

Structure of Surfactant-Polyelectrolyte Complexes

by
K. Rema

**A Thesis submitted to the
Jawaharlal Nehru University
for the Degree of
Doctor of Philosophy**

2003

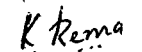
*Raman Research Institute
Bangalore 560 080
India*

Declaration:

I hereby declare that the work reported in this thesis is entirely original. This thesis is composed independently by me at Raman Research Institute under the supervision of Dr. V. A. Raghunathan. I further declare that the subject matter presented in this thesis has not previously formed the basis for the award of any degree, diploma, membership, associateship, fellowship or any other similar title of any university or institution.



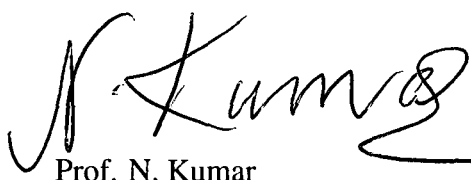
(Dr. V. A. Raghunathan)


(K. Rema)

Liquid Crystal Laboratory
Raman Research Institute
Bangalore 560 080 - INDIA

Certificate:

This is to certify that the thesis entitled **Structure of Surfactant-Polyelectrolyte Complexes** submitted by K. Rema for the award of the degree of Doctor of Philosophy of Jawaharlal Nehru University is her original work. This has not been published or submitted to any other University for any other Degree or Diploma.



Prof. N. Kumar

Director

Raman Research Institute

Bangalore 560 080 INDIA



Dr. V. A. Raghunathan

(Thesis Supervisor)

Acknowledgement:

The work in this thesis has been done under the supervision of Dr. V. A. Raghunathan. I thank him for everything I have learnt from him. Without his patience, support and encouragement, this thesis would not have been possible. I consider myself fortunate to have worked with him.

I thank Dr. Yashodhan Hatwalne and Dr. Madan Rao for their constant interest in this work. I thank Dr. G. V. Shivshankar for several discussions and for all the help received from his group. I thank Dr. J. Samuel and Dr. Bala Iyer for their concern and their encouragement. I thank Dr. Abhishek Dhar, it was a pleasure to discuss my work with him. I also thank Dr. R. Pratibha for all the help received.

I thank Mr. Dhason, Mr. Ram, Mr. Subramanium, Ms. Vasudha, Mr. Ishaq and especially Mr. Mani, for their help in carrying out the experiments. I also thank the Chemistry lab for the help received at various stages of this work. I thank Mr. Raju for his help in developing photographs.

I thank all the library staff for their help, especially Patil, Ratnakar, Girija, Manjunath, Nagaraj, Geetha, Vrinda, Hanumanthappa and Chowdappa.

I thank Mr. Radhakrishna, Ms. Radha, Mr. Manjunath, Ms. Marissa and Ms. Lakshmi for their help in paper work. I also thank the computer department for all the help received.

I thank Sanat for all the discussions and help that I have received from him, he has been an ideal labmate and friend to me. I also thank him for patiently reading through my thesis. I thank Kheya for all the discussions that I have had with her and for her friendship. I thank

Rajkumar for all the help he has given me. I thank Lakshmanan for collaboration. I thank members of the LC group especially Manjula, Surajit, Viswa and Bala. I thank Sajal, Roopa and Dipanjan for discussions.

I thank all the staff and students at RRI, I will always cherish the wonderful atmosphere here.

I thank Mr. Ganguly for giving me the confidence to do research. I thank Sreedhar for the encouragement he gave me just before I joined RRI. I thank Naveen for all the physics that I learnt from him and for all the help he gave me. I thank Madhuri and Abhijit for the good times I had with them. I thank Usha for her help and advice when I needed it the most. I thank Gail and Pati for their wonderful company and help. I thank Niruj and Mamata for their friendship during my years at RRI. I thank Jishnu for constantly pushing me to finish my thesis and for keeping me in good humour. I thank my parents and my sisters, Shobha and Hema, for their support through all these years.

Contents

1	Introduction	1
1.1	Surfactants	1
1.1.1	The Hydrophobic effect	2
1.1.2	Self assembly of amphiphiles	3
1.1.3	Phase behaviour of surfactant solutions	6
1.2	Polymers	10
1.2.1	Polyelectrolytes	11
1.2.2	Counter ion condensation	13
1.3	Formation of surfactant-polyelectrolyte complexes	14
1.4	Theory of x-ray diffraction	15
1.4.1	Polarization and geometric corrections	17
1.4.2	Characterisation of liquid crystalline phases	18
1.5	Experimental Procedure	21
1.5.1	Experimental set up	21
1.5.2	Sample preparation	21
2	Phase behaviour of the CTAB-SHN-water system	26
2.1	Introduction	26
2.2	Earlier studies	27
2.3	Liquid crystalline phases of CTAB-SHN-water system	28
2.4	Curvature defects in lamellar phases	40
2.5	Discussion	41

2.6	Conclusions	46
3	Structures of cationic surfactant-DNA complexes	49
3.1	Introduction	49
3.2	Earlier studies on surfactant-DNA complexes	50
3.3	Structure of CTAB-DNA complex	60
3.4	Modelling the structure of CTAB-DNA complex	61
3.5	Tuning the structure of CTAB-DNA complex with SHN	65
3.6	Discussion	69
3.7	Conclusions	71
4	Influence of hexanol on the structure of CTAB-DNA and CTAB-SHN-DNA complexes	74
4.1	Introduction	74
4.2	Influence of a cosurfactant on the phase behaviour of surfactant-water systems	75
4.3	Theoretical studies on the phase behaviour of cationic lipid-DNA complexes	79
4.4	CTAB-DNA-hexanol Complexes	84
4.5	CTAB-SHN-hexanol-DNA Complexes	88
4.6	Discussion	91
4.7	Conclusion	97
5	Structure of cationic-surfactant – polyelectrolyte complexes	101
5.1	Introduction	101
5.2	Earlier studies	102
5.3	CTAB-polyelectrolyte complexes	107
5.4	CTAB-SHN-polyelectrolyte complexes	110
5.5	DDAB-polyelectrolyte complexes	117
5.5.1	Phase diagram of DDAB-water	117
5.5.2	Earlier studies on DDAB-polyelectrolyte complexes	118

5.5.3	Structure of DDAB-polyelectrolyte complexes	121
5.6	Discussion	125
5.6.1	CTAB-SHN-polyelectrolyte complexes	125
5.6.2	Structures in DDAB-polyelectrolyte complexes	130
5.6.3	Surfactant content of the various polyelectrolyte complexes	132
5.7	Conclusions	134

Preface

This thesis deals with the structure of complexes formed by deoxyribosenucleic acid (DNA) and some other anionic polyelectrolytes with cationic surfactants in dilute aqueous solutions. X-ray diffraction studies on complexes of DNA with cationic double-tailed lipids have established some of the structures exhibited by these systems. The structures of complexes of some synthetic polyelectrolytes with many single-chained cationic surfactants have also been reported. Our objective was to study the structural modifications induced by sodium-3-hydroxy-2-naphthoate (SHN) and hexanol, on complexes of cetyltrimethylammonium bromide (CTAB) with various anionic polyelectrolytes. We also probed the influence of the chemical nature of the polyion on the structure of these complexes. In order to correlate the structure of the complexes, with the phase behaviour of the surfactant system, we have constructed a partial phase diagram of the CTAB-SHN-water system.

The CTAB-SHN-water system is found to exhibit a novel phase behaviour. It shows a lamellar phase with curvature defects at low surfactant concentrations. At high temperatures the defects disappear gradually on decreasing the water content and a lamellar phase without such defects is found at high surfactant concentrations; a similar behaviour has been observed earlier in some surfactant systems. Surprisingly, at lower temperatures, an intermediate ribbon phase appears between the two lamellar phases. Further theoretical work is required to understand this complex phase behaviour.

Cationic lipid-DNA complexes are known to form lamellar and inverted hexagonal structures. We have established a new structure, consisting of DNA strands intercalated into a direct hexagonal phase, in CTAB-DNA complexes.

Structural transitions of these complexes to lamellar and inverted hexagonal phases were observed with the addition of the cosurfactant hexanol. The transition from the lamellar to inverted hexagonal phase in the presence of hexanol has been observed earlier in lipid-DNA

systems. However, a transition from an inverted hexagonal to a lamellar structure driven by DNA concentration was observed for the first time; we propose that this transition is driven by the larger intake of DNA into the lamellar, as compared to the inverted hexagonal structure. We have constructed a partial phase diagram of the system which shows the different structures seen as a function of hexanol and DNA concentrations.

A variety of structures was observed in the complexes of various anionic polyelectrolytes with CTAB-SHN. Some of them have not been reported earlier in polyelectrolyte-surfactant systems. We could also correlate the structures observed in these complexes with those present in the surfactant system at similar surfactant content. Such a correlation has not been suggested in any of the earlier studies. The use of the surfactant system CTAB-SHN which has a rich phase behaviour made this possible in the present case.

In chapter-I, we discuss the phase behaviour of surfactant systems as well as the physical characteristics of polyelectrolytes that are relevant to our study. We also describe here briefly, the theory of x-ray diffraction. Further, we have outlined the experimental techniques employed to study the complexes.

Surfactants are amphiphilic molecules made up of one or more hydrophobic chains attached to a head group which is hydrophilic. In aqueous solutions, they form aggregates above a critical concentration known as the critical micellar concentration. These aggregates known as micelles, may be spherical, rod-like or disk-like in dilute solutions. At high surfactant concentrations, they form liquid crystalline phases with long range orientational order. Polyelectrolytes are polymers which acquire a charge in aqueous solutions by releasing their counter ions. The persistence length of a polymer is a measure of its flexibility, and it is the length below which the polymer chain behaves like a stiff rod. The number of charged groups on the polymer determines its bare charge density. In dilute solutions, the effective charge density of a polyelectrolyte can be much lower than the bare charge density since

some of the counter ions condense back on to the chain. This phenomenon known as the Oosawa-Manning condensation is essentially due to the competition between electrostatics and entropy. Electrostatics requires that the oppositely charged counter ions remain near the polyelectrolyte, whereas the entropy would prefer them to remain dispersed in the solution. Similar behaviour can also occur in the case of aggregates of ionic surfactants. When polyelectrolytes are added to a solution of oppositely charged surfactant, the polyion and the surfactant ion associate to form complexes releasing their respective counter ions into the solution. The resulting increase in the entropy of the counter ions is the main driving mechanism for the complex formation. These complexes form various liquid crystalline phases which may be characterized using x-ray diffraction.

In chapter-II, we describe the characterization of the liquid crystalline phases of CTAB-SHN-water system using polarizing microscopy and x-ray diffraction.

A partial phase diagram of CTAB-SHN-water system at 30 °C constructed from these studies is shown in fig 1. At low SHN concentrations, a direct hexagonal phase (H_1) is observed which consists of long cylindrical micelles arranged on a 2D hexagonal lattice. On increasing the SHN concentration a phase consisting of ribbon-like aggregates arranged on a 2D oblique (O) lattice is obtained. These ribbon phases appear in general in surfactant systems, in between the hexagonal and lamellar phases. At high SHN concentrations, a lamellar phase (L_α^D) is observed over a wide range of surfactant concentration. It contains a large number of pores or slits in the plane of the bilayer. Such lamellar phases with curvature defects have been seen in a few surfactant systems. These defects are found to disappear gradually on increasing the surfactant content. A similar behaviour is observed in the present system at high temperatures (fig. 2). At low temperatures an intermediate centred rectangular phase made of ribbon-like aggregates (fig 3) appears between the two lamellar phases. More theoretical work is required to explain this novel phase behaviour.

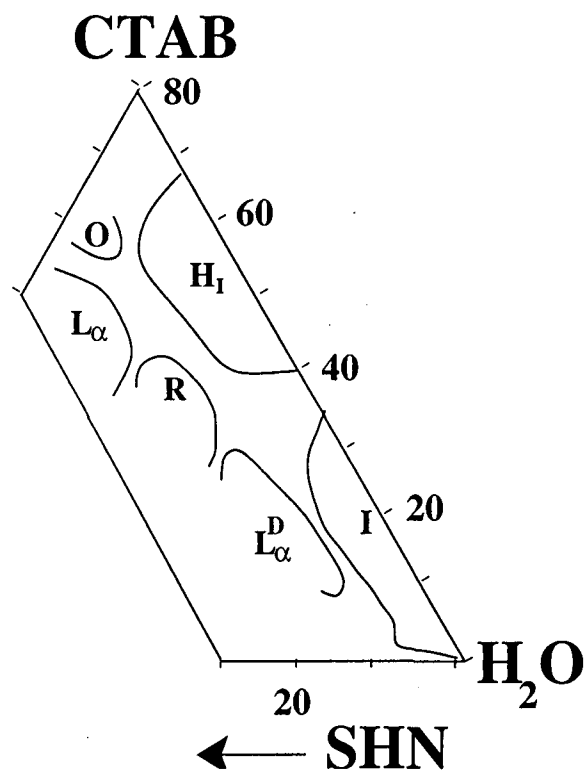


Figure 1: A partial phase diagram indicating the various liquid crystalline phases of CTAB-SHN-water system at 30 °C. L_{α}^D denotes the lamellar phase with defects, O a phase with an oblique lattice, R a ribbon phase with a rectangular lattice, I the isotropic phase, L_{α} the lamellar phase without defects and H the direct hexagonal phase.

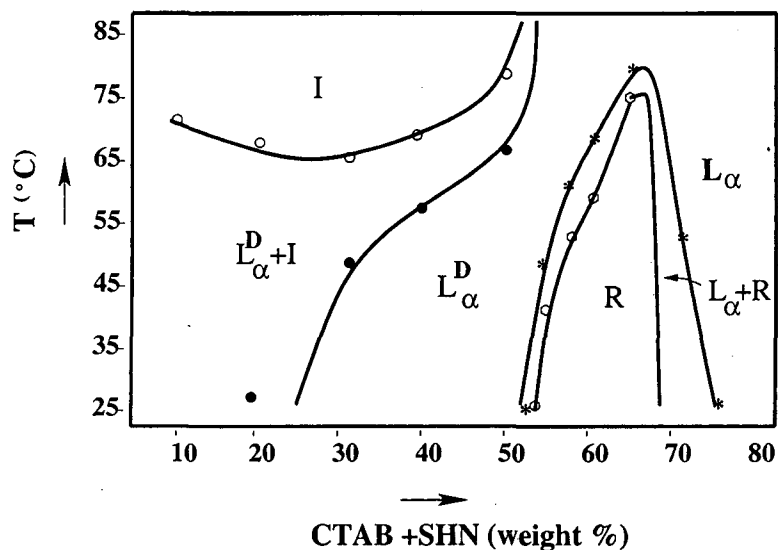


Figure 2: Temperature-composition phase diagram of CTAB-SHN-Water system at equimolar ratios of CTAB and SHN.

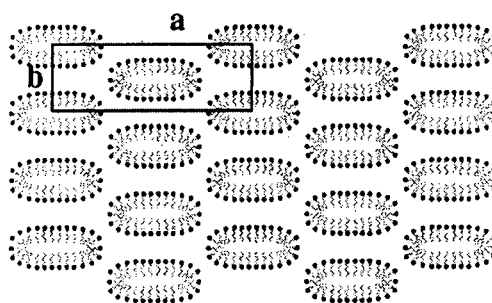


Figure 3: Schematic of the structure of the centred rectangular phase of CTAB-SHN-water system consisting of ribbon-like aggregates arranged on a 2D rectangular lattice. The long axes of the ribbons is normal to the plane shown.

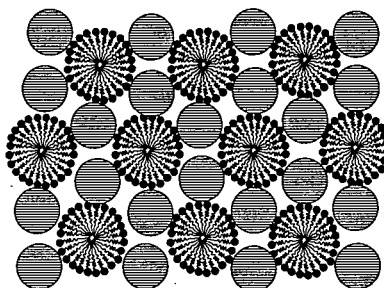


Figure 4: The intercalated hexagonal phase (H_1^C), where each DNA strand (denoted by shaded circles) is surrounded by three cylindrical micelles.

In chapter-III, we discuss our x-ray diffraction studies on complexes of double stranded (ds) and single stranded (ss) DNA with CTAB. Since the addition of SHN decreases the spontaneous curvature of CTAB micelles, we have probed the structural modifications induced by SHN on CTAB-DNA complexes.

The diffraction pattern of CTAB-DNA complexes indicate a 2D hexagonal lattice. However the complex can in principle form either an intercalated hexagonal phase or an inverted hexagonal phase. The intercalated hexagonal phase consists of DNA strands intercalated into the direct hexagonal phase of CTAB (fig 4) where each DNA strand is in contact with three micellar cylinders. Though such a structure was proposed earlier for these complexes, it was not well established. An inverted hexagonal phase consisting of DNA strands covered by a surfactant monolayer and arranged on a 2D hexagonal lattice (fig 5), cannot be ruled

out. Such structures have been seen in cationic lipid-DNA complexes. To establish the structure of these complexes, we have modelled the 2D electron density in the plane normal to the axis of the DNA strands for both the structures. The relative intensities calculated from the models were compared with the experimentally observed values. Only the intercalated structure is consistent with the observed intensities. We conclude from here that CTAB-DNA complexes form an intercalated hexagonal phase.

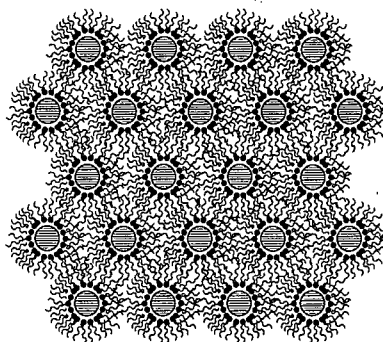


Figure 5: Schematic diagram of the inverted hexagonal phase (H_{II}^C) where the DNA strands are confined to the aqueous cores of the micelles.

CTAB-SHN-DNA complexes also form an intercalated hexagonal phase at low SHN concentrations. At a higher SHN concentration, a lamellar phase is observed in the complex. An intercalated lamellar structure is proposed, consisting of DNA strands sandwiched between the bilayers (fig. 6). Similar structures have been observed in cationic lipid-DNA complexes. The hexagonal to lamellar transition of the CTAB-SHN-DNA complex and the cylinder to bilayer transformation of the aggregates in dilute aqueous solutions of CTAB-SHN, occur at

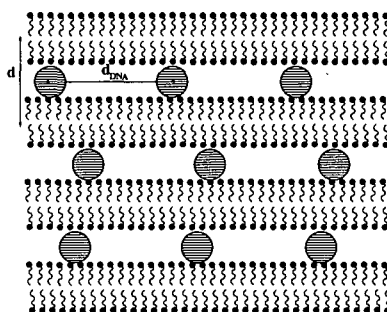


Figure 6: Schematic diagram of lamellar phase (L_{α}^C) of DNA-surfactant complexes, where the DNA strands are sandwiched between surfactant bilayers.

similar SHN concentrations. We conclude from this that the structure of these complexes is determined by the morphology of the aggregates in the surfactant solution. The complexes of ss DNA with CTAB form a hexagonal phase at low SHN concentrations. Since ss DNA strands are highly flexible, the structure consists of cylindrical micelles bridged by the polymer chains. At high SHN concentrations the complex forms a lamellar phase which consists of bilayers bridged by the polymer chains. Thus complexes of ss and ds DNA with CTAB-SHN exhibit similar sequence of phase transitions, though their persistence lengths differ by almost two orders of magnitude.

In chapter-IV, we present our studies on the structural modifications induced by hexanol on CTAB-DNA complexes.

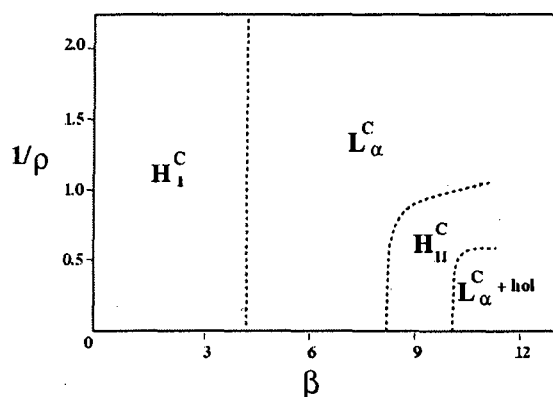


Figure 7: The phase diagram showing the different complexes obtained as a function of hexanol and DNA concentrations. $\beta = [\text{hexanol}]/[\text{CTAB}]$, $\rho = (\text{wt. of CTAB})/(\text{wt. of DNA})$. hol denotes the hexanol rich phase coexisting with the complex. The locations of the different phase boundaries have not been precisely determined.

Three different structures and novel re-entrant phase transitions are found in CTAB-hexanol-DNA complexes as shown in fig 7. At low hexanol concentrations, the complex forms an intercalated hexagonal phase (H_1^C) which transforms to a lamellar phase (L_α^C) on

increasing the hexanol concentration. These transitions are consistent with the cylinder to bilayer transformation of CTAB micelles in the presence of hexanol in aqueous solutions. Hexanol is also known to reduce the bending rigidity of bilayers. This leads to the formation of an inverted hexagonal phase (H_{II}^C), at higher hexanol concentrations. The charges on the DNA are more effectively neutralized due to their greater proximity to the surfactant ions in this structure, as compared to L_{α}^C . Hence the gain in the electrostatic contribution to the free energy is higher in the inverted phase. Further, the energy cost for bending the surfactant monolayer around the DNA is reduced due to their lower bending rigidity in the presence of hexanol thus accounting for the observed behaviour. Further addition of hexanol leads to a phase separation in the surfactant solution to a hexanol rich and surfactant rich phases. The inverted phase reverts back to a lamellar phase possibly due to the decrease in the hexanol content in the surfactant bilayers. At high hexanol content, increasing DNA concentration, leads to a transition from an inverted hexagonal to a lamellar phase. The transition is driven by the lower free energy of the DNA in the complex as compared with that of the uncomplexed DNA in solution. It has been estimated from the geometry of both the structures that nearly twice the amount of DNA can be incorporated into the lamellar phase as compared to the inverted phase at the same surfactant composition. The critical concentration at which the transition occurs can also be estimated. These estimates agree well with the experimentally observed values. Such phase transitions have been predicted earlier, but have not been observed prior to our studies.

In chapter-V, we describe studies on complexes of anionic polyelectrolytes like poly (glutamic acid) (PGA), poly (aspartic acid) (PAA) and poly (vinyl sulfonate) (PVS) with the CTAB-SHN surfactant system.

All complexes form a hexagonal phase at low SHN concentration. Two dimensional rectangular phases consisting of ribbon-like aggregates (fig 8) are formed at high SHN concentrations. The lattice parameters for PGA and PAA complexes are similar, whereas they

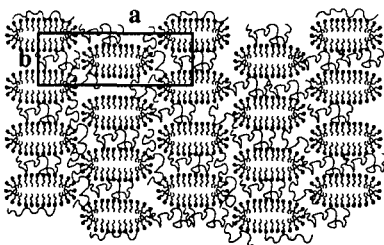


Figure 8: Schematic of the structure of the centred rectangular phase of CTAB-SHN-PAA/PGA/PVS complexes where the ribbon-like surfactant aggregates are bridged by the polyelectrolyte

differ for PVS which has a different charge moiety. The hexagonal phase of the complexes obtained at low SHN concentrations, is consistent with the fact that the surfactant solution consists of cylindrical micelles. The appearance of a rectangular phase in PAA/PGA/PVS complexes and a lamellar phase in DNA complexes, at similar SHN concentrations, is rather surprising. However on estimating the surfactant content in these complexes, we find that the structures seen in these complexes can be correlated with the structures seen in the surfactant system at similar surfactant content.

The dependence of the surfactant content of the complex on the polyelectrolyte used is rather intriguing. The flexibility of the polyelectrolyte cannot be a factor since single as well as double stranded DNA show similar structures at similar SHN concentrations. Since the polyelectrolytes used have comparable bare charge densities, this may also be ruled out as a possible cause. This indicates that the specific interactions between the polyion and the surfactant ion is the most likely cause of the observed behaviour. This conclusion is supported by the results of our studies on the complexes of these polyelectrolytes with the surfactant didodecyldimethylammonium bromide (DDAB).

The following papers contain the work described in this thesis

1. Tuning the structure of surfactant complexes with DNA and other polyelectrolytes,
R. Krishnaswamy, P. Mitra, V. A. Raghunathan, and A. K. Sood,
Europhys. Lett. **62**, 357 (2003).
2. Structures of some surfactant-polyelectrolyte complexes,
R. Krishnaswamy, V. A. Raghunathan, and A. K. Sood,
(to appear in Pramana-J. Phys).
3. Re-entrant phase transitions in DNA-surfactant complexes,
R. Krishnaswamy, V. A. Raghunathan, and A. K. Sood,
(submitted for publication).

Chapter 1

Introduction

This chapter gives a brief introduction to surfactants and polyelectrolytes and x-ray diffraction techniques. The phase behaviour of surfactant systems and the physical characteristics of polyelectrolytes have been discussed in sections 1.1 and 1.2 respectively. The mechanism which drives complex formation between oppositely charged surfactants and polyelectrolytes is described in section 1.3. The theory of x-ray diffraction and the characterization of the different liquid crystalline phases exhibited by surfactant solutions using diffraction methods have been outlined in section 1.4. Finally, the experimental set up, the method of sample preparation, the chemicals used and other experimental details are presented in section 1.5.

1.1 Surfactants

Amphiphilic molecules consist of long hydrocarbon chains covalently attached to molecular groups that tend to associate with water [1, 2]. The hydrocarbon chain is referred to as the tail of the amphiphile and the water-loving molecular group, as the head group. Synthetic amphiphiles are often referred to as surfactants, whereas those of biological origin are usually called lipids. Though this nomenclature is not standard, this is the sense in which these two terms are used here. Depending on the nature of the head group, amphiphiles can be classified as ionic, non-ionic and zwitter-ionic. Ionic amphiphiles dissociate in water and acquire an electric charge. Examples are the single-tailed surfactant cetyltrimethylammo-

onium bromide (CTAB) (fig.1.1A), the double-tailed didodecyldimethylammonium bromide (DDAB) (fig. 1.1B) and the cationic lipid dioleoyltrimethylammonium propane (DOTAP) (fig 1.2). Non-ionic amphiphiles like dodecylhexapolyethyleneoxide ($C_{12}E_6$) have polar head groups which are not charged. In the case of zwitterionic amphiphiles like dioleoylphosphatidyl choline (DOPC) (fig 1.3), the head group acquires a dipole moment in aqueous solutions.

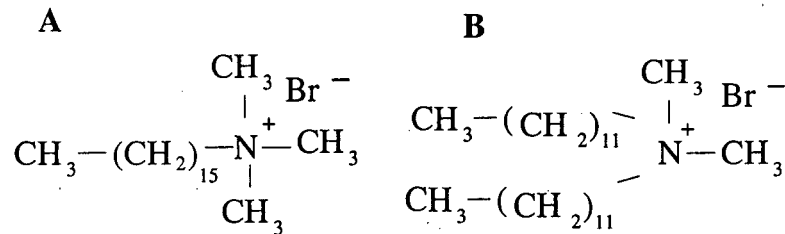


Figure 1.1: Structure of CTAB (A) and DDAB (B).

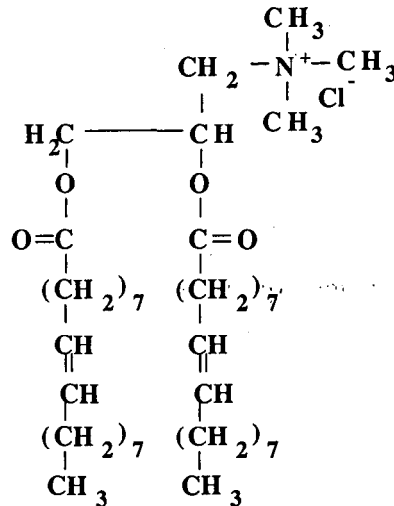


Figure 1.2: Structure of dioleoyltrimethylammonium propane (DOTAP).

1.1.1 The Hydrophobic effect

The interaction between water molecules involve orientation dependent hydrogen bonds with interaction energies in the range $3 - 5 k_B T$, where k_B is the Boltzmann constant and T the temperature. At room temperature, each water molecule is on an average hydrogen bonded

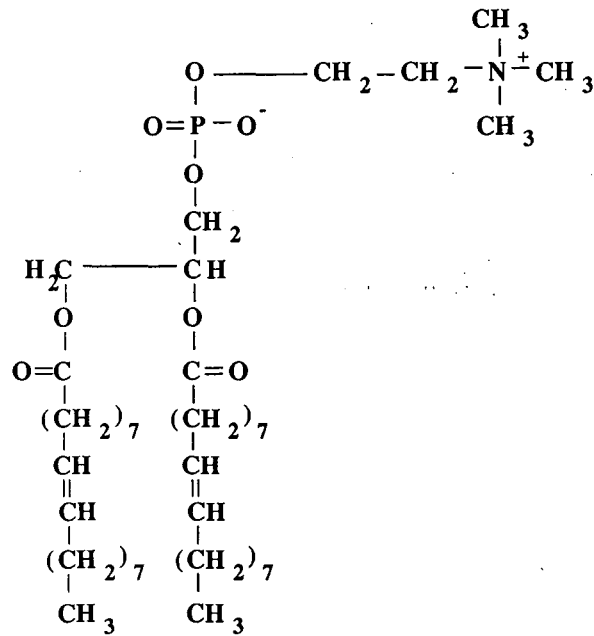


Figure 1.3: Structure of dioleoylphosphatidyl choline (DOPC).

to 3-3.5 molecules. The addition of nonpolar solute molecules like inert atoms, hydrocarbons and fluorocarbons in aqueous solutions disrupts the hydrogen bonds between the water molecules. The water molecules can however form a tetrahedral structure with each other and reorient themselves around these molecules to form 'cage-like' structures. Depending on the size of the solute molecules, they become more ordered than the molecules in the bulk liquid, resulting in a decrease in the entropy of the system. Hence it becomes thermodynamically unfavourable for nonpolar molecules like hydrocarbons to dissolve in water. This immiscibility of inert substances in water which is of entropic origin is known as the hydrophobic effect [2, 3].

1.1.2 Self assembly of amphiphiles

Amphiphilic molecules have low solubilities in water as a result of the hydrophobic effect. They form monolayers at air-water interface in order to minimize contact between their tails and water. Some amphiphiles can form aggregates called micelles in water, where the head groups shield the chains from coming in contact with water. This process is called self

assembly [1, 2].

From a thermodynamic point of view, an aqueous solution of an amphiphile can be considered as a multicomponent system with several phases in equilibrium. Each phase is taken to consist of aggregates of a given aggregation number, which is the number of molecules in an aggregate. For a very dilute solution, the interaction between the aggregates may be neglected and one can apply the theory of dilute solutions to this system.

The chemical potential of an amphiphile in an s -aggregate is given by

$$\tilde{\mu}_s = \tilde{\mu}_s^o + (k_B T/s) \ln(X_s/s)$$

$\tilde{\mu}_s^o$ is the standard part of the chemical potential containing contributions from the interactions of the amphiphiles within the s -aggregate. The second term comes from the entropy of mixing. X_s is the mole fraction of amphiphiles that form s -aggregates. The total mole fraction of the amphiphiles $X = \sum_{s=1}^{\infty} X_s \ll 1$. In chemical equilibrium, the chemical potential of the amphiphile $\tilde{\mu}_s$ remains the same for all s . Thus

$$\begin{aligned} \tilde{\mu}_1^o + k_B T \ln(X_1) &= \tilde{\mu}_2^o + (k_B T/2) \ln(X_2/2) = \dots \\ &= \tilde{\mu}_n^o + (k_B T/n) \ln(X_n/n) \end{aligned}$$

This gives the equilibrium distribution of the s -aggregates as

$$X_s/s = X_1^s e^{s(\tilde{\mu}_1^o - \tilde{\mu}_s^o)/k_B T}$$

If we define $\alpha = (\tilde{\mu}_1^o - \tilde{\mu}_s^o)/k_B T$, then $X_s = s(X_1 e^\alpha)^s$.

Therefore, aggregation can take place only if $\alpha > 0$. Hence the energy per molecule must be lower in aggregates of size M , for some $M > 1$. In practice, $M \sim 50$, and is determined by the optimal packing of the hydrocarbon chains within the micelles.

Since X_s cannot exceed unity, the limiting value of monomer concentration, $X_1 \sim e^{-\alpha}$. The critical micellar concentration (CMC), is the amphiphile concentration at which X_1 saturates and further addition of amphiphiles leads to the formation of micelles (fig 1.4). It is given by, $\text{CMC} \approx e^{-\alpha}$

Hence larger the enthalpy gain in forming an aggregate, the lower the CMC. At CMC, many physical properties of the amphiphile solution exhibit an anomalous behaviour (fig

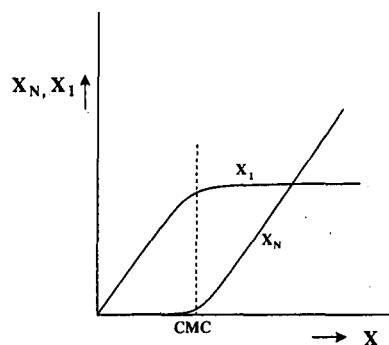


Figure 1.4: Variation of X_1 and X_N as a function of the amphiphile concentration X .

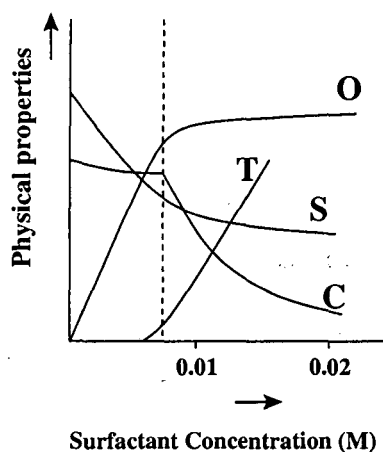


Figure 1.5: Effect of micellization on the bulk properties of surfactant solutions. O, T, S and C denotes the osmotic pressure, turbidity, surface tension and equivalent conductivity of the surfactant solution respectively. The dashed line indicates the critical micellar concentration (CMC). The CMC value and concentration scale corresponds to an aqueous solution of sodium dodecylsulphate. [4]

1.5). These trends can be used to estimate the CMC of an amphiphile in aqueous solution. For CTAB, CMC \sim 1 mM.

Just above CMC, the amphiphiles generally form spherical micelles (fig 1.6). At higher concentrations, they usually form disk-like or rod-like micelles. The size distribution of micelles depends on the aggregate geometry. Spherical micelles (fig 1.6), whose radius is determined by the alkyl chain length of the amphiphile, remain fairly monodisperse. Disk-like micelles whose thickness $h \approx 2l$ where l is the length of the hydrocarbon chain, form infinite bilayers, even at low surfactant concentration. Rod-like micelles whose radius $r \approx l$ are however found to be highly polydisperse. In order to prevent the hydrocarbon chains from

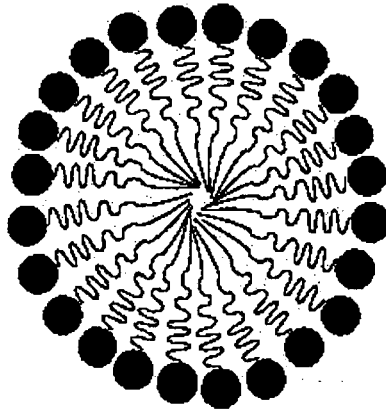


Figure 1.6: Schematic diagram of the crosssection of a spherical micelle, formed in dilute surfactant solutions above CMC.

being in contact with water, the disks have semitoroidal rims and the rods have hemispherical end caps. The formation of these curved edges, however cost energy. The difference in the behaviour of disc-like and rod-like micelles arises from the fact that the perimeter of the rim of a disk increases with the disk radius, whereas the size of the end cap on a cylinder is independent of the length of the cylinder.

If we neglect the inter-aggregate interactions, the average size of a rod-like micelle is given by

$$\langle s \rangle = 2(Xe^\delta)^{1/2}$$

X is the concentration of the amphiphile and δ the energy cost for creating an end cap. δ can be made very large by adding certain salts and alcohols to the amphiphile solution. This results in the formation of very long, flexible micelles that become entangled to form a viscoelastic gel. These are known as ‘worm-like’ micelles and behave in many ways similar to polymers [5].

1.1.3 Phase behaviour of surfactant solutions

Surfactant solutions exhibit many liquid crystalline phases at high surfactant concentrations. All these phases are characterized by long range orientational order of the aggregates.

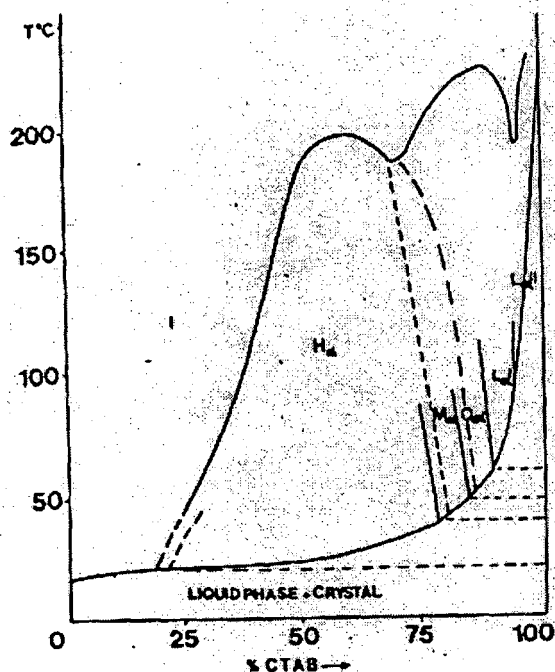


Figure 1.7: Partial temperature-composition phase diagram of CTAB-water system. I, H_{α} , M_{α} and Q_{α} denote the isotropic, 2D hexagonal, monoclinic and cubic phases. L_{α}^I denotes the lamellar phase obtained at lower temperatures where the bilayers are separated by water and L_{α}^{II} is the lamellar phase at high temperatures where the bilayers are collapsed with very little water between them [6].

Here we shall discuss the phase behaviour of two surfactant systems, one of which forms rod-like and the other disc-like aggregates in dilute solutions.

The phase diagram of CTAB-water system is given in figure 1.7 [6]. Just above CMC, the solution consists of spherical micelles. However they transform to rod-like micelles at a higher surfactant concentration (ϕ_s). The rods are randomly oriented and have no positional correlations. Hence the solution is isotropic.

On increasing ϕ_s , the length of the rods increases and long range positional and orientational order develop in the system, with cylindrical micelles arranging themselves on a 2D hexagonal lattice (fig 1.8). At 30°C, hexagonal phase appears over a wide range of surfactant concentration in the CTAB-water system. When the surfactant content is higher than 75 %, a monoclinic phase (M_{α}) appears above 50°C. This phase consists of long aggregates with an almost elliptical cross section, termed as 'ribbon-like', arranged on a 2D oblique lattice.

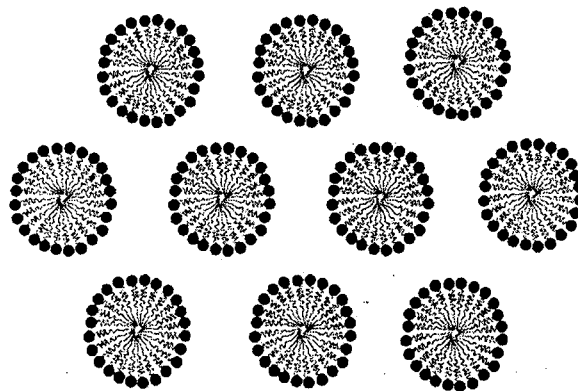


Figure 1.8: Schematic diagram of the hexagonal phase which consists of cylindrical micelles arranged on a 2D hexagonal lattice. The cylinders are oriented normal to the plane shown.



Figure 1.9: Schematic diagram of the lamellar phase which consists of bilayers stacked one above the other. d is the lamellar periodicity.

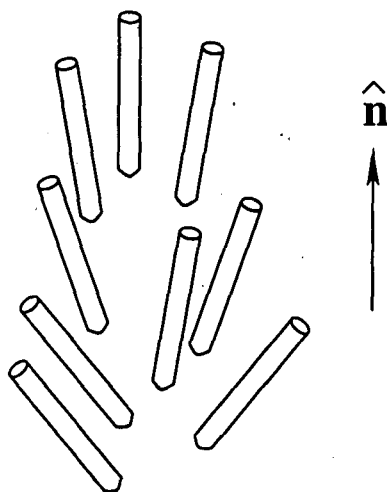


Figure 1.10: Schematic diagram of nematic phase formed by rod-like micelles. $\hat{\mathbf{n}}$ is the apolar director.

Beyond the monoclinic phase, a cubic phase (Q_α) appears. At very high ϕ_s , a lamellar phase is observed in the system which consists of bilayers separated by water (L'_α) (fig 1.9). At high temperatures, above 80 °C another lamellar phase (L''_α) is observed in which the bilayers are collapsed, with very little water between them. The reason for the formation of L''_α is not known at present.

In some systems, in between the isotropic and hexagonal phases, the rod-like micelles acquire long range orientational order to form a nematic phase. This phase is also exhibited occasionally by disk-like micelles in between the isotropic and lamellar phases. Here the symmetry axis of the rod-like (disk-like) micelle has a preferred direction of orientation which is referred to as the nematic director $\hat{\mathbf{n}}$ (fig 1.10).

In the cesium pentadecafluorooctanoate (CsPFO)-water system (fig 1.11), the dilute solution consists of disk-like micelles [7]. At a higher surfactant concentration a nematic phase formed by disk-like micelles is obtained (N_D^+). Further increase in the concentration leads to the appearance of a lamellar phase (L_D). Transitions between these three phases can also be driven by changing the temperature at intermediate values of ϕ_s .

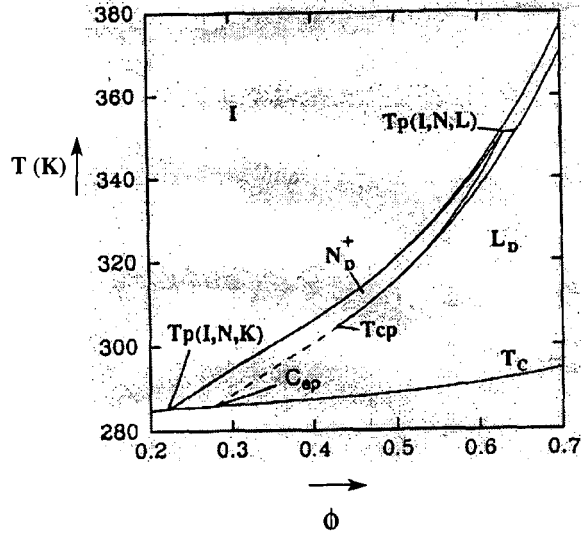


Figure 1.11: Partial temperature-composition phase diagram of CsPFO-water system. I, N_D^+ , L_D denotes the isotropic, nematic and lamellar phases formed by disc-like micelles [7]. T_p denotes the triple points where three phases meet. T_{cp} is a tricritical point across which the nematic to lamellar transition goes from being first order to continuous.

1.2 Polymers

Polymers are obtained by the covalent bonding of a large number of repeat units called monomers [8, 9]. A simple example is polyethylene, whose structure can be represented as $(-CH_2 - CH_2-)_N$. The number of repeat units N is called the degree of polymerization. In a homopolymer, like polyethylene, the repeat units are identical. Polymers in which the repeat units vary are known as copolymers or heteropolymers. For example, single stranded DNA is a heteropolymer with 4 different types of repeat units.

The persistence length l_p , of a polymer is a measure of its flexibility. It can be defined in terms of the orientational correlation length of the tangent vector $\hat{t}(s)$ of the polymer backbone; $\langle \hat{t}(s) \cdot \hat{t}(s+r) \rangle \sim e^{-r/l_p}$. Here $\langle \dots \rangle$ denotes the thermal average, and r is the contour length between the two points. A section of chain shorter than the persistence length behaves like a stiff rod and sections of the chain separated by a distance much larger than the persistence length l_p bend independently of each other. The persistence length of polyethylene is about 1.5 nm and consists of 4 to 5 C-C bonds whereas the persistence length of double

stranded DNA is about 50 nm and consists of roughly 150 bp.

Due to the flexibility of the polymer, any polymer chain which is sufficiently long, forms a random coil in a good solvent. To estimate the size of an ideal polymer chain, it can be treated as a random walk where each step is independent of the previous one. If b is the step size, then the k th step is given by $\mathbf{a}_k = b\hat{a}_k$. As $\mathbf{R} = \sum_{k=1}^N \mathbf{a}_k$, the mean square end to end distance is given by, $\langle R^2 \rangle = \sum_{k=1}^N \sum_{l=1}^N \langle \mathbf{a}_k \cdot \mathbf{a}_l \rangle$. Since each step is independent and can be oriented in any direction, $\langle \mathbf{a}_k \cdot \mathbf{a}_l \rangle = 0$, for $k \neq l$. Hence

$$\langle R^2 \rangle = N \cdot b^2$$

Thus the root mean square end to end distance of a long ideal chain, is proportional to $N^{1/2}$. However in the above estimation, we have not taken into account the fact that different segments of the chain cannot intersect each other. Thus effectively there is a short range repulsive interaction between the chain segments. By taking into account these excluded volume effects, it has been shown that $R \sim N^{3/5}$.

1.2.1 Polyelectrolytes

Polymers in which, the monomers dissociate in aqueous solutions to become charged by releasing their counter ions are known as polyelectrolytes [9]. Examples of polyelectrolytes are DNA and poly (acrylic acid) (PAA). Since the number of charged monomers is equal to the number of counter ions, the polymer solution as a whole is electrically neutral. If e is the charge of a monomer and ϵ , the dielectric constant of the solution, then the Coulomb interaction between two charged monomers separated by a distance r , is given by $V(r) = (e^2 / \epsilon r) e^{(-r/\lambda_D)}$, where λ_D is the Debye screening length. $\lambda_D = \left[\frac{\epsilon k_B T}{4\pi n e^2} \right]^{1/2}$ where e is the elementary charge and n is the concentration of counter ions or the ionic strength of the solution. In a dilute polyelectrolyte solution, the concentration of counter ions is very low and λ_D is very large. Hence due to the long range Coulomb repulsion between the monomers, the chain remains fully extended and the end to end distance $R \sim N$.

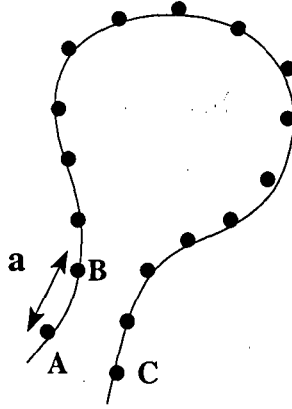


Figure 1.12: A polyelectrolyte chain which bends at length scales much larger than r_D .

In a polyelectrolyte solution of finite concentration, the presence of counter ions in the solution can screen the Coulomb interactions. Hence the polyelectrolyte no longer remains extended, but takes a coil-like configuration. However at shorter length scales, the polyelectrolyte remains stiff due to the electrostatic interactions. The persistence length of a polyelectrolyte (l_p) has contributions from the rigidity of the polymer backbone, known as the intrinsic persistence length (l_o), as well as from electrostatic interactions between the monomers (l_e). Electrostatic contributions can arise in two ways; At short length scales comparable to the separation between the charged monomers on the backbone $a \ll \lambda_D$, the Coulomb repulsion between the charges on the polymer backbone (A and B in fig 1.12), leads to the stiffening of the chain. At large length scales, when the chain bends, a Coulomb repulsion arises when the charges come closer (A and C in fig 1.12) than λ_D , which may also be classified under excluded volume interactions. Taking into account these interactions, the electrostatic contribution to the persistence length l_e is given by, $l_e = u \lambda_D^2 / 4a$, where $u = l_B/a$. $l_B = e^2 / \epsilon k_B T$ is the Bjerrum length, k_B the Boltzmann constant and T the temperature. The Bjerrum length is the separation between two elementary charges at which the Coulomb interaction energy is $k_B T$. Typically, $u \sim 1$, $\lambda_D \gg a$, when the salt concentration is not high. Therefore $l_e \gg \lambda_D$. Hence the stiffening of the polymer chain due to electrostatic interaction occurs on length scales much larger than the Debye length.

1.2.2 Counter ion condensation

Besides screening the Coulomb interactions in the solution, the counter ions can also condense near the polymer chain in the case of highly charged polyelectrolytes, reducing the effective charge density. This is known as the Oosawa-Manning condensation [10]. The linear charge density $\rho_o = e/a$, where a is the separation between the charged units. In a salt free solution, some of the counter ions stay near the polymer and hence remain 'bound', whereas the remaining can be anywhere in the solution and are 'free'. In a simple treatment of the problem, these two regions may be considered as two phases coexisting in equilibrium and the condition under which the counter ions remain bound or condensed can be determined.

If c_1 and c_2 are the concentrations of bound and free counter ions in regions 1 and 2 respectively, and ψ_1 and ψ_2 the electrostatic potentials in these regions, $c_1 = c_2 e^{-e\delta\psi/k_B T}$, $\delta\psi = \psi_1 - \psi_2$. If β is the volume fraction of counter ions in region 2, and ϕ , the volume fraction of region 1 in the solution, then c_1 and c_2 can be expressed in terms of β and ϕ . Then the above relation becomes,

$$\ln [(1-\beta)/\beta] - \ln [\phi/(1-\phi)] = -e\delta\psi/k_B T$$

The polyelectrolyte can be represented as a cylinder at length scales $\sim \lambda_D$. Then the potential difference between regions 1 and 2 can be written as $\delta\psi = (-\rho/\epsilon)\ln(1/\phi)$. Since $(1-\beta)$ is the fraction of counter ions condensed, the effective charge density $\rho = e\beta/a$. In a dilute solution, $\phi \ll 1$. Hence

$$\ln[(1-\beta)/\beta] - \ln[\phi] = (-e^2\beta/\epsilon a k_B T)\ln[\phi], \text{ or}$$

$$\ln[(1-\beta)/\beta] = (1-u\beta) \ln[\phi], \text{ where } u = (e^2/\epsilon a k_B T)$$

Depending on the value of u , two different regimes of behaviour are found. If $u < 1$, then as $\phi \rightarrow 0$, $\beta \rightarrow 1$, hence most of the counter ions remain in the solution. If $u > 1$, then as $\phi \rightarrow 0$, $\beta \rightarrow 1/u$, and the fraction $(1-\beta)$ of the counter ions remain near the polyelectrolyte. This corresponds to counter ion condensation. For $u < 1$, the effective charge density remains the same as the bare charge density. For $u > 1$, the effective charge density is always less than

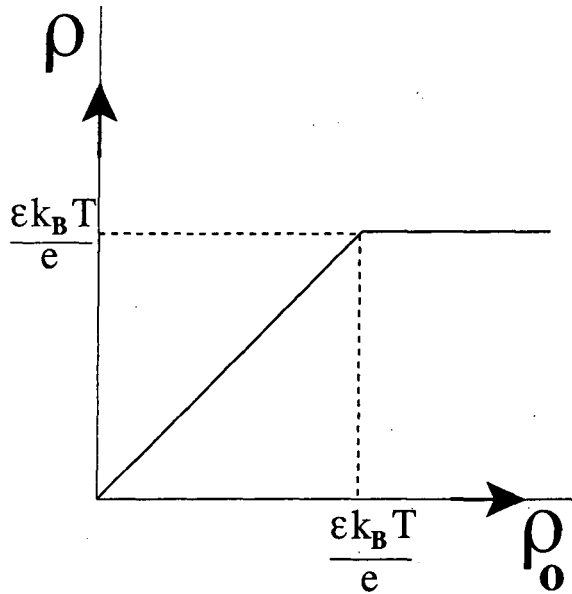


Figure 1.13: Dependence of the effective charge density (ρ) of the polyelectrolyte on the bare charge density (ρ_0). Counter ion condensation occurs for $\rho_0 > \epsilon k_B T / e$, denoted by dashed line.

the bare charge density (fig 1.13). Since $u = l_B/a$, this means that the effective separation between the charges on the polyelectrolyte cannot be less than the Bjerrum length l_B .

Thus the phenomenon of counter ion condensation may be understood as follows: The electrostatic interaction of the counter ions with the polyelectrolyte $\sim 2\rho_0 e \ln r / \epsilon$, would restrict the counter ions to the vicinity of the polyelectrolyte segments. However this involves a loss in entropy of the counter ions $\sim k_B T \ln r^2$. Since both the contributions are proportional to $\ln r$, depending on the coefficient of $\ln r$, the electrostatics or the entropy determines the counter ion distribution in the solution.

1.3 Formation of surfactant-polyelectrolyte complexes

Similar to the polyelectrolytes, the micelles of ionic surfactants also acquire a charge in aqueous solutions. Therefore, the counter ion condensation phenomenon discussed in the case of polyelectrolytes is also applicable here. However the extent of this condensation depends on the geometry of the aggregates. Poisson-Boltzmann theory shows that in pla-

nar bilayers, the counter ions remain always condensed independent of the surface charge density [11]. For a spherical micelle, however, the counter ions remain in solution. The behaviour in the case of long rod-like micelles is similar to that in polyelectrolytes.

In a dilute solution containing oppositely charged surfactants and polyions, the surfactant ion can associate with the polyion to release their corresponding condensed counter ions into the solution. The resultant increase in the entropy of the counter ions is the driving mechanism for complex formation between surfactants and polyelectrolytes. The complex phase separates out of the aqueous solution as a precipitate. Most of the counter ions remain in the aqueous solution which is known as the supernatant. This complex is birefringent and forms various liquid crystalline phases which are described in the subsequent chapters of this thesis.

Counter ion release has been experimentally verified in complexes of the cationic lipid dioleoyltrimethylammonium propane (DOTAP) with ds DNA [12]. The increase in electrical conductivity of the solution due to the counter ion release has been determined from conductivity measurements. It is found that the increase is maximum at the DNA concentration corresponding to the isoelectric point, where all the charges on the DNA can be neutralized by the cationic lipid.

1.4 Theory of x-ray diffraction

X-rays are transverse electromagnetic radiations of short wavelength. The diffraction of x-rays occur due to the scattering by the electrons in the material. The interference of these scattered waves gives rise to the observed diffraction pattern [13, 14]. Hence we consider only coherent, elastic scattering events.

Consider a plane wave of amplitude ϕ_0 and wave vector \mathbf{k}_0 , incident on two electrons,

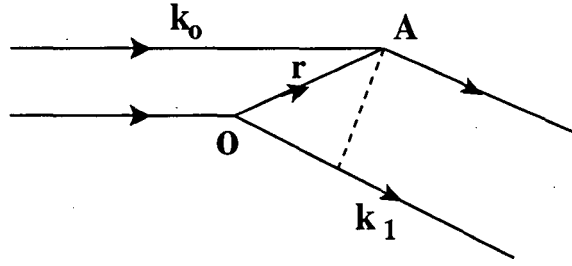


Figure 1.14: Scattering from discrete points; \mathbf{k}_0 and \mathbf{k}_1 denotes the incident and scattered wave vectors. O is the origin. A is a point at a distance r from the origin.

one of which is at the origin and the other at \mathbf{r}

$$\phi_{inc} = \phi_o e^{i\mathbf{k}_0 \cdot \mathbf{r}}$$

The amplitude of the spherical wave scattered by the two electrons at a distance \mathbf{R} ($|\mathbf{R}| \gg |\mathbf{r}|$) is given by

$$\phi_{sc} = (\phi_o a/R) e^{(ikR)} (1 + e^{i\mathbf{q} \cdot \mathbf{r}})$$

where a is the scattering length that determines the strength of scattering and $\mathbf{q} = \mathbf{k}_1 - \mathbf{k}_0$ is called the scattering vector. $q = |\mathbf{q}| = 4\pi \sin\theta/\lambda$ is the scattering wave vector where λ is the wavelength of the incident wave and 2θ the scattering angle. \mathbf{k}_1 is the wave vector in the direction of \mathbf{R} . Since we consider only elastic scattering, $|\mathbf{k}_0| = |\mathbf{k}_1| = k$. If we have an assembly of N electrons at positions \mathbf{r}_i , $i = 1, 2, 3 \dots$, then

$$\phi_{sc} = (\phi_o a/R) \sum_{i=1}^N e^{i(kR - \mathbf{q} \cdot \mathbf{r}_i)},$$

For a continuum distribution of electrons given by density $\rho(\mathbf{r}) = \sum_{i=1}^N \delta(\mathbf{r} - \mathbf{r}_i)$,

$$\phi_{sc} = (\phi_o a/R) e^{(ikR)} \int \rho(\mathbf{r}) e^{-i\mathbf{q} \cdot \mathbf{r}} d\mathbf{r}$$

Thus the scattered amplitude is proportional to the Fourier transform of the electron density of the scattering medium. Here we assume that the scattering is sufficiently weak so that there is no reduction in the intensity as the incident wave propagates through the medium. Hence multiple scattering events are not considered.

The intensity of the scattered radiation $I(\mathbf{q}) = |\phi_{sc}|^2 R^2 / |\phi_{inc}|^2 = A|F(\mathbf{q})|^2$, where

$$F(\mathbf{q}) = \int \rho(\mathbf{r}) e^{-i\mathbf{q}\cdot\mathbf{r}} d\mathbf{r}$$

A is a constant independent of \mathbf{q} .

A periodic structure like a crystal consists of an arrangement of a repetitive unit called the basis on a lattice. Hence $\rho(\mathbf{r})$ of such a system can be described as the convolution of a function representing the lattice $\rho_L(\mathbf{r})$ with another function representing the basis $\rho_b(\mathbf{r})$ [14].
 $\rho(\mathbf{r}) = \rho_L(\mathbf{r}) \otimes \rho_b(\mathbf{r})$.

The structure of the lattice may be described in terms of a set of delta functions, given by

$$\rho_L(\mathbf{r}) = \sum_m \sum_n \sum_p \delta(\mathbf{r} - m\mathbf{a} - n\mathbf{b} - p\mathbf{c})$$

where \mathbf{a} , \mathbf{b} , \mathbf{c} are the basis vectors of the lattice. m , n , p are integers.

Taking the Fourier transform, we get

$$F(\mathbf{q}) = F_L(\mathbf{q}) \cdot F_b(\mathbf{q}) \text{ and hence } I(\mathbf{q}) = |F_L(\mathbf{q})|^2 \cdot |F_b(\mathbf{q})|^2.$$

$F_L(\mathbf{q}) = \sum_h \sum_k \sum_l \delta(\mathbf{q} - h\mathbf{a}^* - k\mathbf{b}^* - l\mathbf{c}^*)$ where \mathbf{a}^* , \mathbf{b}^* , \mathbf{c}^* are the basis vectors of the reciprocal lattice. h , k , l are integers.

$F(\mathbf{q})$ is often called the form factor of the basis and defined by

$$F_b(\mathbf{q}) = \int e^{-i\mathbf{q}\cdot\mathbf{r}} \rho_b(\mathbf{r}) d\mathbf{r}$$

$F_b(\mathbf{q})$ gives the amplitude of the diffraction pattern sampled at the reciprocal lattice points determined by $F_L(\mathbf{q})$.

1.4.1 Polarization and geometric corrections

The scattered intensity from a sample is affected by certain factors that depend on the scattering angle. Therefore, the observed intensities have to be corrected for these effects be-

fore they can be put on a relative scale. The corrected scattered intensity is given by, $I(\mathbf{q}) = A p g I_o(\mathbf{q})$, where $I_o(\mathbf{q})$ is the observed intensity and A, a constant independent of q . p and g depend on q and are called the polarization and geometric factors respectively.

The polarization factor, $p = (1 + \cos^2 2\theta)^{-1}$, and arises from the fact that the incident x-ray beam is unpolarized. In the case of small angle diffraction, $\cos(\theta) \sim 1$ and hence this correction can be ignored.

The geometric correction, g , depends both on the type of sample and detector used in the experiment. In the case of unaligned samples, each diffraction peak is spread over a spherical shell of radius q . If a one dimensional detector is used to collect the data, then the observed intensity has to be multiplied by the area of this shell to get the total intensity of the peak; in this case $g = q^2$. On the other hand, if a two-dimensional detector like an image plate is used, rings obtained correspond to the intersection of these shells by a plane. If the observed intensities are integrated over these rings, then they have to be further multiplied by q to get the true intensities; in this case $g = q$.

1.4.2 Characterisation of liquid crystalline phases

The liquid crystalline phases are birefringent and exhibit characteristic textures when observed under a polarizing microscope. The typical textures of hexagonal and lamellar phases are shown in fig. 1.15 and fig 1.16 respectively. Since these mesophases have either long range or quasi long range positional order, x-ray diffraction gives sharp peaks in the small angle region.

The diffraction pattern of the lamellar phase is the easiest to identify. It consists of a set of peaks in the small angle region, the magnitude of their scattering vectors, q , being in the ratio 1:2:3 etc. These correspond to different orders of reflection from a lamellar periodicity d .

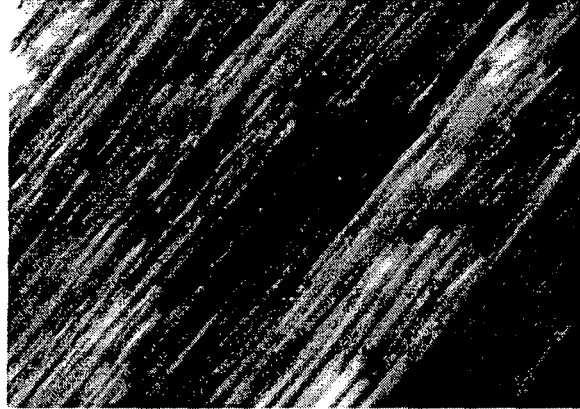


Figure 1.15: Typical texture of the hexagonal phase when observed between crossed polarizers.

The hexagonal phase gives rise to a set of peaks, whose q are in the ratio $1: \sqrt{3}: 2: \sqrt{7}: 3$ etc. These correspond to the $(1\ 0)$, $(1\ 1)$, $(2\ 0)$, $(2\ 1)$ and $(3\ 0)$ planes of a two dimensional hexagonal lattice. The lattice parameter is given by $a = 2\ d_{10}/\sqrt{3}$.

The lamellar and hexagonal phases can in general be identified unambiguously on the basis of their textures and diffraction patterns. However, this is not the case with the ribbon-phases. The textures exhibited by them are very similar to that of the hexagonal phase, as they are all characterized by a two-dimensional lattice. The diffraction patterns of these phases consist of a few peaks in the small angle region, with no specific relation between the corresponding values of q . In most of the cases these can be indexed on a centred rectangular lattice, such that reflections with $h + k = \text{odd integer}$, are absent. From the symmetry of the ribbons, these structures can be assigned to the plane group $cm\bar{m}$ (fig 1.17). Less frequently, the reflections can only be indexed on a rectangular pgg lattice, where $(h\ 0)$ and $(0\ k)$ reflections with h and k odd are absent. In some rare cases the reflections cannot be indexed on a rectangular lattice, and an oblique lattice has to be invoked. Since the latter is the least symmetric one in two dimensions, all systems characterized by positional order in two dimensions can be indexed on such a lattice. In practice, we first try to fit a centred rectangular lattice, then rectangular, and finally an oblique lattice.



Figure 1.16: Typical texture of the lamellar phase when observed between crossed polarizers.

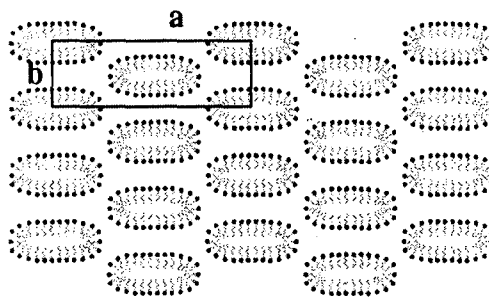


Figure 1.17: Schematic diagram of ribbon phase which consists of ribbon-like aggregates arranged on a 2D centred rectangular lattice. The long axis of the ribbons are normal to the plane shown.

1.5 Experimental Procedure

1.5.1 Experimental set up

X-rays were produced from a rotating anode x-ray generator (*Rigaku, UltraX 18*) operating at 50 kV and 80 mA. Cu K_{α} radiation of wavelength 0.154 nm was selected using a flat graphite monochromator (*Huber*). The sample taken in a glass capillary (*Hampton Research*, outer diameter - 0.5 to 1 mm, wall thickness - 0.01 mm) was placed in a locally built temperature controlled heater with a stability of ± 0.1 K. Most of the experiments were carried out at room temperature (30°C). In a few cases, we have also carried out measurements at higher temperatures (up to 90 °C). The data were collected using an image plate (*Marresearch*, diameter 80 mm). The sample to film distance varied from 200 mm to 300 mm. Typical exposure times were one to 2 hours. The experimental set up is shown schematically in fig (1.18).

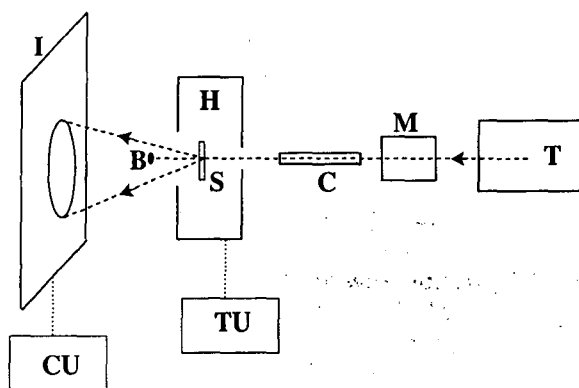


Figure 1.18: Schematic of the experimental set up. T, M, C, H, B, TU, I, CU, denotes the x-ray generator, monochromator, collimator, the heater, beamstop, temperature control unit, image plate and the scanning unit respectively. The dashed line represents the incident and scattered rays.

1.5.2 Sample preparation

Cetyltrimethylammonium bromide (CTAB)(fig 1 A), 3-hydroxy-2-naphthoic acid (HNA), didodecyldimethylammonium bromide (DDAB) (fig 1 B) and hexanol, were obtained from *Aldrich*. Sodium salts of calf thymus ds DNA (30 to 50 kbp) and poly (glutamic acid) (PGA) (fig 1.20) (MW=13650) were purchased from *Sigma*. M13 mp18 ss DNA (7250 bp) was ob-

tained from *Bangalore Genei*.

Poly (acrylic acid) (PAA) (fig 1.20) (MW=2000) and sodium salts of poly (vinyl sulfonate) (PVS) (fig 1.20) and poly (styrene sulfonate) (PSS) (MW=70000) (fig 1.20) were obtained from Aldrich. Sodium salt of PAA was prepared by adding equivalent amount of NaOH to water. 3-sodium-2-hydroxy naphthoate (SHN) (fig 1.19), was prepared by adding equivalent amounts of sodium hydroxide (NaOH) to the HNA solution. The bare charge densities and persistence lengths of the polyelectrolytes used are given in table 1.1.

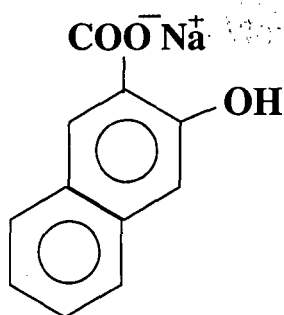


Figure 1.19: Structure of 3-sodium-2-hydroxy naphthoate (SHN).

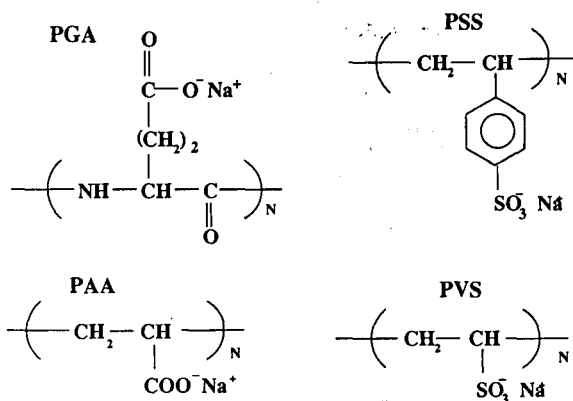


Figure 1.20: The structures of the polyelectrolytes used, namely, poly (glutamic acid) (PGA), poly (acrylic acid) (PAA), poly (vinyl sulfonate) (PVS), poly (styrene sulfonate) (PSS).

To prepare the complexes, surfactant solutions of appropriate concentrations were prepared using de-ionized water (Millipore). The polyelectrolytes were added to the solution. The complex which phase separates out was left in the solution for 3 or 4 days. It was then

Table 1.1: The bare charge densities and persistence lengths of the polyelectrolytes used namely double stranded (ds) DNA, single stranded (ss) DNA, poly (glutamic acid) (PGA), poly (acrylic acid) (PAA), poly (vinyl sulfonate) (PVS), poly (styrene sulfonate) (PSS).

Polyelectrolyte	bare charge density	l_p (nm)
ds DNA	$1 \bar{e}/0.17 \text{ nm}$	50
ss DNA	$1 \bar{e}/0.59 \text{ nm}$	1.5
PGA	$1 \bar{e}/0.154 \text{ nm}$	2
PAA	$1 \bar{e}/0.32 \text{ nm}$	1
PVS	$1 \bar{e}/0.32 \text{ nm}$	1
PSS	$1 \bar{e}/0.25 \text{ nm}$	10

transferred to a capillary along with some supernatant. The capillary was sealed using candle flame.

To prepare CTAB-SHN-water mixtures, appropriate amounts of CTAB and SHN were weighed out. The required concentration was obtained by adding the appropriate amount of water. The tubes containing the mixture were sealed and left in an oven at 40°C , to equilibrate for about two weeks. For x-ray studies, the viscous samples were sucked into a glass capillary, flame sealed initially and later sealed with glue.

Bibliography

- [1] W. M. Gelbart, A. Ben-shaul, D. Roux, Eds., *Micelles, Membranes, Microemulsions, and Monolayers* (Springer Verlag, New York, 1994)
- [2] J. Israelachvili, *Intermolecular and Surface Forces*, 2nd edition (Academic Press, London, 1998)
- [3] C. Tanford, *The Hydrophobic Effect*, 2nd edition (Wiley, New York, 1980).
- [4] H. Wennerstrom and B. Lindman, *Physics Reports* **52**, 1 (1979).
- [5] M. E. Cates and S. J. Candau, *J. Phys. Condens. Matter* **2**, 6869 (1990).
- [6] X. Auvray, C. Petipas, R. Anthore, I. Ricco, and A. Lattes, *J. Phys. Chem.* **93**, 7458 (1989).
- [7] N. Boden, K. W. Jolley, and M. H. Smith, *Liq. Cryst.* **6**, 481 (1989)
- [8] G. Strobl, *The Physics of Polymers*, 2nd edition, (Springer Verlag, Berlin, 1997)
- [9] A. Y. Grosberg and A. R. Khokhlov, *Statistical Physics of Macromolecules* (AIP Press, New York, 1994)
- [10] F. Oosawa, *Biopolymers* **6**, 1633 (1968); G. S. Manning, *J. Chem. Phys.* **51**, 924 (1969).
- [11] I. Rouzina, V. A. Bloomfield, *J. Phys. Chem.* **100**, 9977 (1996).
- [12] K. Wagner, D. Harries, S. May, V. Kahl, J. O. Raedler, and A. Benshaul, *Langmuir* **16**, 303 (2000).

[13] D. C. Champeney, *Fourier Transforms and their Physical Applications*, (Academic Press, London, 1973).

[14] D. Sherwood, *Crystals, X – rays and Proteins*, Longman, 1976.

Chapter 2

Phase behaviour of the CTAB–SHN–water system

2.1 Introduction

This chapter deals with the different liquid crystalline phases exhibited by cetyltrimethylammonium bromide (CTAB)– sodium-3-hydroxy-2-naphthoate (SHN)– water system. There have been some investigations on dilute solutions of this system mainly using electron and polarising microscopy, which revealed a cylinder to bilayer transition of the surfactant aggregates at $[\text{SHN}]/[\text{CTAB}] \sim 0.6$. These earlier studies are discussed in section 2.2. We have characterized the mesophases of this system using x-ray diffraction and optical microscopy. At low SHN concentrations a hexagonal phase is observed. However at higher SHN concentrations, a reentrant lamellar (L_α^D) \rightarrow centered rectangular (R) \rightarrow lamellar (L_α) transition is found on decreasing the water content. These experimental observations are discussed in section 2.3. X-ray diffraction data indicate that the lamellar phase at low surfactant concentration (L_α^D) differs from that observed at high concentrations (L_α). The former structure (L_α^D) contains slits or pores in the plane of the bilayer. Some of the earlier experimental as well as theoretical studies on L_α^D to L_α transformations are described in section 2.4. In the L_α^D phase seen in other systems, the defects are found to disappear gradually on increasing the surfactant concentration. A similar behaviour is seen in the present system at high temperatures. However at low temperatures, a centred rectangular structure appears between the two lamellar phases. This is the first report of such a phase behaviour in surfac-

tant systems. This novel phase behaviour and other results of these studies are discussed in detail in section 2.5.

2.2 Earlier studies

Previous studies on the CTAB-SHN surfactant system were in the context of the formation of worm-like micelles [1]. At low surfactant concentrations (5 - 20 wt %) CTAB forms short rod-like micelles in aqueous solutions. The viscosity of these solutions remains low, nearly the same as that of water. Organic salts like sodium salicylate are known to induce the formation of 'worm-like' micelles in CTAB, which are long (~ 100 nm), flexible (persistence length ~ 10 nm) cylindrical micelles [2]. These micelles can become entangled to form a viscoelastic gel at low surfactant concentrations. NMR studies have shown that in CTAB-SHN micelles, the SHN molecule is oriented so as to keep its naphthalene moiety in the hydrophobic region of the micelle. At α ($=[\text{SHN}]/[\text{CTAB}]$) ~ 0.67 , a turbid, birefringent phase appears, followed by a thick birefringent precipitate at equimolar ratios of CTAB and SHN. The turbid phase was initially characterized as nematic using polarizing microscopy. However, subsequent studies on cetyltrimethylammonium 3-hydroxynaphthalene-2-carboxylate (CTAHNC) (obtained from equimolar ratios of CTAB and SHN) revealed the presence of vesicles and the birefringent phase was shown to be lamellar [3]. The vesicles could be transformed into worm-like micelles by shearing as well as by increasing the temperature [4]. The rich phase behaviour of these systems prompted Horbaschek et al. [5] to study the dilute CTAB-SHN system in detail. The sequence of phases seen in a 100 mM CTAB solution, on varying the SHN concentration, is summarized in table 2.1. Symmetry of the phase behaviour observed about the equimolar mixture is similar to that found in some mixed-surfactant systems [6].

On increasing the temperature of equimolar CTAB-SHN mixture, where a precipitate is observed at low temperatures, an isotropic to lamellar transition is found at 70°C . Rheo-

Table 2.1: Phase behaviour of CTAB-SHN-water system at different SHN concentrations characterized through polarizing microscopy [5]. CTAB concentration in the dilute solution is 100 mM.

[SHN](mM)	Phase behaviour	no of Phases
50	isotropic viscoelastic gel	1
60	isotropic coacervate phase appears in the gel phase	2
> 60	lamellar phase appears in the coacervate phase	3
64	lamellar phase coexists with an isotropic phase	2
70	lamellar	1
> 90	appears turbid	1
100	a thick precipitate is formed	1
105	a turbid white suspension	1
119	turbidity decreases	1
120	isotropic and lamellar	2
122	an isotropic coacervate phase appears as the densest phase	3
140	lamellar phase disappears	2
150	isotropic phase	1

logical studies on the lamellar phase of the system show that the viscosity of this phase is much lower than that of the viscoelastic gel phase observed at lower SHN concentrations. No phase transitions are observed on shearing. Polarizing and electron microscopy on equimolar mixtures indicate multilamellar vesicles that stick together with an interlamellar distance less than 10 nm. Electron microscopy also reveals multilamellar vesicles, extended lamellar tubuli and stacks of bilayers in the lamellar phase.

Though dilute solutions of CTAB-SHN have been investigated in some detail, as discussed above, the phase behaviour of this system at higher surfactant concentrations has not been probed. Hence we have characterized the concentrated solutions using x-ray diffraction and polarizing microscopy.

2.3 Liquid crystalline phases of CTAB-SHN-water system

The phase behaviour was studied in detail at four different SHN concentrations corresponding to $\alpha = 0.25, 0.43, 0.67$ and 1.0 . The total surfactant concentration was varied in the range



Figure 2.1: Flow birefringence of the isotropic phase of CTAB-SHN-water system ($\alpha = 0.25$) observed between crossed polarizers on shearing at 30 °C. The birefringence observed here (indicated by the bright regions) occurs due to the flow of the sample trapped between air bubbles.

10% to 80% by weight. At low SHN concentrations ($\alpha = 0.25$), an isotropic viscoelastic gel which is flow birefringent (fig 2.1) is observed at low surfactant concentrations. Microscopic observations show a texture characteristic of a hexagonal phase at ϕ_s [= wt of surfactant/(wt of water+surfactant)] ~ 0.4 , at 30°C (fig 2.5). X-ray diffraction shows two peaks in the small angle region with the magnitude of scattering vectors q in the ratio $1:\sqrt{3}$ (fig 2.2a). These reflections correspond to the (1 0) and (1 1) planes of a 2D hexagonal lattice. These studies also indicate that the lattice parameter decreases as ϕ_s increases (table 2.3). On heating, no phase transitions occur in the system up to 90°C. At very low water content, corresponding to $\phi_s \sim 0.7$, a crystalline phase appears at low temperatures, which on heating transforms to a hexagonal texture at 50°C. The x-ray diffraction data consist of three peaks at 5.41 nm, 4.56 nm and at 2.28 nm (fig 2.2b). A long exposure in our experimental set up did not reveal any additional peaks. The presence of only two independent reflections makes it impossible to unambiguously determine the structure of this phase. Nevertheless, it is likely to be a rectangular phase. The phase diagram deduced from the data is given in fig 2.3. The d-spacings and the lattice parameters of the hexagonal phase are given in table 2.2.

On increasing the SHN concentration to $\alpha \sim 0.43$, an isotropic phase is observed at low surfactant concentrations (up to $\phi_s \sim 0.3$). Microscopic observations reveal that on increas-

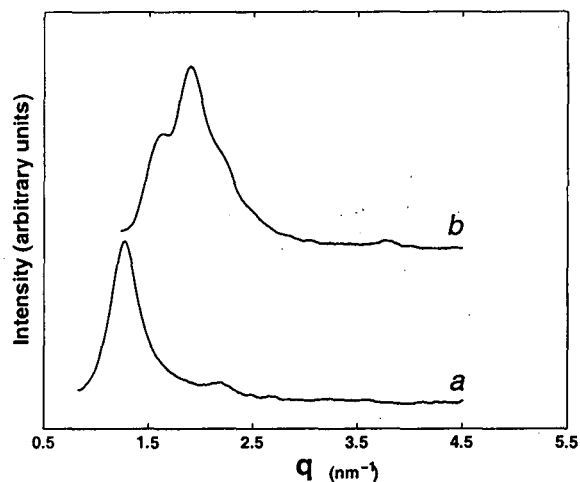


Figure 2.2: Diffraction data of CTAB-SHN-water system at $\alpha = 0.25$, and $\phi_s = 0.5$ (a); $\phi_s = 0.7$ (b).

Table 2.2: The d-spacings, lattice parameters (a) and the mesophases in CTAB-SHN-water at $\alpha = 0.25$ at 30°C . ϕ_s is the total surfactant concentration (wt %).

ϕ_s	$d_1(\text{nm})$	$d_2(\text{nm})$	a (nm)	phase
40	6.13(s)		7.08	hexagonal
50	5.59(s)	3.22(w)	6.45	hexagonal
60	5.12(s)	2.96(w)	5.92	hexagonal

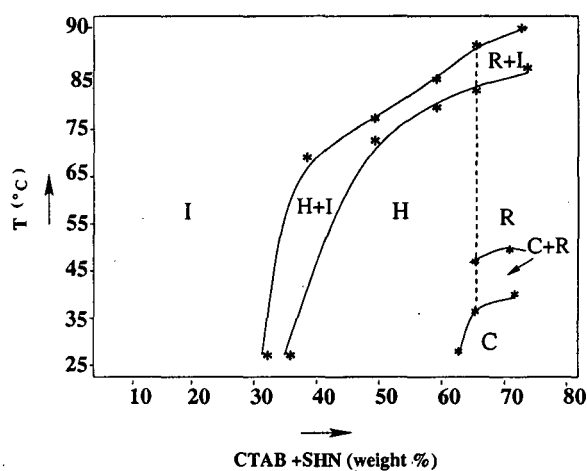


Figure 2.3: Phase diagram of CTAB-SHN-water system at $\alpha = 0.25$. I, H, R and C denote the isotropic, hexagonal, rectangular and crystalline phases respectively. The boundary between the H and R regions has not been precisely determined.

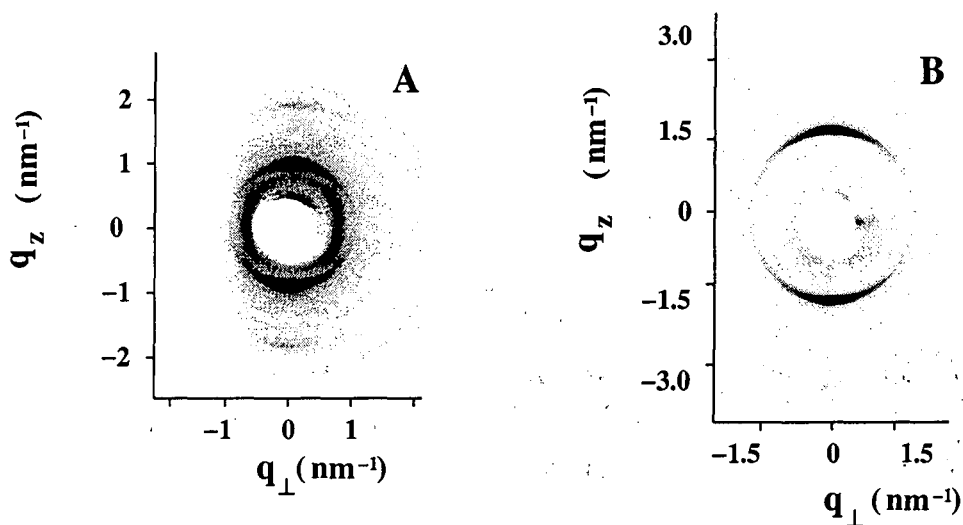


Figure 2.4: Typical diffraction patterns of a lamellar phase with defects (A) and a lamellar phase without defects (B). The diffraction pattern given here corresponds to $\alpha=1$ and $\phi_s = 0.5$ (A); 0.8 (B), though similar behaviour is seen at $\alpha = 0.43$ and 0.67 .

ing the surfactant concentration, a lamellar texture (fig 2.6) coexists with the isotropic phase up to $\phi_s \sim 0.5$ at 30°C . Thus a large coexistence region with the isotropic phase is observed here. On increasing the temperature, lamellar texture disappears leading to the formation of an isotropic phase. These solutions, unlike those at room temperature, were found to be highly viscous. The lamellar to isotropic transition temperature increases with the surfactant concentration. The lamellar texture is observed over a narrow range of surfactant concentration. Further increase of surfactant concentration to $\phi_s \sim 0.6$ leads to the appearance of two coexisting phases. The texture of one of them is lamellar. The other is similar to that seen in a hexagonal phase (fig 2.5). We refer to this henceforth in this chapter as the hexagonal texture though it may not be unique to the hexagonal phase. On heating they undergo a phase transition to a lamellar texture. With increase in ϕ_s , the transition temperature initially increases and later decreases. At $\phi_s \sim 0.7$, only a hexagonal texture is observed at 30°C . On heating, transition to a lamellar texture occurs through a coexistence region. On cooling back to 30°C , a typical texture appears which was not present before heating (fig 2.7). At high surfactant concentration, at around $\phi_s \sim 0.8$, a lamellar texture reappears at 30°C (fig 2.8).

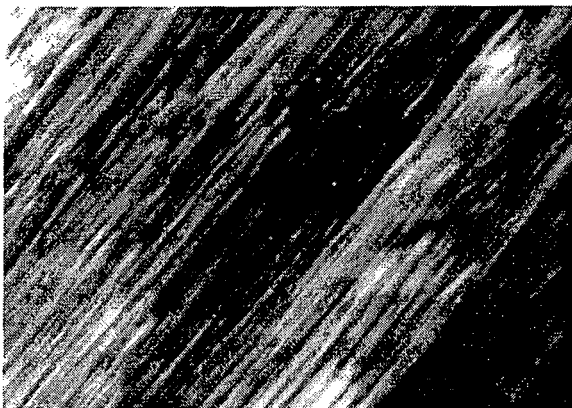


Figure 2.5: Typical texture of the hexagonal phase of CTAB-SHN-water system when observed between crossed polarizers at 30 °C.



Figure 2.6: Typical texture of the lamellar phase with defects (L_α^D) when observed between crossed polarizers at 30 °C.



Figure 2.7: Typical texture of the ribbon phase (R) observed between crossed polarizers, on cooling from the L_α phase.



Figure 2.8: Typical texture of the lamellar phase without defects (L_α) when observed between crossed polarizers, at 30 °C.

The x-ray diffraction pattern of an oriented sample at $\phi_s = 0.5$, shows two peaks with their q values in the ratio 1:2 (fig. 2.4A). These correspond to reflections from a lamellar structure. In addition, a diffused peak is observed at small angles, oriented perpendicular to the lamellar peaks. This peak corresponds to scattering from the plane of the bilayers. At $\phi_s \sim 0.6$, 6 peaks appear in the diffraction pattern. One of them, which is very weak, occurs at the same value as the first order lamellar peak at $\alpha = 0.5$. The remaining 5 peaks can be indexed as the reflections from the (1 0), (0 1), (1 1), (1 $\bar{2}$) and (0 2) planes of a 2D oblique lattice. At $\phi_s \sim 0.7$, only two peaks occur. It is likely that these peaks also correspond to a 2D oblique lattice. At $\phi_s \sim 0.8$, one peak is observed in the small angle region. Since the microscopic studies indicate a lamellar texture, we conclude that this corresponds to a lamellar reflection. In the oriented sample of the lamellar phase, the diffuse peak oriented perpendicular to the lamellar peak is absent (fig. 2.4B). The phase diagram obtained from these studies is given in fig 2.9. The lattice parameters of the various structures are given in table 2.3.

Table 2.3: The lattice parameters and the mesophases in CTAB-SHN-water at $\alpha = 0.43$ at 30°C . vs, s, w and vw indicates the strength of the various reflections with vs being the strongest reflection and vw the weakest reflection. a b denote the lattice parameters.

ϕ_s (wt%)	d_1 (nm)	d_2 (nm)	d_3 (nm)	d_4 (nm)	d_5 (nm)	d_6 (nm)	a (nm)	b (nm)	γ	phase
40	5.72 (s)						5.72			$L_\alpha^D + I$
45	5.35 (s)	2.68 (w)					5.35			L_α^D
50	5.24 (s)	2.59 (w)					5.24			L_α^D
60	7.03 (s)	5.24 (vw)	4.75 (vs)	3.29 (vw)	2.71 (vw)	2.39 (vw)	7.94	5.36	117.7°	$O + L_\alpha^D$
65	6.81 (s)	5.24 (vw)	4.7 (vs)	3.25 (vw)	2.64 (vw)	2.38 (vw)	7.61	5.36	116.5°	$O + L_\alpha^D$
70	6.08 (s)	4.51 (vs)								O
80	3.94 (s)							3.94		L_α

With further increase in SHN concentration to $\alpha \sim 0.67$, microscopic observations indicate an isotropic phase up to $\phi_s \sim 0.2$ at 30°C . On increasing the surfactant concentration, we see the coexistence of a lamellar texture with the isotropic phase. The isotropic phase disappears at around $\phi_s \sim 0.4$. The lamellar texture persists up to $\phi_s \sim 0.55$ beyond which a hexagonal texture appears along with domains of lamellar texture. At $\phi_s = 0.6$ however only a hexagonal texture is observed. This remains so up to $\phi_s = 0.7$. Beyond this, a lamellar texture reappears. The phase behaviour observed on heating were found to be similar to that at $\alpha = 0.43$, described above (fig 2.10). At $\phi_s = 0.5$, the diffraction patterns of the oriented sample consists of three peaks in the small angle region. A diffused peak at around 7.8 nm is oriented perpendicular to two sharp peaks at 5.82 nm and 2.91 nm, which indicate a lamellar structure. But the peak positions do not shift on heating up to 60°C . In our experimental set up the largest distances that can be measured is about 8 nm. Hence it is possible that the diffused peaks are present in the lamellar phase at lower surfactant concentrations, but have not been observed. At $\phi_s = 0.55$, the diffused peak is replaced by a sharp peak at 7.02 nm and a very strong peak at 5.29 nm. Three very weak reflections are also observed at 3.61 nm, 2.97 nm and 2.06 nm respectively. They could be indexed as the (2 0), (1 1), (3 1), (0

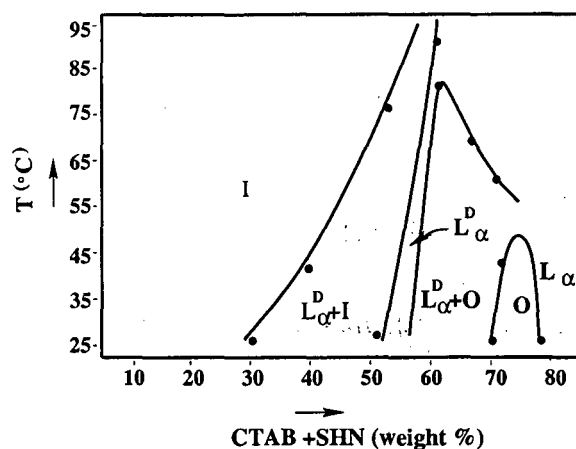


Figure 2.9: Phase diagram of CTAB-SHN-water system at $\alpha \sim 0.43$. L_{α}^D , O, L_{α} and I denotes the lamellar phase with defects, a ribbon phase with a 2D oblique lattice, a lamellar phase without defects and the isotropic phase respectively.

Table 2.4: The d-spacings, lattice parameters and the mesophases in CTAB-SHN-water at $\alpha = 0.67$ at 30°C . a and b denote the lattice parameters.

ϕ_s	$d_1(\text{nm})$	$d_2(\text{nm})$	$d_3(\text{nm})$	$d_4(\text{nm})$	$d_5(\text{nm})$	a (nm)	b (nm)	phase
42.5	6.89							L_{α}^D
45	6.35					6.35		L_{α}^D
47.5	5.97							L_{α}^D
50	7.8	5.82(s)	2.91(w)			5.82		L_{α}^D
52.5	7.66	5.49						L_{α}^D
55	7.02(s)	5.29(vs)	3.61(vw)	2.97(vw)	2.66(vw)	14.04	5.84	R
60	6.61(s)	4.88(vs)	3.31(vw)	2.73(vw)	2.44(vw)	13.0	5.42	R
70	6.08(s)	4.79(vs)	3.14(vw)	2.61(vw)	2.36(vw)	11.96	5.22	R
80	3.91(s)					3.91		L_{α}

2) and (2 2) reflections from a 2D centered rectangular lattice. However at $\phi_s \sim 0.8$, only one peak was observed at 3.91 nm (fig. 2.4B). Since the microscopic observations indicate a lamellar texture we can conclude that this peak arises from a lamellar structure. The lattice parameters of these phases at different surfactant concentrations are given in the table 2.4.

At low surfactant concentrations ($\phi_s = 0.1$), a precipitate which phase separates at the top of the solution is seen in the CTAB-SHN mixture at $\alpha \sim 1.0$. Maltese crosses indicating the presence of multi-lamellar vesicles are observed under a polarizing microscope at 30°C (fig 2.11). On heating, an isotropic phase is observed. When the surfactant concentration is

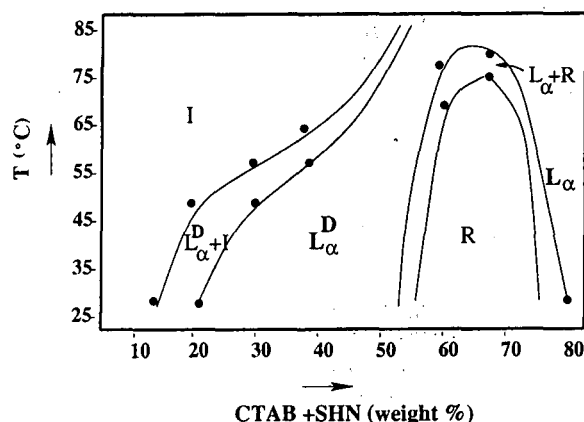


Figure 2.10: Phase diagram of CTAB-SHN-water system at $\alpha \sim 0.67$. L_{α}^D , R, L_{α} and I denotes the lamellar phase with defects, the centred rectangular phase, the lamellar phase without defects and the isotropic phase.

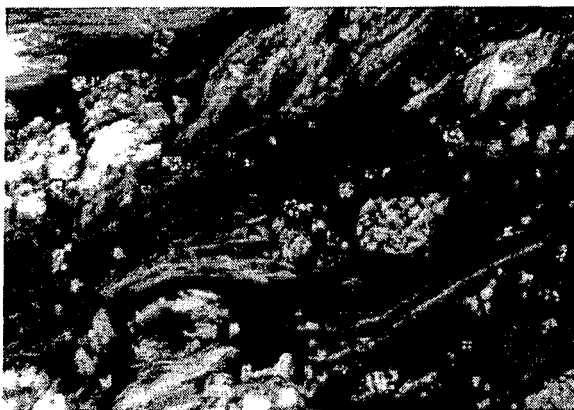


Figure 2.11: Typical texture of the multilamellar vesicles of the equimolar mixture of CTAB-SHN-water system ($\phi_s = 0.1$) when observed between crossed polarizers at 30°C .

increased, the precipitate dissolves and the solution appears turbid. This behaviour persists up to $\phi_s \sim 0.3$. At $\phi_s = 0.3$, a lamellar texture is observed, which on heating transforms to an isotropic phase through a coexistence region. A similar phase behaviour is observed up to $\phi_s = 0.525$ beyond which a hexagonal texture appears. On heating, the hexagonal texture transforms into lamellar. At high surfactant concentrations a lamellar texture is observed ($\phi_s = 0.7$). Thus we find that though there is a shift in the phase boundaries as the SHN concentration is increased, the phase behaviour remains nearly the same in the range $0.43 < \alpha < 1$.

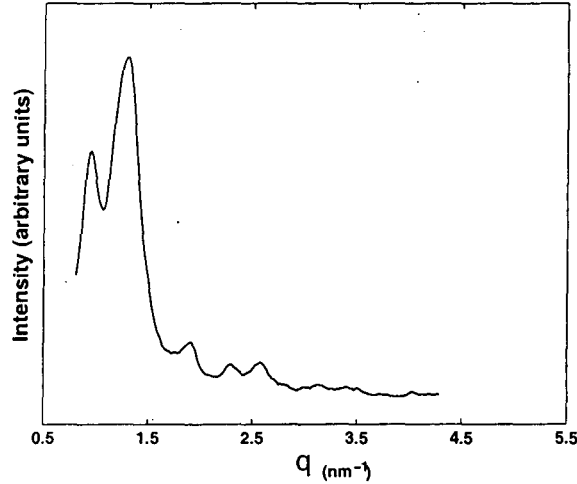


Figure 2.12: Diffraction data of CTAB-SHN-water system at $\alpha = 1$, $\phi_s = 0.6$.

X-ray diffraction studies at 30°C of the CTAB-SHN mixture at $\phi_s = 0.1$ show two peaks at 4.81 nm and 2.4 nm indicating a lamellar phase (fig 2.4A). No diffraction peaks were observed up to 8 nm in the small angle region up to $\phi_s = 0.3$. At $\phi_s = 0.4$, two peaks observed in the small angle region consists of a strong reflection at 7.3 nm and a weak reflection at 3.65 nm, indicating a lamellar structure. On increasing the surfactant concentration, the diffraction pattern of the oriented sample shows two lamellar peaks and a diffuse peak oriented perpendicular to it. We also find that at similar surfactant concentrations, the diffuse peak occurs at larger angles for higher values of α . For example, at $\phi_s = 0.5$, the diffuse peak shifts from 7.8 nm at $\alpha = 0.67$ to 7.45 nm at $\alpha = 1.0$. At $\phi_s \sim 0.525$, five peaks are observed in the small angle region which can be indexed on a 2D centred rectangular lattice (fig 2.12). At $\phi_s \sim 0.7$, a strong reflection at 5.63 nm, a very strong reflection at 4.12 nm and a weak reflection at 2.06 nm are observed. Long exposure in our set up did not reveal additional peaks. Since microscopic studies indicate domains of lamellar and hexagonal textures, it is likely that the first peak corresponds to the (1 1) reflection of a centered rectangular phase. The second and third peaks would then correspond to a lamellar phase. The structures and their lattice parameters are tabulated below (table 2.5). The phase diagram is given in fig 2.13

Partial phase diagram of the tertiary CTAB-SHN-water system is shown in figure 2.14.

Table 2.5: The d-spacings, lattice parameters and the mesophases in CTAB-SHN-water at $\alpha= 1.0$ at 30°C . a and b denote the lattice parameters.

ϕ_s	$d_1(\text{nm})$	$d_2(\text{nm})$	$d_3(\text{nm})$	$d_4(\text{nm})$	$d_5(\text{nm})$	a (nm)	b (nm)	phase
10	4.81(s)	2.4(w)				4.81		L_α^D+I
40	7.3(s)	3.65(w)				7.3		L_α^D
50	7.45	5.85(s)	2.93(w)			5.85		L_α^D
55	6.89(s)	5.51(vs)	3.68(vw)	2.75(vw)		13.78	6.0	R
60	6.55(s)	5.07(vs)	3.46(vw)	2.86(vw)	2.57(vw)	12.9	5.72	R
70	5.63(s)	4.12(vs)	2.06(w)					$R+L_\alpha$

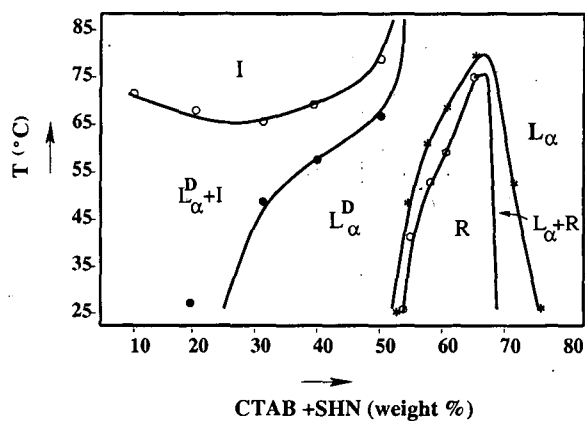


Figure 2.13: Phase diagram of CTAB-SHN-water system at equimolar ratios of CTAB and SHN. L_α^D , R, L_α denotes the lamellar phase with defects, centred rectangular phase and lamellar phase without defects respectively.

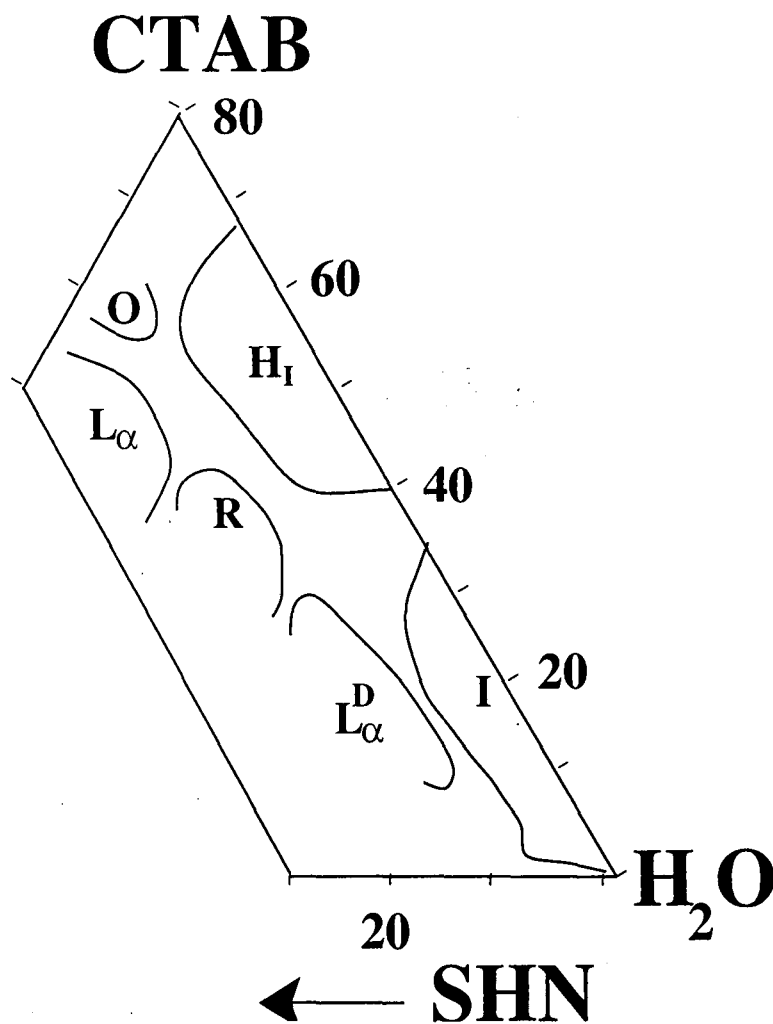


Figure 2.14: Partial phase diagram indicating the various liquid crystalline phases of CTAB-SHN-water system at 30 °C. L_{α}^D denotes the lamellar phase with defects, O denotes the 2D oblique phase, R the centred rectangular phase, I the isotropic phase, L_{α} the lamellar phase without defects and H, the hexagonal phase

Five single phase regions are found corresponding to the isotropic (I), hexagonal (H), rectangular (R), oblique (O), lamellar phases with and without defects (L_{α}^D , L_{α}). The presence of the 2D oblique phase in between H and L_{α} is similar to the phase behaviour seen in some surfactant systems [7]. However, as discussed below the formation of a 2D centred rectangular phase in between two lamellar phases has not been seen earlier.

2.4 Curvature defects in lamellar phases

Bilayers with pores or slits have been observed in some surfactant systems like cesium pentadecafluorooctanoate (CsPFO) -water [8]. CsPFO forms disk-like micelles in dilute solutions, which become orientationally ordered to give a nematic phase on increasing the surfactant concentration. A lamellar phase is observed at higher surfactant concentrations. X-ray diffraction studies on these systems reveal a diffused peak at small angles in addition to the set of peaks which arises due to the lamellar periodicity. Since the ionic conductivity measurements do not show a discontinuity across the nematic to lamellar transition, it was proposed that the lamellar phase was made up of disk-like micelles arranged in layers [9]. However the scattering from such an array of disk-like micelles separated by a continuous medium cannot be distinguished from the scattering from water filled pores in a continuous bilayer. Further experimental studies were carried out on these systems using small angle neutron scattering techniques as well as water diffusion experiments on oriented bilayers [10]. They showed that the bilayers consist of pores filled with water. The pores heal on adding $CsCl_2$ or on increasing the surfactant concentration, to form a lamellar phase without defects.

Such curvature defects are also found in mixed-surfactant systems [11]. Neutron scattering studies on SDS-alcohol-water system find that the number of defects per unit area increases as the SDS/alcohol ratio increases. However the pores disappear gradually when the water content is decreased. Similar defects occur in mixtures of dimyristoylphosphatidyl choline (DMPC) with a shorter chain lipid dihexanoylphosphatidyl choline (DHPC) [12]. These mixtures form disk-like aggregates called bicelles at low surfactant concentrations. Small angle neutron scattering studies show that at higher temperatures, they form a lamellar phase consisting of bilayers with pores. These pores are expected to arise when DHPC phase separates to the edges of the bilayer or to the rim of the pores.

There have also been some theoretical studies on curvature defects in bilayers, which predict a transformation from stripes to random lines to pores on increasing the surfactant concentration [13]. The stripe phase consists of slits in the plane of the bilayer, parallel to each other. The random lines are obtained as the slits meet leading to random cuts in the plane of the bilayer. The pores form as the slits within each bilayer close upon themselves. The origin of these defects may be qualitatively understood as follows. Each defect or pore is made of a semitoroidal rim or edge. If the amphiphile locally prefers a curved surface as compared to a flat region, the overall free energy of the system can be lowered by the creation of these edges or pores in the bilayer. The surfactants that would have occupied the pores can be accommodated in two ways: i) by decreasing the area per surfactant molecule in the bilayer; this leads to a stretching of the tails of the amphiphiles and hence to an increase in the thickness of the bilayers, ii) by creating more bilayers; this however decreases the interlamellar separation. Thus creation of pores decreases the packing entropy. If the surfactants are charged, as in the CsPFO-water system, the electrostatic repulsion between the edges in adjacent bilayers also cost energy, as the surfactant concentration increases. Hence at lower water content, when the interlamellar interactions become significant, the pores disappear. The increase in the density of defects, as the SDS/alcohol ratio increases indicate that SDS prefers curved regions locally. This may also lead to a phase separation of the SDS and alcohol molecules with further loss of entropy.

2.5 Discussion

The isotropic phase at $\alpha \sim 0.25$ consists of worm-like micelles. This is indicated by the high viscosity as well as by the flow birefringence observed on shearing these samples. The growth of these long flexible micelles is the consequence of the decrease in the spontaneous curvature of the CTAB cylinders in the presence of SHN. CTAB forms a hexagonal phase over a wide range of surfactant concentration. Therefore, the observation of a hexagonal phase at low SHN concentrations ($\alpha \sim 0.25$) is not surprising. However at very low water

content a crystalline phase is obtained at 30°C , since the Kraft temperature of CTAB increases with surfactant concentration [14]. The rectangular phase at 50°C obtained at $\phi_s \sim 0.7$, is usually observed in surfactant systems in between the hexagonal and lamellar phases as the water content is lowered. This is formed by long aggregates with an almost elliptical cross-section, known as ribbons. These ribbons are arranged on a 2D rectangular lattice. At higher surfactant concentrations the ribbons merge to form bilayers, thus leading to a lamellar structure.

The isotropic phase at $\alpha \sim 0.43$ could be made up of long rod-like micelles, since the viscosity of these mixtures is found to be higher than that of the lamellar phase. The formation of an isotropic, viscoelastic gel on heating from the L_{α} phase at higher surfactant concentration, indicates that vesicular aggregates undergo a change in shape to form long flexible rod-like micelles that get entangled.

The observation of the lamellar phase at higher surfactant concentrations, is in confirmation with earlier studies on dilute mixtures of CTAB-SHN: However we find that the lamellar phase occurs earlier, that is, at a lower ϕ_s on increasing α . In the diffraction pattern of the oriented sample, the orientation of the diffused peak perpendicular to the lamellar peaks indicate that they arise from some structure in the plane of the bilayer. The diffused peaks observed here have been reported earlier in a few surfactant systems where they are believed to arise from pores in the plane of the bilayer, as discussed in section 2.4. Hence we surmise that in the CTAB-SHN system also curvature defects are present in the plane of the bilayer. Since no x-ray diffraction studies have been carried out till now, this is the first report of these defects in the present system. The isotropic solution at $\alpha \sim 0.67$ is most probably made up of vesicles since the viscosity of the solution is found to be low.

The lamellar phase exists over a wide range of surfactant concentration at $\alpha \sim 0.67$, indicating the existence of long range repulsion between the bilayers which allows them to swell.

One possible origin of such a repulsion is electrostatic interaction between the charged bilayers. The interaction energy per unit area between two planar surfaces of charge density σ , separated by a distance z is given by [15]

$$V_{el}(z) = \frac{2\sigma^2\lambda_D}{\epsilon\epsilon_0} e^{-z/\lambda_D}$$

where σ is the surface charge density, λ_D the Debye length, ϵ and ϵ_0 , the dielectric constant of the medium and the dielectric permittivity of free space respectively. If χ is the ionic strength of the solution, then $\lambda_D = \left[\frac{\epsilon\epsilon_0 k_B T}{4\pi\chi e^2}\right]^{1/2}$. k_B is the Boltzmann constant and T the temperature.

In the lamellar phase of CTAB-SHN-water system, due to the release of the Br^- and Na^+ counter ions into the solution, the effective salt concentration is high and the Debye length is < 1 nm. On the other hand, the thickness of the water layer separating the bilayers is > 2 nm. Therefore, electrostatic repulsion between adjacent bilayers in the lamellar phase can be expected to be negligible and cannot account for the observed swelling behaviour.

The other possible origin of the interbilayer repulsion is the steric interaction between the bilayers due to thermal undulations of the bilayers [16]. The steric interaction energy per unit area between two bilayers separated by a distance z is

$$V_u(z) = 3\pi^2 (k_B T)^2 / 128\kappa z^2$$

where κ is the rigidity modulus of the bilayer, k_B the Boltzmann constant and T the temperature. This repulsive interaction can be increased either by increasing the temperature or by increasing the flexibility of the bilayers. The addition of alcohol is known to lower the bending rigidity of bilayers by an order of magnitude [17]. This in turn is found to increase the bilayer separation by two orders of magnitude. Since the electrostatic interactions can be ruled out in the CTAB-SHN-water system, we surmise that a steric repulsion, stabilizes the lamellar phase over a large range of surfactant concentration. It would indicate that the CTAB-SHN bilayers are highly flexible, but we have not measured κ independently.

The absence of any shift in the peak positions in the diffraction pattern on increasing the temperature indicates that the separation between the bilayers as well as the separation between the defects in the plane of the bilayer do not change up to 60° C. This leads us to conclude that the defect density does not alter with temperature. No clear picture exists at present regarding the structure of these defects. Since the defects are not oriented in the plane of the bilayer, it is difficult to extract any information regarding the form factor of these defects from the x-ray diffraction data. Hence it is not known whether these defects are pores or long slits in the plane of the bilayer. The size distribution of the defects, that is whether the pores or slits are polydisperse or monodisperse is also not known. But the presence of the ribbon phase at higher surfactant concentration indicates that these are most probably slits.

The appearance of multilamellar vesicles at low surfactant concentration in equimolar mixtures has not been understood at present. Also, the interlamellar separation increases as the surfactant concentration increases. Since one molecule of NaBr is released for every CTAB and SHN that associate to form a complex, the increase in surfactant concentration leads to the increase in the salt concentration in the surfactant solution. Swelling of the bilayers on increasing surfactant concentration is possibly due to the presence of salt. More work has to be done to understand this behaviour.

The formation of a centered rectangular structure in between the two lamellar phases is unusual. As far as we know, the CTAB-SHN-water system is the first to show such a behaviour. Normally the centered rectangular phase (R) appears in between the hexagonal and lamellar phases, similar to the behaviour observed in our system at $\alpha = 0.25$ described above. A 2D centered rectangular lattice can result if trans-bilayer correlations arise between the defects. 3D lattices of such defects have been observed in some lipid-polypeptide systems [18]. If the defects formed a centred rectangular structure, one of the lattice parameters would correspond to twice the lamellar periodicity. If we consider the lattice parameters of our system in the centred rectangular phase, say at $\alpha = 0.67$, $\phi_s = 0.55$, the lattice parameters

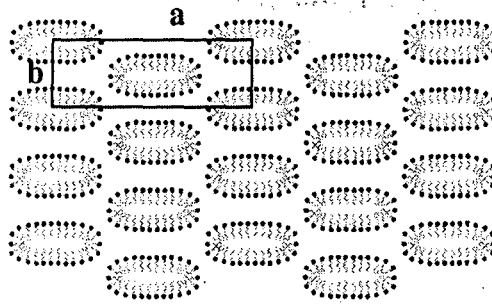


Figure 2.15: Schematic of the structure of the centred rectangular phase of CTAB-SHN-water system consisting of ribbon-like micelles arranged on a 2D rectangular lattice:

are found to be 14.04 nm and 5.84 nm. The periodicity of the lamellar phase at $\alpha=0.67$, $\phi_s = 0.525$ is 5.49 nm. Thus twice the lamellar periodicity of the lamellar phase close to the $L_\alpha^D \rightarrow R$ transition is not comparable to the lattice parameters observed in the centred rectangular structure. Moreover, in such a structure, the strongest reflection in the x-ray diffraction data would be from the (2 0) planes, which corresponds to the scattering from the bilayers and not from the (1 1) planes as observed here. Hence we can rule out a lattice arising from the 2D ordering of defects. This indicates that the centred rectangular structure seen here most probably consists of ribbon-like aggregates arranged on a 2D centred rectangular lattice (fig 2.15). Such structures have been seen before in some surfactant systems in between the hexagonal and lamellar phases [7].

The decrease in the separation between defects in the plane of the bilayer on increasing the SHN concentration indicates an increase in defect density. The fact that we find the centred rectangular phase at a lower surfactant concentration on increasing SHN concentration may be related to this. An increase in the defect density above a critical value, may lead to the formation of ribbon-like aggregates that form a 2D lattice. Further theoretical work is needed to understand this behaviour.

The absence of a diffuse peak in the lamellar phase at high surfactant concentrations

(L_α), indicates that the defects are absent in the plane of the bilayer. The transformation from a lamellar phase with defects (L_α^D) to one without defects (L_α) at high temperatures (fig 2.9,2.10,2.13) is similar to the behaviour seen in some surfactant systems, discussed in section 2.4. However the appearance of a centred rectangular phase (R) in between the two lamellar phases at lower temperatures cannot be understood in the framework of present theories.

2.6 Conclusions

Partial phase diagram of the tertiary system CTAB-SHN-water has been constructed. In addition, temperature-composition phase diagrams of the system at a few values of [SHN]/[CTAB] have also been determined. We find that the phase behaviour of this system is rather rich consisting of hexagonal, lamellar, oblique and centred rectangular structures. The $L_\alpha^D \rightarrow L_\alpha$ transformation that we observe here at high temperatures has been seen earlier in some surfactant systems. However the $L_\alpha^D \rightarrow R \rightarrow L_\alpha$ transition at lower temperatures has not been reported in any other surfactant system.

Bibliography

- [1] B. K. Mishra, S. D. Samant, P. Pradhan, S. B. Mishra, and C. Manohar, *Langmuir* **9**, 894 (1993).
- [2] M. E. Cates and S. J. Candau, *J. Phys. Condensed Matter* **2**, 6869 (1990).
- [3] R. A. Salkar, P. A. Hassan, S. D. Samant, B. S. Valaulikar, V. V. Kumar, F. Kern, S. J. Candau, and C. Manohar, *Chem. Commun.* **10**, 1223 (1996).
- [4] E. Mendes, J. Narayanan, R. Oda, F. Kern, S. J. Candau, and C. Manohar, *J. Phys. Chem. B* **101**, 2256 (1997).
- [5] K. Horbaschek, H. Hoffmann, and C. Thunig, *J. Colloid Interface Sci.* **206**, 439 (1998).
- [6] C. A. Baker, D. Saul, G. J. T. Tiddy, B. A. Wheeler, E. Willis, *J. Chem. Soc., Faraday Trans.* **70**, 154 (1974).
- [7] Y. Hendrikx and J. Charvolin, *J. de Physique* **42**, 1427 (1981).
- [8] M. S. Leaver and M. C. Holmes, *J. Phys. II France* **3**, 105 (1993).
- [9] M. C. Holmes, D. J. Reynolds, and N. Boden, *J. Phys. Chem.* **91**, 5257 (1987).
- [10] M. C. Holmes, P. Sotta, Y. Hendrikx, and B. Deloche, *J. Phys. II France* **3**, 1735 (1993).
- [11] Y. Hendrikx, J. Charvolin, P. Kekicheff, and M. Roth, *Liq Cryst.* **2**, 677 (1987).
- [12] M. Nieh, C. J. Glinka, S. Kroeger, R. S. Prosser, and J. Katsaras, *Langmuir* **17**, 2629 (2001).

- [13] C. K. Bagdassarian, D. Roux, A. Benshaul, and W. M. Gelbart, *J. Chem. Phys.* **94**, 3030 (1991).
- [14] X. Auvray, C. Petipas, R. Anthore, I. Ricco, and A. Lattes, *J. Phys. Chem.* **93**, 7458 (1989).
- [15] J. N. Israelachvili, *Intermolecular and Surface Forces*, 2nd edition, Academic Press, London (1991).
- [16] W. Helfrich, *Z. Naturforsch* **33a**, 305 (1978).
- [17] C. R. Safinya, E. B. Sirota, D. Roux, G. S. Smith, *Phys. Rev. Lett.* **62**, 1134 (1989).
- [18] L. Yang, T. M. Weiss, R. I. Lehrer, and H. W. Huang, *Biophys. J.* **79**, 2002 (2000).

Chapter 3

Structures of cationic surfactant-DNA complexes

3.1 Introduction

This chapter deals with the structures exhibited by complexes of DNA with cetyltrimethylammonium bromide (CTAB) and with mixtures of CTAB and sodium-3-hydroxy-2-naphthoate (SHN). Detailed x-ray diffraction experiments have been carried out on complexes of DNA with mixtures of double-tailed cationic lipids like dioleoyltrimethylammonium propane (DOTAP) and neutral lipids like dioleoylphosphatidyl choline (DOPC) or dioleoylphosphatidyl ethanolamine (DOPE) in recent years, motivated by their potential biomedical applications. These are summarized in section 3.2. Complexation of DNA with the single-tailed cationic surfactant CTAB has been widely made use of in the extraction of DNA from plants. Nevertheless, no detailed studies have been reported on this system. CTAB forms cylindrical micelles in aqueous solution, unlike the double-tailed DOTAP, which forms bilayers. Hence CTAB-DNA complexes can be expected to form structures different from those exhibited by DOTAP-DOPC-DNA complexes. We have carried out x-ray and optical microscopy studies of CTAB-DNA complexes. These experiments described in section 3.3, reveal that the complexes have a two-dimensional (2D) hexagonal structure. However, there are two molecular packings that can result in such a lattice. In order to distinguish between these two possibilities, we have modelled the electron densities in these two structures and calculated the intensities of the diffraction peaks. This analysis, pre-

sented in section 3.4, clearly shows that the structure consists of DNA strands intercalated between cylindrical CTAB micelles. In section 3.5, we describe the structural modifications of CTAB-DNA complexes induced by the addition of SHN. We find that the structure of the complex changes from hexagonal to lamellar at a critical SHN concentration, very close to that at which a cylinder to bilayer transformation is found in the CTAB-SHN-water system. This observation further confirms the structure of the hexagonal complexes obtained from a modelling procedure. These experimental results are discussed in section 3.6. Finally, the conclusions drawn from the experiments described in this chapter are given in section 3.7 .

3.2 Earlier studies on surfactant-DNA complexes

Many of the earlier studies have been on DNA-cationic lipid systems. The earliest structure proposed in these systems, consists of liposomes attached to the DNA strands and known as the bead-on-string structure [1, 2]. Electron Microscopy studies have reported a variety of structures including oligolamellar structures [3] and tube like images indicating lipid bilayer covered DNA [4].

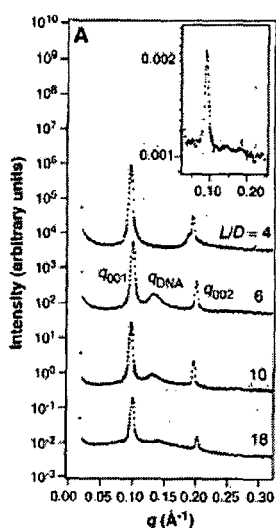


Figure 3.1: A series of SAXS scans of cationic lipid-DNA complexes in excess water as a function of different lipid to DNA weight ratio (L/D) [5]

Detailed x-ray diffraction studies [5, 6] have been carried out on complexes of DNA with

mixtures of cationic lipids like DOTAP or dimyristoyltrimethylammonium propane (DM-TAP) and neutral lipids like DOPC or DOPE. In the absence of DNA, x-ray studies on the dilute, equimolar lipid mixtures did not reveal any peaks in the small angle region indicating that the bilayer separations are larger than 10 nm. However in the presence of DNA, birefringent condensates coexist with a dilute aqueous solution. These complexes were studied for different values of ρ (= weight of cationic lipid/ weight of DNA). X-ray diffraction studies on these condensates (fig 3.1) reveal a set of peaks that correspond to a lamellar periodicity of 6.51 nm and an additional diffuse peak. As the DNA concentration is increased, ie for $\rho < \rho_{iso}$ (the concentration at the isoelectric point, where the negative charges on the DNA are neutralized by the positive charges of the cationic lipid), the position of the diffuse peak shifts from 4.4 nm to 3.7 nm. Based on these observations, a structure has been proposed, where the DNA is sandwiched between the cationic lipid bilayers (fig. 3.2) known as the intercalated lamellar phase (L_{α}^C) [5]. The bilayer thickness is around 3.9 nm and the diameter of DNA with a hydration shell is around 2.5 nm. Hence the DNA sandwiched between two bilayers would correspond to a periodicity of about 6.4 nm, which is consistent with the periodicities observed in these complexes. The diffused peak indicates positional correlations of the DNA strands in the plane of the bilayers. The shift in the DNA-DNA peak with DNA concentration arises due to an abrupt change in the separation between the DNA strands (d_{DNA}) across the isoelectric point. There are no transbilayer positional correlations of the DNA strands when the bilayers are in the fluid L_{α} phase. The DNA chains confined between the bilayers form a 2D smectic [7]. At lower temperatures, when the bilayers are in the L_{β} phase and hence more rigid, positional correlations arise across the bilayers and a 2D rectangular lattice (fig 3.3) of the DNA has been reported [8].

d_{DNA} can be calculated from the lamellar structure proposed for the complexes, if it is assumed that all the DNA strands are adsorbed between the bilayers at ρ_{iso} [5]. If ρ_D and ρ_L are the densities of DNA and lipid respectively, δ_m the membrane thickness, A_D the area of cross-section of a DNA double helix, L and D the weights of lipid and DNA respectively,

then the separation between the DNA strands,

$$d_{DNA} = (A_D \rho_D / \delta_m \rho_L)(L/D) \quad (3.1)$$

If the amounts of cationic lipid and DNA are fixed at ρ_{iso} and (L/D) is varied by changing the amount of the neutral lipid, then according to eqn 3.1, plot of d_{DNA} vs (L/D) must be linear. This was found to agree remarkably well with the variation of d_{DNA} observed on diluting the charge of the lipid membrane by the addition of a neutral lipid [5].

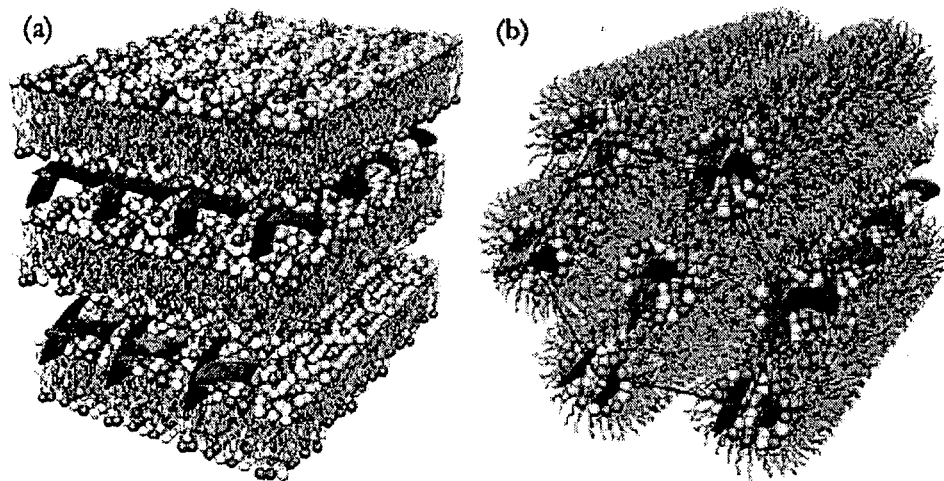


Figure 3.2: Proposed structures of the intercalated lamellar phase (a) and the inverted hexagonal phase (b) in lipid-DNA complexes [12].

Theoretical studies indicate that a variety of structures is possible in lamellar DNA-lipid complexes, like the isotropic lamellar, nematic lamellar, columnar, and sliding columnar phases, depending on the degree of ordering of the DNA strands [9]. In the isotropic lamellar phase, there is no long range or quasi long range positional or orientational order of the DNA strands. If long range orientational order arises between the DNA strands with no positional order, a nematic lamellar phase is obtained. In addition to the orientational order, when there are long range positional correlations between the DNA strands across the bilayers, we have a columnar phase with the DNA arranged on a 2D rectangular or a 2D centered rectangular lattice. The former structure results when the effective interactions between the DNA strands sandwiched between the bilayers is attractive. A centered rectangular phase

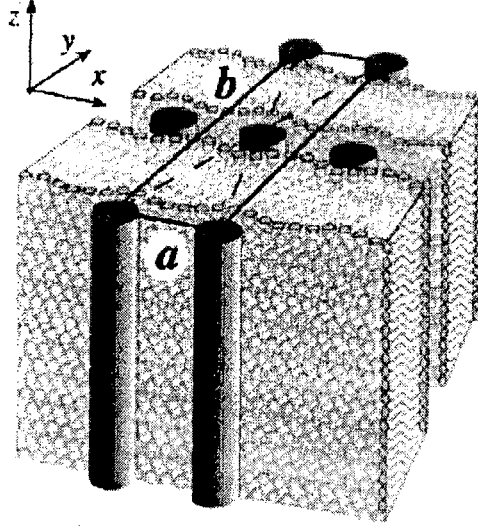


Figure 3.3: Local structure of the centered rectangular columnar DNA lattice embedded in a cationic lipid lamellar phase observed when the bilayers are in the L'_β phase [8].

would be observed when there is a repulsion between the DNA strands. Such a phase has been observed in some lipid-DNA systems as discussed above [8]. In addition to these, a sliding columnar phase has also been proposed with properties intermediate between the columnar and nematic lamellar phases. Here, in-plane smectic correlations decay as $\exp(-\ln^2 r)$ as a function of the DNA-DNA separation r . The positional correlation between these smectic lattices, die off exponentially with layer-number difference. Though it is very likely that the intercalated lamellar phase (L^C_α) is a sliding columnar phase, further confirmation would require monodomain samples. However to our knowledge such a phase has not yet been experimentally observed.

In lipid-DNA complexes, one would a priori expect that the separation between the DNA strands (d_{DNA}) would be determined by the isoelectric point, where the charges of the cationic lipid are neutralized by the charges on the DNA. Hence d_{DNA} should remain fixed at d_{DNA}^{iso} determined by the sample geometry [10].

$$d_{DNA}^{iso} = (A_D \rho_D / \delta_m \rho_L) (\rho_{iso} / (1 - \phi_{PC})) \quad (3.2)$$

where ϕ_{PC} (=weight of DOPC/total weight of the lipid).

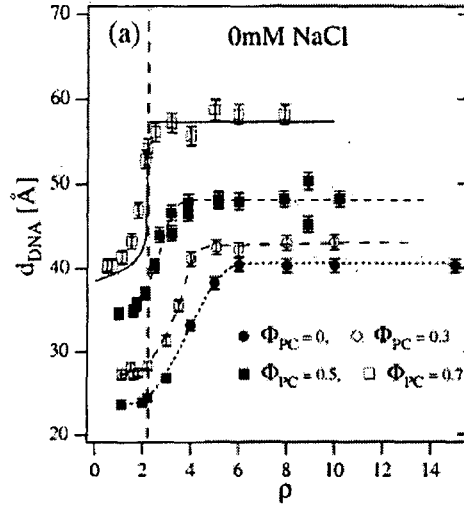


Figure 3.4: Variation of DNA packing with ρ in complexes with fixed ϕ_{PC} and no salt [10]. Vertical dashed line indicates isoelectric point. The solid line through the data at $\phi_{PC} = 0.7$ is the result of nonlinear Poisson-Boltzmann theory for complexes with low membrane charge density [11]

To verify this, d_{DNA} was measured for DOTAP-DOPC-DNA complexes at different values of ϕ_{PC} and ρ [10]. Microscopic observations confirm that the complex remains monophasic with no excess DNA or liposomes. The plot of d_{DNA} vs ρ at different values of ϕ_{PC} (fig 3.4) indicates an overall increase of d_{DNA} on increasing ϕ_{PC} due to the decrease in the bilayer charge density. The plot of d_{DNA} vs ρ follows the predicted behaviour only for $\rho = \rho_{iso}$ ($= 2.2$) (fig. 3.5). It is found that for $\rho \neq \rho_{iso}$ d_{DNA} deviates from d_{DNA}^{iso} . The complex structure has smaller d_{DNA} for $\rho < 2.2$ and a larger value of d_{DNA} for $\rho > 2.2$ (fig.3.4). However the structure remains constant away from the isoelectric point with fixed d and d_{DNA} . Electrophoresis experiments also show that complex is negatively charged for $\rho < 2.2$ and positively charged for $\rho > 2.2$.

The charge reversal of the complex at the isoelectric point implies that it absorbs excess cationic lipid when $\rho > \rho_{iso}$ and excess DNA when $\rho < \rho_{iso}$. A unit cell of the complex consists of a DNA strand of unit length and a bilayer of area d_{DNA} . The free energy per unit cell of a complex that acquires a positive charge by incorporating excess cationic lipid is

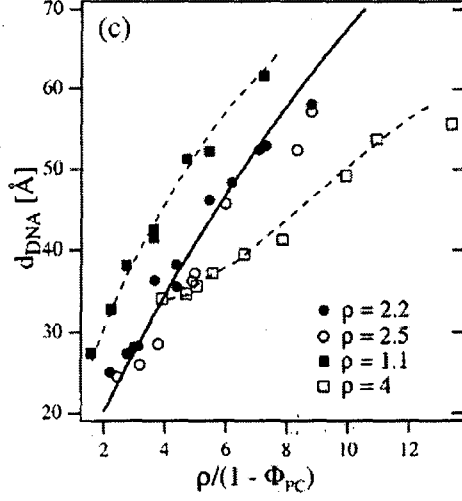


Figure 3.5: Variation of d_{DNA} with changing ϕ_{PC} in complexes with different fixed ρ . Solid line is the prediction from the geometry for isoelectric complexes [10].

given by [10]

$$F_C^+ = d_{DNA}[(1/e)(4k_B T \sigma^+)(\ln(2l_D/l_C) - 1) + \pi k_B T / l_B \delta_w] \quad (3.3)$$

where $\sigma^+ = \sigma_c(1 - d_{DNA}^{iso}/d_{DNA})$ is the excess cationic charge density of the complex, σ_c the charge density of the free bilayer, e the elementary charge, k_B the Boltzmann constant and T the temperature. The first term corresponds to the free energy of the bilayer surface in the complex consisting of excess cationic lipids. The Chapman length $l_C (= e/2 \pi \sigma^+ l_B)$, corresponds to the thickness of condensed counterion layer near the membrane surface and the Debye screening length $l_D \gg l_C$. The Bjerrum length $l_B = e^2/\epsilon k_B T$. The second term corresponds to the repulsion between the bilayers. δ_w is the thickness of the water layer in the complex.

The free energy of excess cationic membrane of length d_{DNA} in the aqueous solution is given by,

$$F_B = d_{DNA}[(1/e)(4k_B T \sigma_c)(\ln(2l_D/l_C) - 1)] \quad (3.4)$$

Since $\sigma^+ < \sigma_c$, the free energy of bilayer is higher in the aqueous solution than in the complex. The complex thus absorbs excess bilayer into it and lowers the free energy of the system by releasing the counterions into the complex. However the intake of cationic lipid is limited by the repulsion between the bilayers given by the second term in eqn (3.3). Also,

higher the charge density σ_c , of the bilayer, greater the amount of charged lipid which enters the complex. This was found to agree with the experimental observations.

For $\rho < \rho_{iso}$, the electrostatic energy per unit cell of the negatively charged complex is given by

$$F_C^- = \delta_w [(1/e)(4k_B T \sigma^-) (\ln(2l_D/l_C) - 1) + \pi k_B T / l_B d_{DNA}] \quad (3.5)$$

where $\sigma^- = \sigma_{DNA}(1 - d_{DNA}/d_{DNA}^{iso})$ is the excess anionic charge density in the complex and σ_{DNA} , the charge density of free DNA.

The free energy per unit length of free DNA is higher in solution than in the complex. The entropy of the counterions is lower for the free DNA since they are confined near the cylindrical surface. Since σ^- is lower than σ_{DNA} , the overall free energy of the system may be lowered by incorporating the free DNA into the complex. The intake of DNA is however limited by the repulsion between the DNA strands given by the second term in equation 3.5. In fig 3.5 the data points above ρ_{iso} line corresponds to complexes which have taken in excess DNA and those below ρ_{iso} line correspond to complexes with excess lipid. Thus the shift in the d_{DNA} curves from the predicted values at ρ_{iso} , confirms the overcharging phenomenon discussed above.

The structural changes of lipid-DNA complexes, on replacing the neutral lipid DOPC by DOPE, has been studied using x-ray diffraction [12]. At low values of ϕ_{DOPE} (\equiv weight of DOPE/total weight of the lipid), diffraction peaks indicate a lamellar structure for the complex similar to that observed in DOTAP-DOPC-DNA complexes. At $\phi_{DOPE} = 0.75$, four peaks are obtained (fig 3.6) which can be indexed as the (1 0), (1 1), (2 0) and (2 1) peaks of a 2D hexagonal lattice. The lattice parameter was found to be 6.74 nm. The DOPE-DOTAP bilayer thickness is around 4 nm. Also, pure DOPE forms an inverted hexagonal phase (H_{II}) in excess water [13, 14]. The observed lattice parameter of 6.8 nm is consistent with an inverted hexagonal structure (H_{II}^C) shown in fig 3.2 with a lipid monolayer thickness of 2 nm,

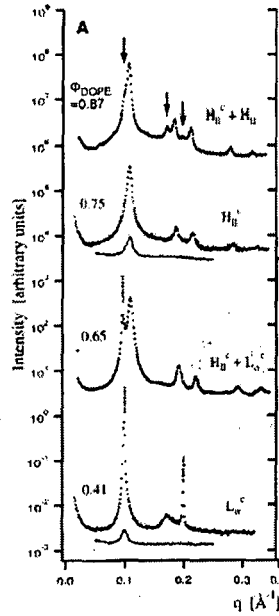


Figure 3.6: SAXS scans of cationic lipid-DNA complexes as a function of increasing ϕ_{DOPE} [12].

and an aqueous core of 2.8 nm diameter. Such a core can accommodate a DNA strand with two hydration shells.

The structure of the complex is determined by the elastic properties of the lipid membrane and the electrostatic interactions between the lipid and the DNA [15, 16]. In the inverted hexagonal phase, the neutralization of the negative charges on the DNA by the cationic lipids is more efficient as compared to L_{α}^C , since the lipids are brought closer to the DNA strands in the former structure. But the bending of the lipid monolayer around the DNA in H_{II}^C phase, costs energy. The presence of DOPE in the complex however leads to a negative spontaneous curvature of the lipid-water interface and reduces this energy cost. Hence the addition of DOPE to DOTAP-DNA complexes induces a structural transformation from L_{α}^C to H_{II}^C .

Systematic studies similar to those discussed above on cationic lipid- DNA systems have not been carried out on complexes of single-chained cationic surfactants with DNA. This is despite the fact that the complexation with such a cationic surfactant CTAB, is often

used for RNA and DNA extraction from plants [17]. It is also being used for quick extraction of high quality DNA from lambda phages [18]. Various techniques have been used to study cationic surfactant-DNA complexes. But not many structural investigations have been carried out. Complex formation between short DNA fragments (200 bp) and dodecyltrimethylammonium bromide (DTAB) has been studied using dynamic light scattering (DLS), static light scattering (SLS), high performance capillary electrophoresis (HPCE) and DTAB-specific electrode [19]. Light scattering studies indicate that the diffusion coefficient of the complexes decrease in a non-linear manner as the degree of binding of surfactant ions (determined using a surfactant selective electrode) increases, and attains saturation at 0.8 molecules of surfactants per DNA phosphate group. Using HPCE, electrophoretic mobility of DNA has been measured as a function of free surfactant concentration. Comparison of the diffusion coefficient of complexes with their electrophoretic mobility suggests that the decrease in mobility is caused by an increase in the hydrodynamic friction, as more surfactant molecules are bound without changing the effective charge of DNA. Further increase in surfactant concentration leads to a significant decrease in mobility. This is due to the effective neutralization of the DNA. Hence the complex formation occurs in two stages. In the first stage, surfactant cations exchange with the counterions condensed on the surface of the DNA, without changing the effective charge on the DNA. More surfactant molecules bind in the second stage, causing a charge neutralization of the DNA and phase separation of the complex [19]. The effects of binding at surfactant concentrations below the critical micellar concentration has also been examined [20] using techniques like spectroscopy, fluorescence, isothermal titration calorimetry, high-resolution ultrasonic velocity and density measurements. It was found that the binding of surfactants results in a significant change in the DNA secondary structure. Fluorescence studies have also reported a discrete transition from an elongated coil to a collapsed globule of a single DNA (166 kbp) molecule in the presence of a cationic surfactant [21].

There have been some x-ray studies to probe the structure of single-tailed cationic

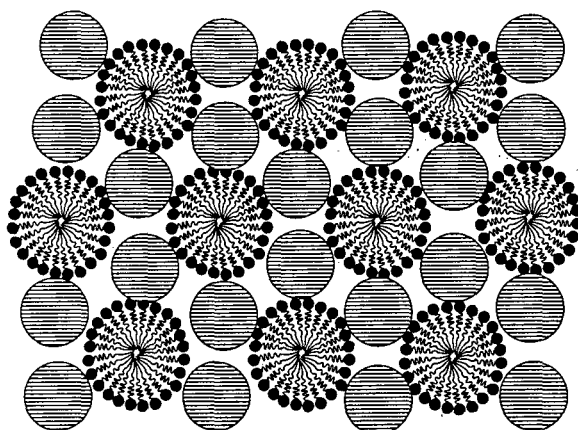


Figure 3.7: Schematic of the structure of the intercalated hexagonal phase, where each DNA strand is surrounded by three cylindrical micelles. The lattice parameter, $a = \sqrt{3} (R_m + R_{DNA})$, where R_m is the radius of the cylindrical micelle (~ 2.0 nm) and R_{DNA} that of the hydrated DNA strand (~ 1.25 nm)

surfactant–DNA complexes [22]. The surfactants used were DTAB, tetradecyltrimethylammonium bromide (TTAB), CTAB and octadecyltrimethylammonium bromide (OTAB). OTAB did not form complexes with DNA. The x-ray diffraction studies of DNA complexed with DTAB, show one peak at 3.6 nm. The TTAB–DNA complexes show peaks at 4 nm and 2.25 nm, which may be indexed as the (1 0) and (1 1) reflections of a 2D hexagonal lattice. Two peaks were also obtained for CTAB–DNA complexes at 4.4 nm and 2.54 nm which may again be indexed on a 2D hexagonal lattice. However in these studies, the peaks at 2.25 nm for the TTAB–DNA and 2.54 nm for CTAB–DNA complexes were wrongly attributed to the DNA–DNA separation within the complexes. Based on these observations, a structure was proposed for the complex, where the DNA strands are intercalated between the micellar aggregates, forming a 2D hexagonal lattice (fig.3.7). The model was proposed on the basis that the surfactants as well as DNA form a hexagonal phase at higher concentrations and not from any detailed analysis of the diffraction data. An inverted hexagonal phase as seen in DNA–lipid complexes cannot be ruled out from these studies. Hence we found it necessary to carry out further studies on these complexes to determine their structure unambiguously.

3.3 Structure of CTAB-DNA complex

CTAB solutions of appropriate concentrations were prepared in deionized water (Millipore). On adding DNA to the surfactant solution, the complex precipitates out. It was left to equilibrate in solution for about 4 days. The complex was then examined under a polarizing microscope and found to be birefringent. On heating, it was found to be stable up to 90°C. The precipitate along with some supernatant was transferred into a 1 mm diameter glass capillary for x-ray studies. The x-ray diffraction of the CTAB-DNA complex gives 3 peaks in the small angle region of the diffraction pattern (fig 3.8) with the magnitude of the scattering vectors q in the ratio 1 : $\sqrt{3}$: 2. We index them as the (1 0), (1 1) and (2 0) reflections from a 2D hexagonal lattice. The relative integrated intensities of the 3 reflections after geometric corrections, are in the ratio 1 : 0.07 ± 0.02 : 0.013 ± 0.003 . Relative intensities and the peak positions were found to be independent of the DNA concentration and of CTAB concentration up to 300 mM. Though x-ray diffraction determines the lattice of the complex, two possible structures can be proposed. One of them is an inverted hexagonal phase, where the DNA strands coated by a surfactant monolayer are arranged on a 2D hexagonal lattice (fig 3.2). A similar structure has been observed in lipid-DNA complexes [12]. The other is the intercalated phase (fig 3.7) consisting of DNA strands intercalated into the direct hexagonal phase of CTAB, where each DNA strand is surrounded by three cylindrical micelles [22].

The lattice parameter for the CTAB-DNA complex is 5.64 ± 0.09 nm. Taking the thickness of CTAB bilayer δ_s to be 3 nm and the radius of the hydrated DNA strand, R_{DNA} to be 1.25 nm, inverted phase would give a lattice parameter a ($=\delta_s + 2.R_{DNA}$) ~ 5.5 nm. If the radius of the cylindrical micelle R_m is 1.98 nm, the intercalated phase would have a lattice parameter a , given by $\sqrt{3}(R_m + R_{DNA}) \sim 5.6$ nm. Hence neither of the structures can be ruled out on the basis of the lattice parameter obtained for the complex. Intercalated phase would ensure that the complex is hydrophilic, whereas inverted phase would make it hydrophobic. Complexes of CTAB with short DNA are found to form stable dispersions which might lead

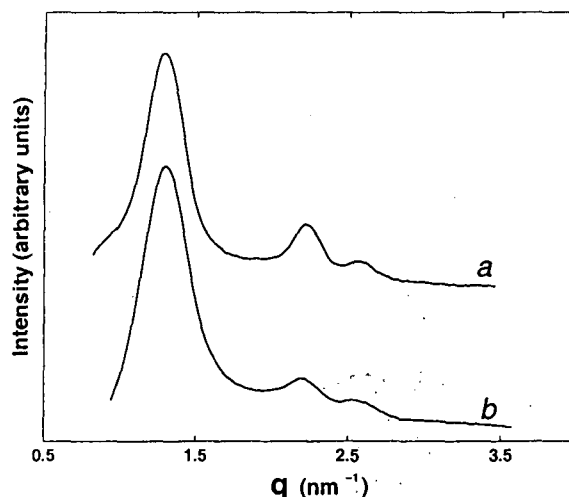


Figure 3.8: Diffraction patterns of the CTAB-DNA complex. ρ (=weight of CTAB/weight of polyelectrolyte) for the different curves are: 1.0 (a); 7.2 (b); CTAB concentration in the aqueous solution was 10 mM.

us to suspect that it forms an intercalated phase [23]. But this may not be conclusive of the structure. Only three reflections are obtained in the diffraction pattern of these systems with our experimental conditions, and hence the structure cannot be determined by calculating electron density maps. We have, therefore, used a modelling approach to determine the structure.

3.4 Modelling the structure of CTAB-DNA complex

To distinguish between the two distinct structures possible in CTAB-DNA complexes, as discussed above, we constructed models for the electron densities of each of these structures. The relative intensities calculated from the two models were then compared with the experimentally observed values.

The two dimensional electron density $\rho(\mathbf{r})$ of these two structures can be written as a convolution of a lattice function $\rho_L(\mathbf{r})$, which represents a 2D array of delta functions corresponding to the hexagonal lattice, with the electron density $\rho_b(\mathbf{r})$ as the repeating basis. [24].

Table 3.1: The parameters for the models obtained from the literature [25].

parameters	values
r_c	1.58 nm
ρ_c	0.28
ρ_w	0.332
r_h	0.4 nm
ρ_h	0.352

$$\rho(\mathbf{r}) = \rho_L(\mathbf{r}) \otimes \rho_b(\mathbf{r}) \quad (3.6)$$

where \mathbf{r} is a 2D vector.

The observed diffraction intensity $I(\mathbf{q})$, where \mathbf{q} is the scattering vector, is given by

$$I(\mathbf{q}) = A|F(\mathbf{q})|^2 = A|F_L(\mathbf{q})|^2|F_b(\mathbf{q})|^2 \quad (3.7)$$

where $F(\mathbf{q})$, $F_L(\mathbf{q})$ and $F_b(\mathbf{q})$ are the fourier transforms of $\rho(\mathbf{r})$, $\rho_L(\mathbf{r})$ and $\rho_b(\mathbf{r})$, respectively, and A is a constant independent of \mathbf{q} . In these models (fig 3.9), the DNA strand is represented as a circular disc of uniform electron density ρ_D . ρ_D has contributions from the water molecules and from the counterions present in the complex. The radius r_D of the disc is taken to be that of a DNA molecule with a hydration shell around it (= 1.25 nm). Each cylindrical micelle is represented as a cylindrical disc of uniform electron density ρ_c and radius r_c corresponding to the chain region, surrounded by an annular ring of electron density ρ_h and width r_h representing the head group of the micelle. The inverted micelle is modelled as an annular ring of electron density ρ_h and width r_h , surrounding the circular disc representing the DNA molecule. The values of electron density of water ρ_w , ρ_c , ρ_h , r_h and r_c taken from the literature [25] are given in table 3.1.

$\rho_b(\mathbf{r})$ for the intercalated phase is given as

$$\rho_b(r, \theta) = \rho_{DNA}(r) \otimes [\delta(\theta)\delta(r - b) + \delta(\theta - \pi)\delta(r - b)] + \rho_m(r) \quad (3.8)$$

where b is the separation between the DNA and the micellar cylinder and θ is the angle

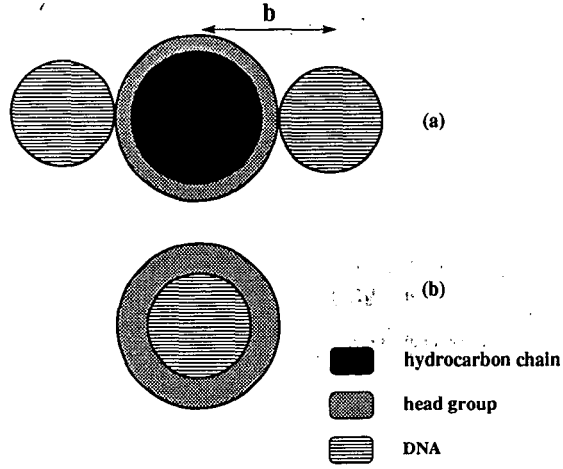


Figure 3.9: The repeating basis in the intercalated (a) and inverted (b) hexagonal phases.

made by b with the x -axis (fig 3.9). $\rho_m(r)$ and $\rho_{DNA}(r)$ are the electron densities of the cylindrical micelle and DNA strand respectively.

$$\begin{aligned}\rho_{DNA}(r) &= \rho_D - \rho_w, 0 < r < r_D \\ &= 0, r > r_D\end{aligned}$$

$$\begin{aligned}\rho_m(r) &= \rho_c - \rho_w, 0 < r < r_c \\ &= \rho_h - \rho_w, r_c < r < r_c + r_h \\ &= 0, r > r_c + r_h\end{aligned}$$

Fourier transforming $\rho_b(r, \theta)$, we get

$$F(q, \phi) = 4\pi \cos[qb(\cos\phi)] \rho_D r_D J_1(qr_D)/q + F_m(q) \quad (3.9)$$

where ϕ is the angle made by \mathbf{q} with the x -axis and $J_1(qr_D)$ is the Bessel function of order 1.

$F_m(q)$, the form factor of the micelle is given by

$$F_m(q) = 2\pi\rho_h[(r_h + r_c)J_1(q(r_h + r_c))/q - r_c J_1(qr_c)/q] \quad (3.10)$$

$\rho_b(\mathbf{r})$ of the inverted phase is,

$$\begin{aligned}\rho_b(r) &= \rho_D - \rho_c, 0 < r < r_D \\ &= \rho_h - \rho_c, r_D < r < r_h + r_D\end{aligned} \quad (3.11)$$

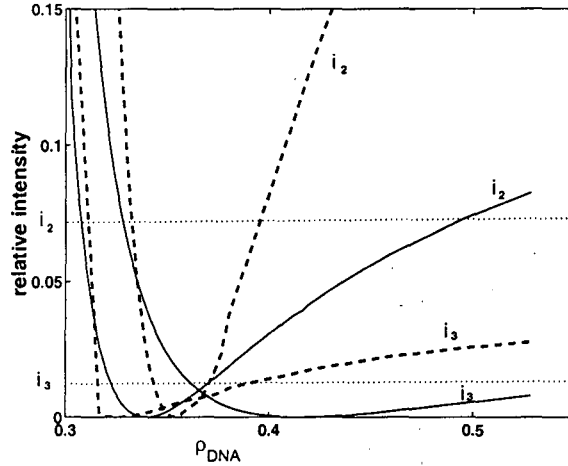


Figure 3.10: Variation of the relative intensities of the second and third Bragg peaks with ρ_{DNA} , obtained from the model for the intercalated (dashed lines) and inverted hexagonal phases (solid lines) of CTAB-DNA complex. The dotted lines indicate the experimental values of the relative intensities.

Fourier transforming $\rho_b(r)$, we get

$$F(q) = 2\pi\rho_D r_D J_1(qr_D)/q + 2\pi\rho_h[(r_D + r_h)J_1(q(r_D + r_h))/q - r_D J_1(qr_D)/q] \quad (3.12)$$

The relative intensities of the (1 0), (1 1) and (2 0) reflections of the hexagonal phase can be calculated using equation 3.7.

Due to the different contributions to ρ_D mentioned earlier, it could not be estimated. Therefore the relative intensities of the (1 1) and (2 0) reflections with respect to that of the (1 0) reflection denoted as i_2 and i_3 respectively were calculated from the two models for a reasonable range of values of ρ_D (fig 3.10). As seen from the figure, only in the case of the intercalated hexagonal phase the calculated and observed intensities match for a particular value of ρ_D , thus confirming the structure. Hence, we conclude from these studies that CTAB-DNA complexes form an intercalated phase. The formation of an intercalated phase suggests that the structure in the complex is determined by the morphology of the aggregates in the surfactant solution. To ascertain this we have tuned the spontaneous curvature of the surfactant aggregates in the complex using SHN.

3.5 Tuning the structure of CTAB-DNA complex with SHN

As discussed in section 3.3, SHN modifies the spontaneous curvature of CTAB micelles. For α ($= [\text{SHN}]/[\text{CTAB}]$) < 0.64 , the aggregates form worm-like micelles in dilute solution. At $\alpha \approx 0.64$, the aggregates transform from cylinders to bilayers [26, 27]. We have investigated the influence of SHN on the structure of the complex by varying α . At $\alpha = 0.2$, three peaks are observed in the small angle region which can be indexed on a hexagonal lattice (fig 3.11a).

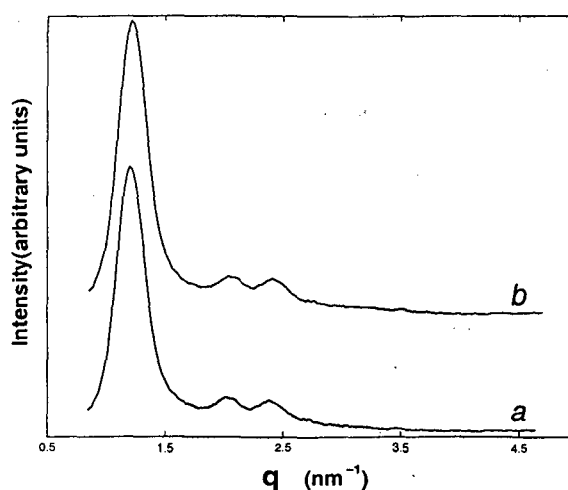


Figure 3.11: Diffraction patterns of the CTAB-SHN-DNA complexes. $\alpha = ([\text{SHN}]/[\text{CTAB}]) = 0.2$ and ρ ($=$ weight of CTAB/weight of polyelectrolyte) for the different curves are: 7.2 (a); 1.2 (b); $\rho_{iso} = 1.4$ at $\alpha = 0.2$. CTAB concentration in the aqueous solution was 10mM.

The peak positions remain independent of DNA concentration (fig 3.11b). Up to $\alpha = 0.55$, we find a similar behaviour in CTAB-SHN-DNA complexes, at different DNA concentrations (fig. 3.12). However, the lattice parameter a increases gradually with α from $a = 5.64 \pm 0.09$ nm at $\alpha = 0$ to $a = 6.06 \pm 0.09$ nm at $\alpha = 0.55$ in the hexagonal phase of the complex (fig. 3.13).

At $\alpha = 0.6$, x-ray diffraction gives two sharp peaks in the small angle region with their scattering vector q in the ratio 1: 2 (fig 3.14). In addition to this, a broad peak is observed at small angles (indicated by an arrow in the fig 3.14) whose position shifts to larger q values

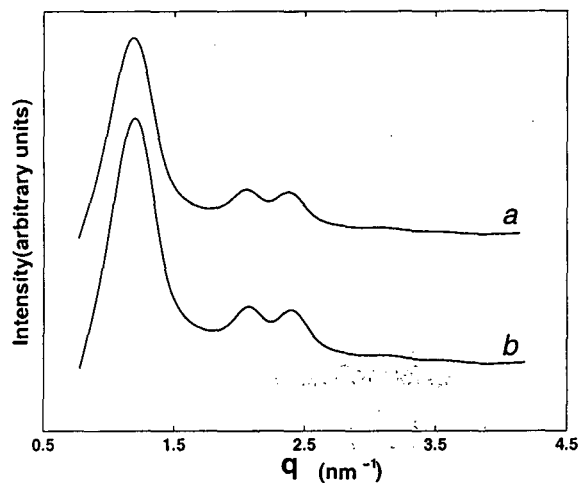


Figure 3.12: Diffraction patterns of the CTAB-SHN-DNA complexes. $\alpha = 0.55$. ρ for the different curves are: 14.4 (a); 1.2 (b); $\rho_{iso} = 1.72$ at $\alpha = 0.55$.

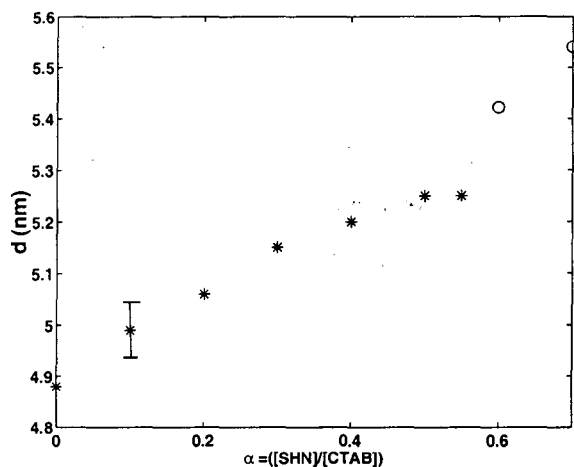


Figure 3.13: Variation of the lattice parameter with α . '*' denotes the hexagonal phase of the complex and 'o' denote the lamellar phase.

on increasing DNA concentration. The former set of peaks that remain independent of DNA content, correspond to a lamellar structure. The diffused peak is the DNA-DNA peak that has been observed earlier in lipid-DNA systems. Hence a hexagonal to lamellar transition of the complex occurs at around $\alpha = 0.6$. The lamellar periodicity at $\alpha = 0.6$ is 5.45 ± 0.09 nm. A sharp decrease in d_{DNA} is observed for $\rho < \rho_{iso}$ (fig 3.15). A similar structure is also observed at $\alpha = 0.7$ (fig 3.16). Here the lamellar periodicity increases by 0.1 nm. The dependence of d on α is given in fig 3.13. The various phases observed in the CTAB-SHN-DNA complexes and their corresponding lattice parameters at different SHN concentrations are given in table

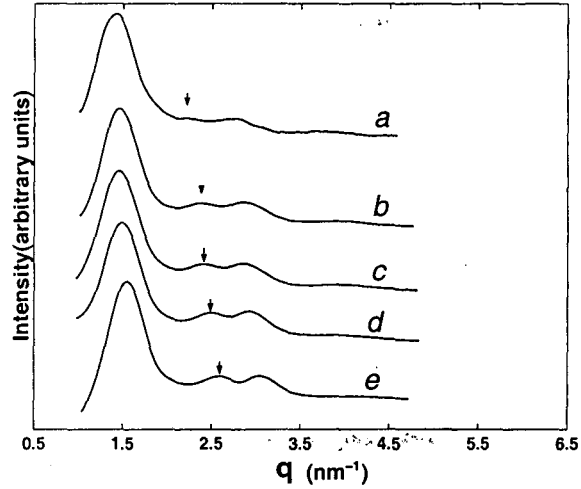


Figure 3.14: Diffraction patterns of the CTAB-SHN-DNA complexes. $\alpha = 0.6$. ρ for the different curves are: (a) 2.25; (b) 2.0; (c) 1.64; (d) 1.33; (e) 1.0; The arrow on the curves indicate in-plane DNA-DNA correlation peak. $\rho_{iso} = 2.8$ at $\alpha = 0.6$.

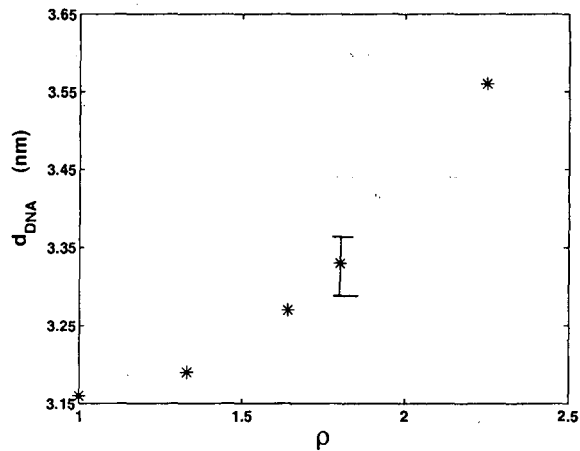


Figure 3.15: Variation of the DNA-DNA peak with ρ at $\alpha = 0.6$. $\rho_{iso} = 2.8$

3.2. No structural transformations are observed on heating up to 90 °C, although the lattice parameters are found to decrease with increasing temperature.

We have also studied the influence of NaCl on the structure of the complex. In the lamellar phase of the complex, corresponding to $\alpha = 0.6$ and $\rho = 1.3$, the separation between the bilayers increases from 5.45 nm to 5.85 nm in the presence of 0.5 M NaCl. Also a shift in the DNA-DNA peak from 3.19 nm to 3.56 nm is observed. This is similar to the behaviour seen in lipid-DNA complexes [10].

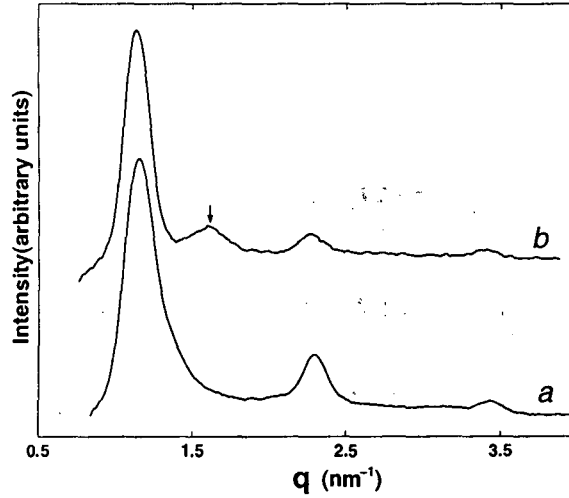


Figure 3.16: Diffraction patterns of the CTAB-SHN-DNA complexes. $\alpha = 0.7$. ρ for the different curves are: 14.4 (a); 3 (b). The arrow on curve b indicates in-plane DNA-DNA correlation peak, $\rho_{iso} = 3.74$ at $\alpha = 0.7$. CTAB concentration in the aqueous solution was 10mM.

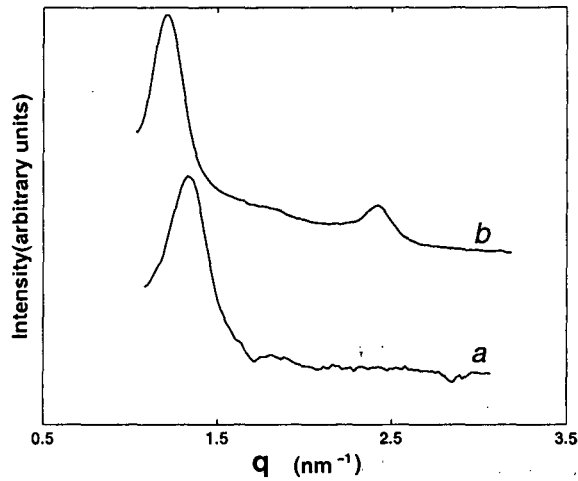


Figure 3.17: Diffraction patterns of the CTAB-ss DNA complexes. α and ρ for the different curves are: 0, 14.4 (a); 0.6, 14.4 (b); $\rho_{iso} = 1.12$ at $\alpha = 0$ and $\rho_{iso} = 2.8$ at $\alpha = 0.6$.

To study the influence of flexibility of the polyelectrolyte on the structure of CTAB-DNA complexes, the double stranded (ds) DNA was replaced by single stranded (ss) DNA. The persistence length of ss DNA (~ 1.5 nm) is an order of magnitude lower than that of ds DNA. CTAB-ss DNA complexes are found to form a hexagonal phase with a lattice parameter of 5.47 nm (fig 3.17a). At high SHN concentrations, ($\alpha = 0.6$), the complex exhibits a lamellar phase with a periodicity of 5.15 nm (fig 3.17b).

Table 3.2: The d-spacings and structures observed in CTAB-SHN-DNA complexes at different values of α . T is the temperature.

α	$d_1(nm)$	$d_2(nm)$	$d_3(nm)$	structure	T($^{\circ}C$)
0	4.88	2.82	2.44	H_I^C	30
0	4.7	-	-	H_I^C	90
0.1	4.99	2.88	2.50	H_I^C	30
0.2	5.06	2.92	2.53	H_I^C	30
0.3	5.15	-	2.575	H_I^C	30
0.4	5.2	-	2.6	H_I^C	30
0.5	5.2	-	2.6	H_I^C	30
0.55	5.25	3.03	2.63	H_I^C	30
0.6	5.42	2.71	-	L_{α}^C	30
0.6	5.09	-	-	L_{α}^C	75
0.7	5.54	2.77	1.85	L_{α}^C	30

3.6 Discussion

The hexagonal structure observed at low SHN concentrations, should be similar to that seen in CTAB-DNA complexes. However, by adding SHN to the CTAB solution, we decrease the spontaneous curvature of the cylinders. Hence the increase in the lattice parameters of the hexagonal phase on increasing α could be the consequence of an increase in the radius of the micellar cylinders.

The lamellar periodicity of 5.45 nm at $\alpha=0.6$ is consistent with the model of DNA strands sandwiched between the bilayers, with $d = \delta_m + 2R_{DNA}$, where δ_m (~ 3 nm) is the thickness of CTAB-SHN bilayer and R_{DNA} is the radius of a hydrated DNA strand ($= 1.25$ nm). Hence the lamellar phase obtained for the CTAB-SHN-DNA complex (fig. 3.18) is similar to the intercalated lamellar phase observed in lipid-DNA systems. In the lamellar phase of the complex, the separation between the DNA strands (d_{DNA}) depends on ρ , which is also consistent with the observations on lipid-DNA complexes [10]. The absence of DNA-DNA peaks in the lamellar complexes for $\rho > 2.25$ is probably because they fall within the first order lamellar

peak. This peak, however, appears as it shifts to higher q values for $\rho < 2.25$.

As discussed in section 3.2 in the context of DOTAP-DOPE-DNA complexes, electrostatics prefers H_{II}^C over L_α^C structure. The geometry of the H_{II}^C structure brings the surfactant ions closer to the negative charges on the DNA. Hence there is a gain in free energy due to the efficient neutralization that occurs in the H_{II}^C phase. But the free energy gain should compensate for the energy cost required to bend the surfactant monolayer around the DNA strand. If CTAB-DNA complexes formed an H_{II}^C structure, addition of SHN would reduce the energy cost required to have a negative spontaneous curvature at the micelle-water interface. Thus the presence of SHN should stabilize the inverted phase. We assume here that SHN does not substantially increase the rigidity of the bilayers. However, as discussed in section 3.4, a hexagonal to lamellar transition of the complex is observed close to where the cylinders transform to bilayers in the dilute surfactant solutions (ie at $\alpha = 0.6$). Hence these observations indicate that the structure of the complex is determined by the morphology of the aggregates in the surfactant solution. We also conclude from here that the CTAB-DNA complexes form an intercalated hexagonal phase consisting of DNA strands surrounded by cylindrical micelles (fig 3.7). The preference for this phase also indicates that the energy cost to disrupt the cylindrical micelles is much higher than the energy gain due to the greater proximity of surfactants to the DNA strand in the H_{II}^C structure. These results are consistent with the structure proposed from the analysis of diffraction data in section 3.3.

The complexes of CTAB with ss DNA also form a hexagonal phase similar to that of ds DNA. Since the persistence length of ss DNA differs from ds DNA, by an order of magnitude (refer table 1.1), the structure is expected to consist of cylindrical micelles bridged by the flexible DNA strands. In addition to the flexibility, the bare charge density of ss DNA is also different from that of ds DNA. Yet the structures obtained for the complexes are similar for the same SHN concentrations. The difference in the lattice parameters may arise due to the steric size of ds DNA that keeps the bilayers or cylinders from coming closer as compared

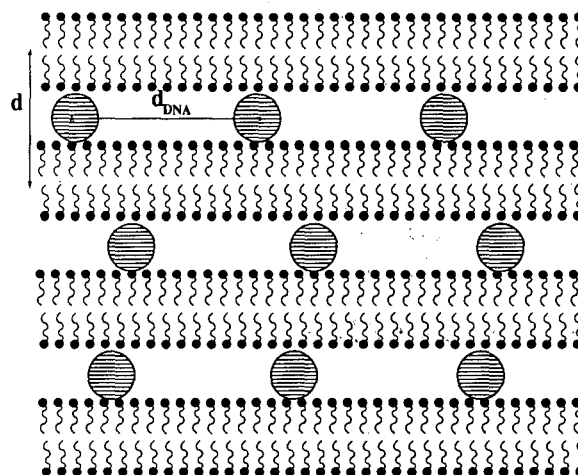


Figure 3.18: Schematic of the structure of the lamellar phase of DNA-surfactant complexes. The shaded circles represent the cross-section of the DNA strands.

to the ss DNA.

3.7 Conclusions

The complexes formed by ds and ss DNA with CTAB have a hexagonal structure. Analysis of the diffraction data indicates that the CTAB-ds DNA complex forms an intercalated hexagonal phase consisting of DNA strands surrounded by cylindrical micelles. We have further substantiated the structure by tuning the shape of the micellar aggregates using SHN. We find a continuous increase in the lattice parameter in the hexagonal phase of the complex and a hexagonal to lamellar transition at $\alpha \sim 0.6$, close to the cylinder to bilayer transition of the surfactant aggregates in dilute solutions. Both ds and ss DNA are found to exhibit a similar behaviour. We may conclude from here that the structure of the CTAB-DNA complexes is not significantly influenced by the flexibility or bare charge density of the polyelectrolyte, but is primarily determined by the morphology of the surfactant aggregates.

Bibliography

- [1] P. L. Felgner and G. Rhodes, *Nature* **349**, 351 (1991).
- [2] P. L. Felgner, *Proc. Natl. Acad. Sci. U.S.A.* **84**, 7413 (1987).
- [3] J. Gustafsson, G. Arvidson, G. Karisson, and M. Almgren, *Biochim. Biophys. Acta* **1235**, 305 (1995).
- [4] B. Sternberg, F. L. Sorgi, and L. Huang, *FEBS Lett.* **356**, 361 (1994).
- [5] J. O. Raedler, I. Koltover, T. Salditt, and C. R. Safinya, *Science* **275**, 810 (1997).
- [6] D. Lasic, H. Strey, C. A. Stuart, R. Podgornik, and P. M. Frederik, *J. Am. Chem. Soc.* **119**, 832 (1997).
- [7] T. Salditt, I. Koltover, J. O. Raedler, and C. R. Safinya, *Phys. Rev. E* **58**, 889 (1998).
- [8] F. Artzner, R. Zantl, G. Rapp, and J. O. Raedler, *Phys. Rev. Lett.* **81**, 5015 (1998).
- [9] L. Golubovic, T. C. Lubensky, and C. S. O'Hern, *Phys. Rev. E* **62**, 1069 (2000).
- [10] I. Koltover, T. Salditt, and C. R. Safinya, *Biophys. J.* **77**, 915 (1999).
- [11] R. Bruinsma, *Eur. Phys. J. B.* **4**, 75 (1998).
- [12] I. Koltover, T. Salditt, J. O. Raedler, and C. R. Safinya, *Science*, **281**, 78 (1998).
- [13] J. M. Seddon, *Biochim. Biophys. Acta*, **1031**, 1 (1989).
- [14] S. M. Gruner, *J. Phys. Chem.* **93**, 7562 (1989).

- [15] D. Harries, S. May, W. M. Gelbart, and A. Benshaul, *Biophys. J.*, **75**, 159 (1998).
- [16] S. May, D. Harries, and A. Benshaul, *Biophys. J* **78**, 1681 (2000).
- [17] N. Stein, G. Herren, and B. Keller, *Plant Breeding*. **120**, 354 (2001).
- [18] G. Manfioletti and C. Schneider, *Nucleic Acids Research* **16**, 2873 (1988).
- [19] A. V. Gorelov, E. D. Kudryashov, J. Jacquier, D. M. McLoughlin, and K. A. Dawson, *Physica A* **249**, 216 (1998).
- [20] S. Morrissey, E. D. Kudryashov, K. A. Dawson, V. A. Buckin, *Progr Colloid Polym Sci.* **112**, 71 (1999).
- [21] S. M. Mel'nikov, V. M. Sergeyev, K. Yoshikawa, H. Takahashi, and I. Hatta, *J. Chem. Phys.* **107**, 6917 (1997).
- [22] R. Ghirlando, E. J. Watchtel, T. Arad, and A. Minsky, *Biochemistry* **31**, 7110 (1992).
- [23] D. Langevin, Private Communication.
- [24] D. Sherwood, *Crystals, X – rays and Proteins*, Longman, 1976.
- [25] F. Reiss-Husson and V. Luzzati, *J. Phys. Chem.* **68**, 3504 (1964).
- [26] B. K. Mishra, S. D. Samant, P. Pradhan, S. B. Mishra, and C. Manohar *Langmuir*, **9**, 894 (1993).
- [27] K. Horbaschek, H. Hoffmann and C. Thunig, *J. Colloid Interface Sci.* **206**, 439 (1998).

Chapter 4

Influence of hexanol on the structure of CTAB-DNA and CTAB-SHN-DNA complexes

4.1 Introduction

This chapter deals with the structural transformations of CTAB-DNA complexes induced by the cosurfactant hexanol. Earlier work on lipid-DNA systems [1] has shown that hexanol can transform these complexes from a lamellar to a hexagonal structure, which has been attributed to the increased flexibility of the membranes in the presence of the cosurfactant. These experimental studies are described in section 4.2. The phase behaviour of a surfactant-water system is significantly altered by the addition of a cosurfactant and the phase diagram of the CTAB-hexanol-water system is also discussed in section 4.2. In section 4.3, we outline some theoretical calculations on the phase behaviour of lipid-DNA complexes as a function of the membrane flexibility, charge density and spontaneous curvature. In section 4.4, we present our results on CTAB-hexanol-DNA complexes. Novel structural transformations of these complexes are found driven by hexanol and DNA concentrations. We have also studied the influence of hexanol on the lamellar phase of CTAB-SHN-DNA complexes. Here again we find a transition from a lamellar to a hexagonal phase on increasing the hexanol concentration. These observations are dealt with in section 4.5. In section 4.6, we present some plausible explanations for the observed behaviour, based on the theories of phase behaviour of lipid-DNA complexes. Finally, section 4.7 deals with the conclusions

that may be drawn from the experiments discussed in this chapter.

4.2 Influence of a cosurfactant on the phase behaviour of surfactant-water systems

A cosurfactant is an amphiphile which does not form aggregates by itself in aqueous solutions. However when added to a surfactant solution, it modifies the properties of the surfactant aggregates such as their spontaneous curvature and flexibility. The effect of alcohols (ethanol to hexanol) on the micellar properties have been studied using conductivity, osmometry and light scattering techniques [2]. These studies indicate that long chain alcohols significantly affect the micellar properties. It is found that the addition of alcohols ranging from butanol to hexanol to a micellar solution results in a decrease of the critical micellar concentration (CMC) and of the molecular weight of the micelle, as well as an increase in the degree of ionization of the micelle. These are attributed to changes in surface charge density as well as in the dielectric constant near the head-group region.

The effect of long chain alcohols on surfactant systems has been studied in detail [3]. The morphology of the micelle is found to vary on adding hexanol and has been monitored through viscosity and light scattering measurements. Hexanol induces a sphere to rod transition of the micelles. This is a consequence of the decrease in spontaneous curvature of the headgroup-water interface in the presence of hexanol which leads to the elongation of micelles. These studies have also shown that the solution consists of long, flexible rod-like micelles that get entangled leading to a viscoelastic behaviour [4]. These are referred to as worm-like micelles in the literature.

The cetyltrimethylammonium bromide (CTAB)-water system exhibits an isotropic phase formed by spherical or rod-like micelles at low surfactant concentration (up to 25% by weight) [5]. On increasing the surfactant content, a hexagonal phase consisting of rod-like

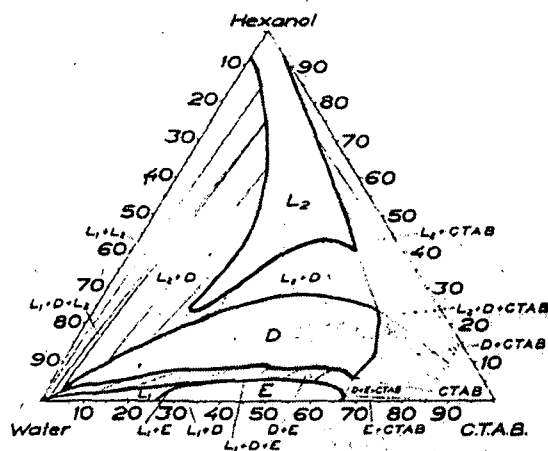


Figure 4.1: Phase diagram of CTAB-hexanol-water at 25°C. L_1 - isotropic, aqueous solution, L_2 - isotropic hexanol rich solution. D- lamellar phase, E- hexagonal phase [6].

micelles arranged on a 2D hexagonal lattice is obtained. The hexagonal phase persists over a large range of surfactant concentration. A lamellar phase finally appears at very high surfactant content (84-92% by weight). The addition of hexanol, however, alters the phase behaviour of CTAB-water system significantly.

The phase behaviour of CTAB-hexanol-water system (fig 4.1) has been probed in some detail using x-ray diffraction and polarizing microscopy [6]. An isotropic micellar solution is present at low surfactant and hexanol concentration (L_1). At higher surfactant concentrations (30- 70%) and low hexanol concentration (0 - 5%), a hexagonal phase (E) is observed. The incorporation of hexanol does not significantly alter the lattice parameter of the hexagonal phase, the diameter of the micellar cylinders and the thickness of the water layer up to 6% hexanol. At higher hexanol concentrations, a lamellar phase (D) is observed. The bilayer thickness is found to decrease from 3 nm to 2.5 nm on varying the ratio of hexanol to CTAB from 0.5 to 3.0. The lamellar phase exists up to 99% water dilution. This swelling behaviour is attributed to a steric repulsion arising from the thermal undulations of the bilayers, as discussed in chapter 2 [7]. The region L_2 observed at high hexanol concentrations, consists of a homogenous, isotropic phase rich in hexanol.

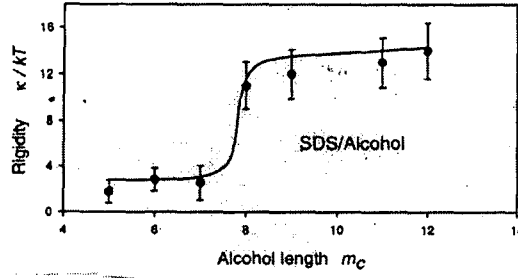


Figure 4.2: Bending rigidity of the bilayers in sodium dodecylsulphate-alcohol-water system as a function of alcohol chain length. Black circles are experimental data [8] and the solid line is calculated from theory [13].

The influence of alcohols on the bilayer bending rigidity (κ) has been studied using x-ray scattering techniques on sodium dodecylsulphate (SDS)-alcohol-water systems [8]. Due to the thermal undulations of the bilayers in the lamellar phase, the profile of the diffraction peak follows a power law behaviour given by

$$I(0, q_z) \sim |q_z - q_m|^{-2+\eta_m}$$

$$I(q_\perp, 0, q_m) \sim (q_\perp)^{-4+2\eta_m}$$

where q_\perp and q_z are components of the wave vector \mathbf{q} parallel and normal to the bilayers. $q_m = m q_0 = 2\pi m/d$, m being an integer and d the lamellar periodicity.

η_m is the exponent which describes the algebraic decay of layer correlations and is given by $\eta_m = m^2 q_0^2 k_B T / 8\pi (BK)^{\frac{1}{2}}$, where B is the compressibility modulus and K the bending rigidity modulus of the lamellar phase. $K = \kappa / d$, where κ is the bending rigidity of a single bilayer. B can be estimated from osmotic pressure measurements on the lamellar phase. Thus from the power law exponent η_m , κ has been calculated [9]. The plot κ as a function of the alcohol chain length is given in fig 4.2. For short chain alcohols (up to heptanol) $\kappa \approx 3 k_B T$, whereas for long chain alcohols (octanol to dodecanol) $\kappa \approx 13 k_B T$.

Elasticity theory predicts that $\kappa \propto \delta^3$, where δ is the thickness of the membrane [10]. In some of the earlier microscopic theories of the bilayer bending rigidity [11, 12], the dramatic lowering of κ observed on addition of short hydrocarbon chains to a bilayer composed of

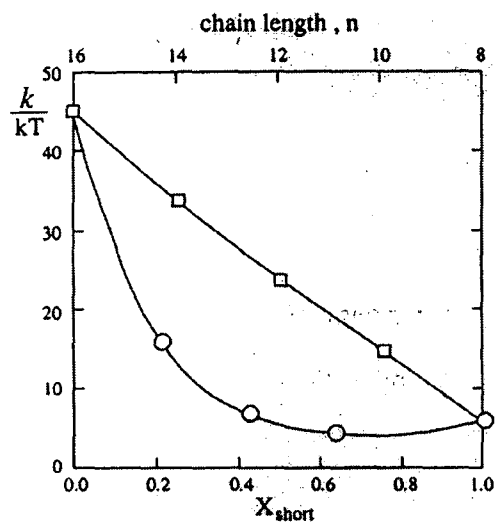


Figure 4.3: Bending elastic constants of a mixed bilayer consisting of long (C_{16}) and short (C_8) chains as a function of the short chain mole-fraction (circles, lower abscissa). Also shown (squares, upper abscissa) are the bending constants of a single component bilayer as a function of chain length. All data, for both the mixed and the pure bilayers are for chains packed with an average area per head-group of $A = 31.6 \text{ \AA}^2$. In these calculations the bending takes place at constant A [11].

long chains (fig 4.3) is qualitatively explained as follows: Closer to the hydrocarbon-water interface, the short and long chains have similar area per molecule. But beyond the region where the short chains terminate, the area per long chain increases and the bending in this region has negligible energy cost. Thus the short cosurfactant chains can be regarded as spacers between the long chains. Though these theories can explain the increase in κ with the chain length of the alcohol, they cannot account for the observed discontinuity in the bending rigidity with chain length. A more recent theory proposed by Foret and Wurger [13] is however able to quantitatively account for the measured rigidity as well as the discontinuous behaviour of bending modulus (fig 4.2).

4.3 Theoretical studies on the phase behaviour of cationic lipid-DNA complexes

The phase behaviour of solutions containing DNA, cationic and neutral lipids has been theoretically studied [14]. The different phases considered in this theory are intercalated lamellar structure of the lipid-DNA complex (L_{α}^C) consisting of DNA strands sandwiched between bilayers, the inverted hexagonal phase of the complex consisting of DNA covered by lipid monolayer (H_{II}^C), free bilayers in aqueous solution (L_{α}), uncomplexed, free DNA in solution (D) and inverted hexagonal phase (H_{II}). The free energies of the various phases have been calculated as a function of lipid composition and lipid/DNA ratio (ρ).

The free energy per lipid molecule is of the form

$$f_{\alpha} = f_{\alpha}^{es} + f_{\alpha}^{el} + f_{\alpha}^{mix} (\alpha = L_{\alpha}^C, H_{II}^C, L_{\alpha}, H_{II})$$

The three terms represent contributions from electrostatic charging, elastic curvature, and 2D mixing entropy of the lipid layers respectively. The total free energy, which is a weighted sum involving the different phases, is then minimized with respect to the relevant thermodynamic variables to obtain the phase diagram.

The major contribution in the electrostatic free energy is the entropy gain from the release of counter ions originally bound to the polyanion and the bilayers, into the solution on complex formation. This depends on the surface charge densities of the individual macroions, structure and composition of the condensed phases and salt concentration in solution. The electrostatic free energies of the various structures are calculated based on the nonlinear Poisson-Boltzmann (PB) equation.

If σ is the local surface charge density, Φ the corresponding electrostatic potential, V the volume of the electrolyte solution and n_0 the concentration of salt in the aqueous solution

and Ψ the reduced electrostatic potential given by $\Psi = e\Phi/k_B T$. The electrostatic free energy of a charged surface in solution is given by

$$F^{es} = \frac{1}{2} \int_S \sigma \Phi ds + k_B T n_0 \int_V [\Psi \sinh \Psi - 2 \cosh \Psi + 2] dv$$

where the first term involves contribution from all the charged surfaces S . Ψ is obtained by solving the Poisson-Boltzmann equation given by

$$\nabla^2 \Psi = \kappa'^2 \sinh \Psi$$

where the Debye screening length $\lambda_D = 1/\kappa'$.

The solution to the Poisson Boltzmann equation depends on the charged surface considered and boundary conditions specified for the system. In the L_α phase, the bilayer surfaces are treated as cationic, electrostatically decoupled surfaces for which $\Psi' = d\Psi/dz = 0$ at $z \rightarrow \infty$ and $\Psi' = -4\pi\phi_B l_B/a$ at the charged surface. l_B is the Bjerrum length and $\phi_B = N_B^+/N_B^0$, where N_B^+ and N_B^0 are the number of cationic and neutral lipids in the bilayer. If A is the cross-sectional area per lipid molecule, ϕ_B determines the surface charge density σ_B of the bilayer, given by $\sigma_B = e \phi_B/A$.

In this model the ds DNA is treated as a cylindrical rod of uniform negative charge. Hence in the H_{II}^C , H_{II} and D phases, the charged surfaces are cylindrically symmetric. If b is the separation between the charges on the DNA, then the uniform surface charge density of DNA, σ_D , may be given in terms of the radius of DNA R_D as $\sigma_D = -e / 2 \pi R_D b$. Thus for phase D, the boundary condition is given by $\Psi' = 0$ at $r = \infty$, and $\Psi'(R_D) = 2l_B/(R_D)b$ at the surface of the rod. For the H_{II} phase, the boundary conditions are $\Psi'(0) = 0$ and $\Psi'(R_I) = 4\pi\phi_I l_B/A_{hg}$, where R_I is the radius of curvature of the lipid head group water interface in the H_{II} phase and A_{hg} is the head group area of the lipid molecule in the inverted phase, and $\phi_I = N_I^+/N_I^0$ where N_I^+ and N_I^0 are the number of cationic and neutral lipids in the inverted hexagonal phase. For the H_{II}^C phase, the PB equation is solved for the aqueous region between two concentric, oppositely charged surfaces with $R_D \leq r \leq R_H$. R_H is the radius of curvature of the strongly curved lipid head group surface in the H_{II}^C phase.

$R_H = R_D + \delta_w$, where δ_w is the thickness of the water layer between the DNA and the lipid molecules. The boundary conditions are $\Psi'(R_D) = 2l_B/R_D b$ at the DNA surface and $\Psi'(R_H) = 4\pi\phi_H l_B/A_{hg}$ at the lipid surface, where A_{hg} is the head group area of the lipid molecule in the inverted phase and $\phi_H = N_H^+/N_H^0$, where N_H^+ and N_H^0 are the number of cationic and neutral lipids in the inverted hexagonal lipid-DNA complex.

The PB equation for the unit cell of the L_α^C phase is two dimensional and the boundary conditions here are more complex [15].

The elastic energy density of the lipid monolayers constituting the different lipid containing phases is given by

$$f^{el}(c, \phi) = A(\kappa/2)(c - c_o(\phi))^2 + f_v.$$

The first term represents the elastic deformation energy per molecule in a cylindrically bent lipid monolayer. Here, κ is the bending modulus, c_o the spontaneous curvature of the monolayer, c the actual curvature and A the area per molecule. ϕ denotes the lipid composition. In the inverted phase, some of the hydrophobic tails are more stretched in order to fill the interstitial regions between the cylinders. Since these molecules experience a different geometry from the rest, they are frustrated and experience average stretching cost per molecule given by f_v . For the phases L_α and L_α^C , f_v is zero.

The monolayers in the different phases are assumed to be ideal 2D mixtures. Hence their mixing free energy is given by

$$f^{mix}/k_B T = \phi \ln \phi + (1 - \phi) \ln(1 - \phi)$$

Adding the electrostatic, elastic, and mixing contributions, the total free energy of the mixture is minimized with respect to the relevant variables. It involves eleven concentration variables, of which three are eliminated due to the conservation condition that the total number of cationic lipid, neutral lipid and DNA molecules are fixed. Also since R_H and R_I are fixed in the inverted phases, it imposes a structural constraint that fixes the number of molecules that can be incorporated into the inverted phase. Thus f is a function of seven

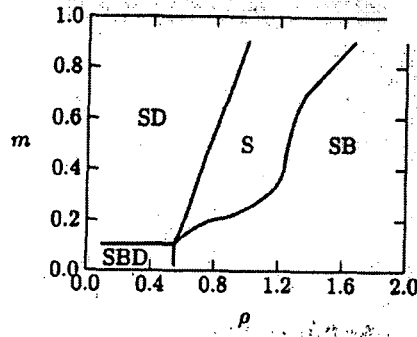


Figure 4.4: The phase diagram of a lipid-DNA mixture, for lipids that self-assemble into rigid planar membranes. The phase diagram was calculated for a membrane characterized by $\kappa = 10k_B T$ and $c_o = 0$. The symbols S, B, and D denote, respectively, the L_α^C , L_α and uncomplexed DNA phases [14].

independent variables. For every ρ , which is the ratio between the total number of cationic and DNA charges in the system, and m , the mole fraction of the cationic lipid in the original lipid mixture, the minimization of free energy with respect to these variables gives the number and identity of the coexisting phases and their composition.

For rigid planar membranes, no hexagonal phases appear in the calculated phase diagram (fig 4.4). At low values of ρ , lamellar complexes coexist with uncomplexed DNA. Here the DNA-DNA separation remains constant. Further increase of ρ leads to a one-phase region of lamellar complex alone where the DNA-DNA separation increases linearly with ρ , near the isoelectric point. At high values of ρ the complex coexists with excess bilayers.

For soft planar membranes, a more complex phase behaviour is obtained (fig 4.5). At small values of ρ , D coexists with either L_α^C or H_{II}^C depending on the value of m . At high ρ , all the DNA is complexed and coexists with excess bilayers. The lamellar phase of the complex, persists over a large range of ρ at high m , since the structure can tolerate changes in lipid composition by adjusting d_{DNA} . Due to the structural constraint imposed in the H_{II}^C phase, it exists only along a straight line in the phase diagram. At fixed ρ , the complex can undergo a transition from a lamellar to a hexagonal complex on decreasing the charge density which

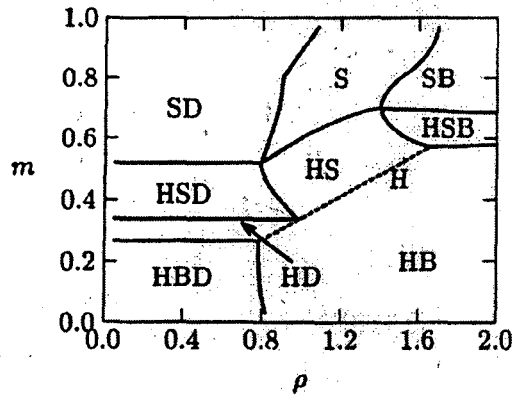


Figure 4.5: The Phase diagram of a lipid-DNA mixture, for lipids that self-assemble into very soft planar membranes. The phase diagram was calculated for membranes characterized by $\kappa=0$ and $f_v \equiv 0$. The symbols S,B,H and D denote respectively, the $L_\alpha^C, L_\alpha, H_{II}^C$ and uncomplexed DNA phases. The straight dashed line marks the single H_{II}^C phase region [14].

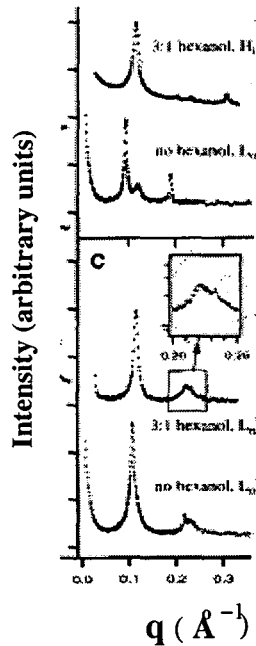


Figure 4.6: A series of SAXS scans of DOTAP-DOPC-hexanol-DNA complexes in excess water at different [hexanol]/[lipid] ratio [1].

has been observed experimentally [1]. A hexagonal to lamellar transition of the complex is also predicted for intermediate charge densities on decreasing ρ . Such transitions have not been reported in any of the earlier studies on lipid/surfactant-DNA complexes.

In the absence of DOPC, DNA-DOTAP-hexanol complexes exhibit a lamellar phase [1].

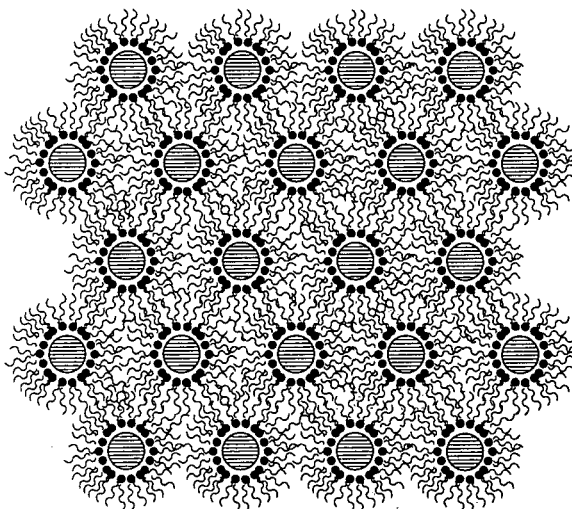


Figure 4.7: Schematic diagram of the inverted hexagonal phase (H_{II}^C) where the DNA are confined to the aqueous cores of the micelles.

The DNA-DNA separation was found to increase with hexanol concentration. Further, when $[DOPC]/[DOTAP] \sim 1$, the diffraction pattern indicates a 2D hexagonal lattice (fig 4.6) with the addition of hexanol. The lattice parameter of the hexagonal phase was found to be 6.25 nm. An inverted hexagonal structure consisting of DNA covered by a lipid monolayer, arranged on a 2D hexagonal lattice has been proposed in these systems (fig 4.7). As discussed above the addition of hexanol increases the flexibility of the bilayers. In addition, they also reduce the charge density. Therefore, these experimental observations are consistent with the $L_\alpha^C \rightarrow H_{II}^C$ transitions predicted for highly flexible bilayers with low charge density.

4.4 CTAB-DNA-hexanol Complexes

We have studied the influence of hexanol on the structure of CTAB-DNA complexes using small angle x-ray diffraction. The hexanol concentration β ($=[\text{hexanol}]/[\text{CTAB}]$) was varied from 1 to 10, keeping the concentration of CTAB fixed at 10 mM. All the complexes were found to be birefringent under a polarizing microscope, irrespective of the hexanol and DNA concentrations. The experimental results on CTAB-DNA-hexanol complexes may be summarized in the phase diagram (fig 4.8). This gives the structure of the complexes at

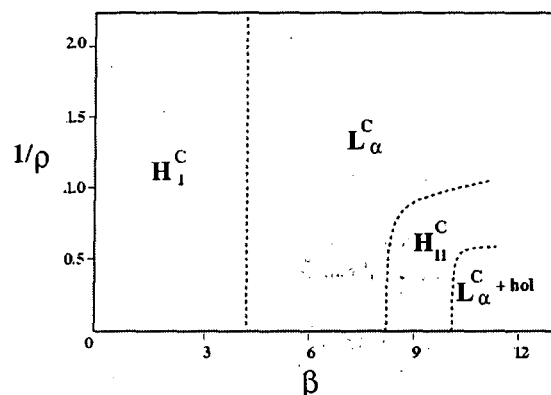


Figure 4.8: Partial phase diagram of the system showing the different structures obtained as a function of hexanol and DNA concentrations. $\beta = [\text{hexanol}]/[\text{CTAB}]$, $\rho = (\text{wt. of CTAB})/(\text{wt. of DNA})$. hol denotes the hexanol rich phase coexisting with the complex. The locations of the different phase boundaries have not been precisely determined.

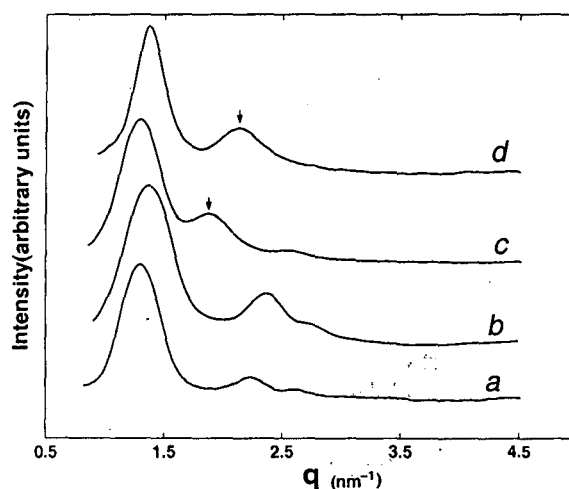


Figure 4.9: Diffraction patterns of the CTAB-hexanol-DNA complexes. β and ρ for the different curves are: 3.5, 36 (a) 3.5, 1 (b); 5, 36 (c); 5, 1 (d); $\rho_{iso} = 1.12$. CTAB concentration in the aqueous solution was 10 mM. The arrows on curves (c) and (d) indicate in-plane DNA-DNA correlation peak.

different hexanol and DNA concentrations. Note that β and ρ correspond to the total concentrations of hexanol and DNA in the solution and not in the complex alone. The boundaries between the different structures have not been determined very accurately.

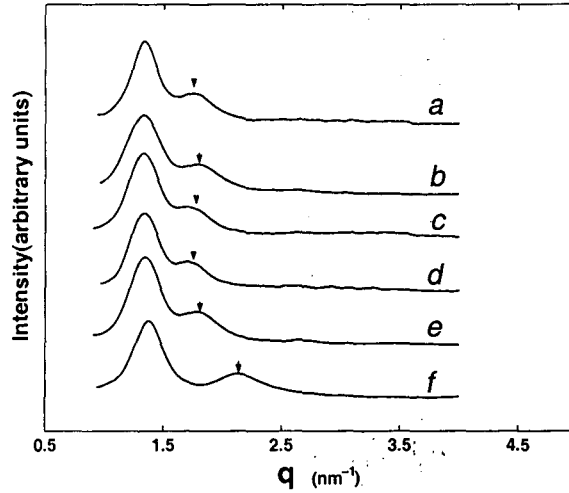


Figure 4.10: Diffraction patterns of the CTAB-hexanol-DNA complexes. $\beta=8$ and ρ for the different curves are: 36 (a); 7.2 (b); 1.8 (c); 1.2 (d); 1.01 (e); 0.9 (f); $\rho_{iso}=1.12$.

The x-ray diffraction data at low hexanol concentration (fig 4.9a,b) reveal three peaks in the small angle region, whose q values are in the ratio $1:\sqrt{3}:2$. Hence they could be indexed as the (1,0),(1,1) and (2,0) reflections of a 2-D hexagonal lattice. This phase was observed up to $\beta=3.5$. The lattice parameter of the hexagonal phase decreases from 5.64 nm at $\beta = 0$ to 5.50 nm at $\beta = 3.5$ for $\rho = 36$. At a higher DNA concentration, ($\rho=1$), the lattice parameter decreases to 5.23 nm from 5.5 nm at $\beta=3.5$.

At $\beta \sim 5$, diffraction pattern consists of two peaks in the small angle region corresponding to a lamellar structure (fig 4.9c,d). A diffuse peak whose position depends significantly on the DNA concentration near the isoelectric point is also observed indicated by an arrow in the diffraction patterns. Similar observations have been made in CTAB-SHN-DNA complexes (chapter 3) and cationic lipid-DNA complexes [16] where an intercalated lamellar structure has been proposed consisting of DNA strands sandwiched between the bilayers. The peak whose position depends on DNA concentration arises due to the correlation between the DNA strands in the plane of the bilayers and gives the average distance d_{DNA} between adjacent DNA strands. At $\rho > \rho_{iso}$, d_{DNA} increases from 3.32 nm at $\beta = 5$ to 3.65 nm at $\beta = 8$ (fig 4.10). The structure of the complex remains lamellar up to $\beta \sim 8.5$ (table 4.1).

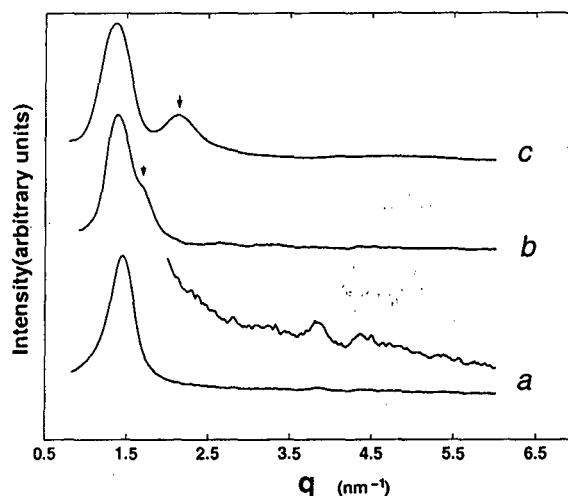


Figure 4.11: Diffraction patterns of the CTAB-hexanol-DNA complexes. $\beta = 9$ and ρ for the different curves are: 36 (a); 1 (b) 0.9 (c); $\rho_{iso}=1.12$. The peaks at $q=3.85$ and 4.4 nm^{-1} correspond to the (2,1) and (3,0) reflections from the 2-D hexagonal lattice.

At $\beta = 8.5$, another phase is observed at $\rho = 36$. The morphology of the complex changes at this hexanol concentration and it precipitates out of the aqueous solution. One strong peak and two weak reflections are observed in the diffraction pattern at $\beta \sim 9$ (fig 4.11a). The scattering vectors, q are in the ratio $1:\sqrt{7}:3$. These reflections can be indexed as the (1,0), (2,1) and (3,0) reflections from a 2D hexagonal lattice. On decreasing ρ , a transition to a lamellar phase is observed close to ρ_{iso} and the peak positions indicated by an arrow (fig 4.11b,c) shift from 3.6 nm to ~ 2.7 nm.

At $\beta = 10$, the surfactant solution phase separates to form surfactant rich and hexanol rich phases. On adding DNA to the CTAB-hexanol solution at $\beta = 10$, the complex obtained coexists with a hexanol rich phase. X-ray diffraction indicates a lamellar structure for the complex at $\rho = 36$ (fig 4.12a). A DNA-DNA peak is observed at 3.7 nm which is similar to that observed at lower values of β . However, further decrease in ρ leads to the gradual disappearance of the hexanol rich phase (hol) and at $\rho = 1$, a hexagonal phase is observed (fig 4.12b). On increasing DNA concentration much beyond the isoelectric point a lamellar structure reappears (fig 4.12c) with a d_{DNA} of 2.96 nm. This transition occurs in a narrow range of $1 > \rho > 0.5$. Such transformations of the structure, driven by DNA concentration

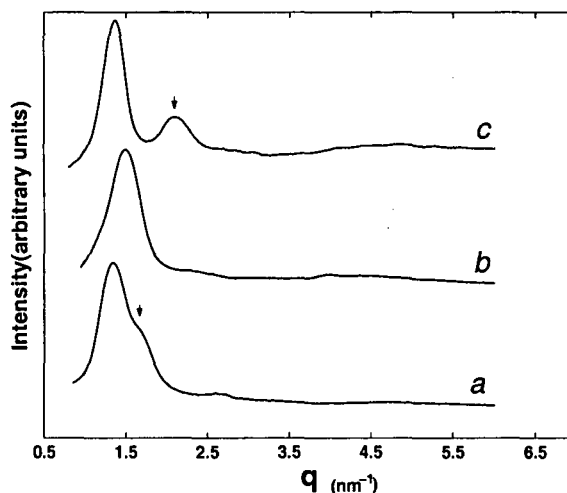


Figure 4.12: Diffraction patterns of the CTAB-hexanol-DNA complexes. β and ρ for the different curves are: 10, 36 (a); 10, 1 (b); 10, 0.5 (c); $\rho_{iso}=1.12$.

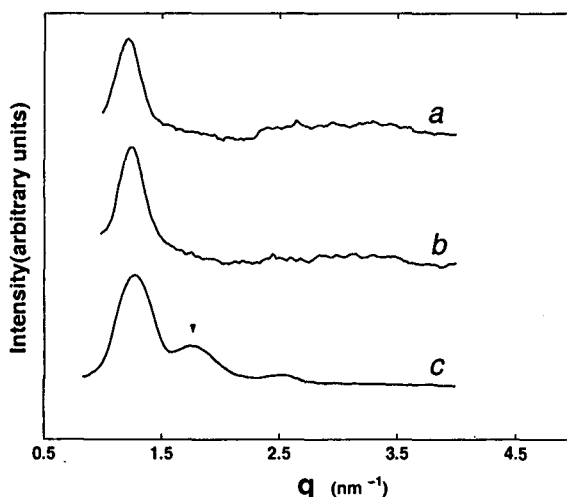


Figure 4.13: Diffraction patterns of the CTAB-SHN-hexanol-DNA complexes. $\alpha = 0.7$; β and ρ for the different curves are: 3, 36 (a); 4, 36 (b) 5, 36 (c); $\rho_{iso}=3.74$.

have not been reported in the literature.

4.5 CTAB-SHN-hexanol-DNA Complexes

As discussed in chapter 3, CTAB-SHN-DNA complexes have a lamellar phase at $[\text{SHN}]/[\text{CTAB}] \sim 0.6$. We have studied the influence of hexanol on these complexes. The diffraction pattern of CTAB-SHN-hexanol-DNA complexes reveal three peaks in the small angle region with the scattering vectors in the ratio, 1:2:3 (fig 4.13). Hence up to $\beta \sim 5$,

Table 4.1: The d-spacings, structure and lattice parameters of CTAB-hexanol-DNA complexes at different values of α and ρ . a and d denote the lattice parameters of the hexagonal and lamellar phases respectively. $\rho_{iso} = 1.12$.

β	ρ	$d_1(nm)$	$d_2(nm)$	$d_3(nm)$	$d_{DNA}(nm)$	phase	$a, d(nm)$
0	36	4.88	2.82	2.44	-	H_l^C	5.64
0	1	4.88	2.82	2.44	-	H_l^C	5.64
3.5	36	4.76	2.79	2.38	-	H_l^C	5.50
3.5	1	4.53	2.64	2.27	-	H_l^C	5.23
5	36	4.87	2.43	-	3.32	L_α^C	4.87
5	1	4.65	-	-	3.23	L_α^C	4.65
6	36	4.76	-	-	-	L_α^C	4.76
8	36	4.7	-	-	3.65	L_α^C	4.70
8	7.2	4.70	-	-	3.52	L_α^C	4.70
8	3.6	4.76	-	-	3.61	L_α^C	4.76
8	1.8	4.70	-	-	3.61	L_α^C	4.70
8	1.2	4.7	-	-	3.61	L_α^C	4.70
8	1.03	4.7	-	-	3.52	L_α^C	4.70
8	0.9	4.59	-	-	2.93	L_α^C	4.59
8.5	36	4.35	1.64			H_{li}^C	5.01
8.5	0.85	4.61			3.01	L_α^C	4.61
9	36	4.34	1.62	-	-	H_{li}^C	5.01
9	7.2	4.36	1.64	-	-	H_{li}^C	5.03
9	1	4.49	-	-	-		
9	0.9	4.59	-	-	2.96	L_α^C	4.59
10	36	4.60	2.30	-	3.7	L_α^C	4.60
10	1	4.17	1.58	-	-	H_{li}^C	4.82
10	0.47	4.5			2.97	L_α^C	4.5

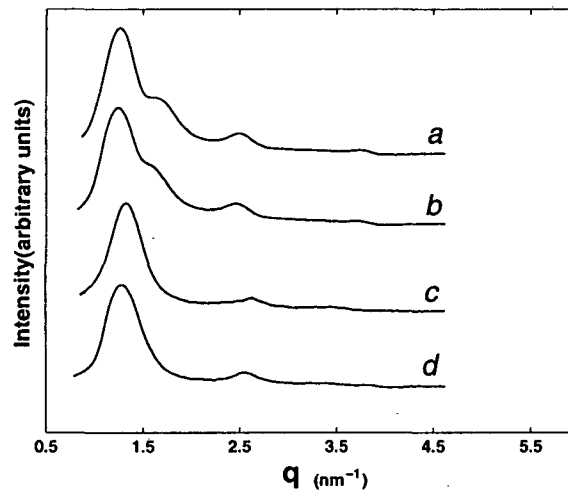


Figure 4.14: Diffraction patterns of the CTAB-SHN-hexanol-DNA complexes. $\alpha = 0.7$; β and ρ for the different curves are: 6, 36 (a); 7, 36 (b); 8, 36 (c); 9, 36 (d); $\rho_{iso} = 3.74$.

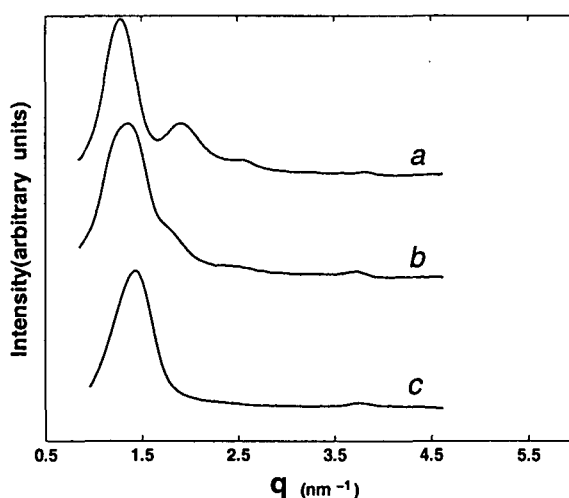


Figure 4.15: Diffraction patterns of the CTAB-SHN-hexanol-DNA complexes. $\alpha = 0.7$; β and ρ for the different curves are: 10, 36 (a); 10, 1 (b) 12, 0.5 (c); $\rho_{iso}=3.74$.

the structure of the complex remains lamellar. Also, the lattice parameter decreases with increase in hexanol concentration (table 4.2). Phase separation occurs in the CTAB-SHN-hexanol solution at $\beta \sim 6$ with the appearance of a hexanol rich phase. At $\beta = 6$, the complex coexists with a hexanol-rich phase. However the complex remains lamellar up to $\beta = 9$ (fig 4.14). At $\beta = 10$, the complex shows a lamellar phase at low DNA concentrations (fig 4.15 a, b).

At $\beta \sim 10$, the morphology of the complex changes at high DNA concentration. It no longer remains dispersed in the aqueous solution but precipitates out of it. Further the hexanol rich phase disappears. Similar behaviour was also observed at $\beta \sim 12$. One strong reflection and a weak reflection were observed in the diffraction pattern of this complex (fig 4.15c), with the scattering vectors in the ratio, $1:\sqrt{7}$. These could be indexed as the (1,0) and (2,1) peaks of a 2D hexagonal lattice. The d-spacings, lattice parameters and structures of the complexes at various SHN, hexanol and DNA concentrations are given below (table 4.2).

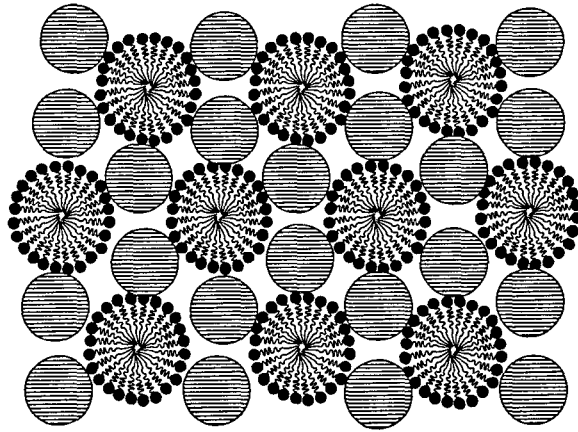


Figure 4.16: The intercalated hexagonal phase (H_I^C), where each DNA strand is surrounded by three cylindrical micelles.

surfactant solution, ρ_1 and ρ_2 the density of CTAB and hexanol, then $\rho_s = \phi_1\rho_1 + \phi_2\rho_2$

The average area of DNA, A_D [= molar volume/(N_A · contour length)] $\sim 1.86 \text{ nm}^2$. The density of DNA ρ_D is 1.7 g/cc and the weight fraction of CTAB in the micelle f is 0.51 at $\beta = 3.5$. This gives $\rho_s = 0.9$.

In the absence of hexanol $\rho_c = 3.98$. Since $\rho_{iso}=1.1$, this implies that these complexes are overcharged with excess CTAB. This is a consequence of the much smaller area of the CTAB head group compared to the effective area per charge of the DNA. The system would, therefore, tend to incorporate more DNA in the complex in order to achieve better neutralization. However, this can only be done by making the CTAB micelles thinner. The observation that the lattice parameter of these complexes do not change with DNA concentration indicates that such deformations are prevented by the rigidity of these micelles.

$\rho_c = 1.67$ at $\beta = 3.5$, which is still larger than ρ_{iso} . Interestingly, in this case the lattice parameter is found to decrease with DNA concentration for $\rho < 1.67$, indicating uptake of more DNA by thinning the cylindrical micelles. The incorporation of hexanol in the micelles seems to make them more flexible and susceptible to such deformations.

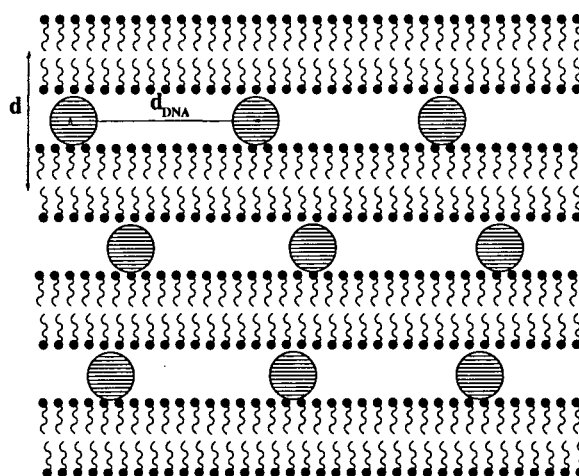


Figure 4.17: Schematic diagram of lamellar phase (L_{α}^C) of DNA-surfactant complexes, where the DNA strands (denoted by shaded circles) are sandwiched between surfactant bilayers.

The diffraction pattern of the lamellar phase observed at $\beta = 5$, indicates that the structure is similar to the intercalated lamellar phase (L_{α}^C), discussed in chapter 3 (fig 4.17) [16]. The lattice parameter of 4.9 nm observed at $\rho = 36$, is consistent with a CTAB-hexanol bilayer of thickness 2.4 nm and a hydrated DNA of diameter 2.5 nm. The decrease in the lamellar periodicity to ~ 4.7 nm, at $\beta = 8$, indicates that the addition of hexanol leads to the thinning of bilayers. The increase in DNA-DNA separation by nearly 3 nm on varying β from 5 to 8 at low DNA concentrations ($\rho = 36$), is probably a consequence of a decrease in the charge density of the bilayers when it incorporates more hexanol. As discussed in section 3.2, addition of hexanol to CTAB-water system leads to a transition from a hexagonal to a lamellar phase. The transition from H_I^C to L_{α}^C on increasing the hexanol concentration is thus consistent with the phase behaviour of the surfactant-water system. The sharp decrease in d_{DNA} , near ρ_{iso} observed at $\beta \sim 8$ is similar to the behaviour observed in lipid-DNA complexes. Here below ρ_{iso} , the complex get overcharged with excess DNA due to the higher free energy of the uncomplexed DNA in solution [17].

The diffraction pattern (fig 4.11a) and the morphology of the complex indicates that the

hexagonal phase observed at $\beta = 8.5$, is different from that observed at lower values of β . An inverted hexagonal phase can be proposed for the complex. The lattice parameter of 5.05 nm is consistent with a CTAB-hexanol bilayer of thickness ~ 2.5 nm and the diameter of a hydrated DNA ~ 2.5 nm. A similar structure has been observed in lipid-DNA complexes in the presence of hexanol [1], where DNA strands are confined to the aqueous cores of inverted cylindrical micelles (fig 4.7). This (H_{II}^C) structure is consistent with the hydrophobic nature of the complex and is further supported by a simple analysis of the diffraction data. The absence of the (1 1) and (2 0) reflections in the diffraction patterns of the complex indicates that the form factor of the electron rich cylindrical core has a zero in between the corresponding values of q . Taking the electron density of the core to be uniform, this condition gives the radius of the core to be about 1.3 nm, which is very close to that of a hydrated DNA (~ 1.25 nm).

The occurrence of the $L_{\alpha}^C \rightarrow H_{II}^C$ transition on increasing the hexanol concentration may be qualitatively understood as follows. In the inverted phase, the neutralization of the base pairs by the surfactant counter ions is more efficient due to their enhanced proximity in this geometry. Hence formation of an inverted phase results in a gain in the electrostatic contribution to the free energy. However the accompanying energy cost for bending the bilayer around the DNA is given by $\frac{1}{2}\kappa (C - C_o)^2$. C is the curvature of the DNA cylinder and C_o the spontaneous curvature of the surfactant-water interface. The presence of hexanol is known to lower κ and hence decreases the energy cost for bending the bilayers [8]. It has been shown from theoretical computations that H_{II}^C phase is preferred over the L_{α}^C phase in lipids with very flexible bilayers at low charge density [14]. The presence of hexanol decreases the charge density of the bilayers as well as increases their flexibility and hence satisfies both these conditions. Further, as hexanol is not confined to the lipid-water interface, it can occupy the interstitial regions in the H_{II}^C structure where the three inverted cylindrical micelles meet. This reduces the frustration of the chains of the amphiphile that would have had to stretch in order to occupy these regions. Thus the presence of hexanol further stabilizes the

H_{II}^C phase.

The diffraction pattern as well as the morphology of the complexes obtained at higher DNA concentration when $\beta = 9$ indicates that they form an intercalated lamellar structure. The reason for the transition from H_{II}^C to L_α^C structure on increasing DNA concentration observed here, is most likely the denser packing of DNA in the lamellar phase. The distance between two adjacent DNA is fixed at the lattice parameter a , in the inverted phase. On the other hand, no such restriction exists in the L_α^C structure, and d_{DNA} can change significantly across the isoelectric point. The amount of DNA which can be incorporated into lamellar phase as compared to the inverted hexagonal phase, can be estimated from the geometry of the two structures. For the inverted hexagonal phase, it is given by

$$\rho_c^H = \rho_s^1 A_s^1 f^1 / \rho_D A_D.$$

where the superscript 1 denotes the H_{II}^C structure.

Similarly for the lamellar complex it is given by

$$\rho_c^L = \rho_s^2 A_s^2 f^2 / \rho_D A_D.$$

where the superscript 2 denotes the L_α^C structure.

If we consider the two structures at similar surfactant composition,

$$\rho_s^1 f^1 = \rho_s^2 f^2,$$

$$\rho_c^H / \rho_c^L = A_s^1 / A_s^2$$

Since $A_s^1 = (\sqrt{3}a^2 - 2\pi R_D^2)/2$ and A_s^2 , estimated from the bilayer thickness δ and the separation between the DNA strands d_{DNA} , is given by $A_s^2 = d_{DNA} \delta$.

The ratio, $\rho_c^H / \rho_c^L = (\sqrt{3}a^2 - 2\pi R_D^2)/(2\delta d_{DNA})$. Putting $a = 5.0$ nm, $R_D = 1.25$ nm, and $\delta = 2.2$ nm, this ratio turns out to be $7.5/d_{DNA}$. Hence the lamellar complex can accommodate more DNA than the H_{II}^C structure as long as $d_{DNA} < 7.5$ nm. In the lamellar complexes obtained for low hexanol concentrations, d_{DNA} is 3.5 nm even at low hexanol concentrations.

Thus it is clear that more DNA can be accommodated in the L_α^C phase as compared to H_{II}^C .

Though at low DNA concentrations, the H_{II}^C phase is stabilized by the efficient neutralization of DNA, it becomes unstable in the presence of excess uncomplexed DNA and transforms to L_α^C . The fact that the $H_{II}^C \rightarrow L_\alpha^C$ transition is observed at a value of ρ slightly greater than ρ_{iso} supports the proposed mechanism. Such transformations of the structure of the complexes, driven by DNA concentrations have not been reported in the literature.

The DNA concentration at the H_{II}^C to L_α^C transition should correspond to the maximum amount of DNA that can be incorporated in the former structure. As discussed earlier, it can be estimated from the geometry of the system and is given by $\rho_c = (\sqrt{3}a^2 - 2\pi R^2)\rho_s f / (2A_D \rho_D)$. At $\beta = 9$, ρ_c is found to be 1.3. This is close to the experimental value of ~ 1.0 , thus once again confirming the above mechanism.

The formation of a lamellar complex at $\beta = 10$ for high ρ with d_{DNA} comparable to the values at lower β and high ρ , indicates that the hexanol concentration in the surfactant-rich phase is less than that in the solution just before phase separation. The gradual disappearance of the hexanol rich phase on increasing the DNA concentration indicates that hexanol content in the complex increases. This leads to an increase in the flexibility and a decrease in charge density of the bilayer and the structure transforms to H_{II}^C . The $H_{II}^C \rightarrow L_\alpha^C$ transition at higher DNA concentration as before is driven by the denser packing of DNA in the latter phase. The observed d_{DNA} of 2.9 nm is consistent with this. The narrow range of $0.5 < \rho < 1$ over which the transition occurs agrees with the estimated $\rho_c \sim 1.0$.

Similar phase transitions have been theoretically predicted for soft bilayers ($\kappa = 0$) at intermediate charge densities [14]. Here the charge density of the bilayers are varied using a mixture of the cationic and neutral lipids. Since both the lipids remain near the lipid-water interface, from the lipid composition and the head group area of the lipids, the charge density

of the bilayers at each composition can be estimated. Such an estimation cannot be made in our system since the hexanol does not remain confined at the surfactant-water interface. Hence the phase diagram obtained for the CTAB-hexanol-DNA complexes cannot be quantitatively compared with the calculated phase diagrams of lipid-DNA complexes. However our experimental observations qualitatively agree with the theoretical prediction of $H_{II}^C \rightarrow L_{\alpha}^C$ transition in flexible bilayers at low charge densities on increasing the DNA concentration.

In the CTAB-SHN-hexanol-DNA complexes, the structure remains lamellar for all hexanol concentrations, at high values of ρ . The decrease in the lattice parameters on increasing β , observed before the phase separation occurs in the surfactant solution, is consistent with the thinning of bilayers in the presence of hexanol. Similar to the lipid-DNA complexes, a transition from $L_{\alpha}^C \rightarrow H_{II}^C$ is also observed in these complexes at high ρ . The absence of (1,1) and (2,0) reflections and the presence of a weak (2,1) reflection confirms the inverted phase. Though a detailed study of the system has not been carried out, the phase behaviour of this system can be expected to be similar to that of CTAB-hexanol-DNA complexes, except for the occurrence of the intercalated hexagonal structure at low hexanol concentrations in the latter system.

4.7 Conclusion

We have studied the influence of hexanol on the structure of complexes of CTAB formed with ds DNA. At low DNA concentrations, the complexes exhibit a $H_I^C \rightarrow L_{\alpha}^C \rightarrow H_{II}^C$ transition on varying the hexanol concentration. These transitions are in accordance with the known influence of hexanol on the structure and properties of CTAB aggregates. A novel $H_{II}^C \rightarrow L_{\alpha}^C$ transformation is observed as a function of DNA concentration at high hexanol content, which may be understood in terms of the more efficient packing of DNA in the L_{α}^C

structure. A partial phase diagram of this system has been constructed, which shows the different structures exhibited by these complexes. We have also studied the influence of hexanol on the structure of CTAB-SHN-DNA complexes. The phase behaviour of the system is found to be similar to the CTAB-DNA complexes, but for the occurrence of the intercalated hexagonal phase at low hexanol concentration in the former system.

Bibliography

- [1] I. Koltover, T. Salditt, J. O. Raedler, and C. R. Safinya, *Science*, **281**, 78 (1998).
- [2] R. Zana, S. Yiv, C. Strazielle, and P. Lianos, *J. Colloid Interface Sci* **80**, 208 (1981).
- [3] R. Gomati, J. Appell, P. Bassereau, J. Marignan, and G. Porte, *J. Phys. Chem.*, **91**, 6203 (1987).
- [4] J. Appell, G. Porte, and Y. Poggi, *J. Colloid Interface Sci* **87**, 492 (1982).
- [5] F. Husson, H. Mustachchi, and V. Luzzati, *Acta Cryst.* **13**, 668 (1960).
- [6] P. Ekwall, L. Mandell, and K. Fontell, *J. Colloid Interface Sci* **29**, 639 (1969).
- [7] W. Helfrich, *Z. Naturforsch.*, **33a**, 305 (1978).
- [8] C. R. Safinya, E. B. Sirota, D. Roux, and G. S. Smith, *Phys. Rev. Lett.*, **62**, 1134 (1989).
- [9] D. Roux and C. R. Safinya, *J. Phys. France* **49**, 307 (1998)
- [10] L. D. Landau and E. M. Lifschitz, *Theory of Elasticity* (Pergamon, New York, 1970).
- [11] I. Szleifer, D. Kramer, A. Ben-Shaul, D. Roux, and W. M. Gelbart, *Phys. Rev. Lett.*, **60**, 1966 (1988).
- [12] I. Szleifer, D. Kramer, A. Ben-shaul, W. M. Gelbart, and S.A. Safran, *J. Chem. Phys.*, **92**, 6800 (1990).
- [13] L. Foret and A. Wurger, *Phys. Rev. Lett.*, **86**, 5930 (2001)
- [14] S. May, D. Harries, and A. Benshaul, *Biophys. J.*, **75**, 159 (1998).

- [15] D.Harries, S.May, W.M.Gelbart, and A.Benshaul, *Biophys. J.* **75**, 159 (1998).
- [16] J. O. Raedler, I. Koltover, T. Salditt, and C. R. Safinya, *Science* **275**, 810 (1997).
- [17] I.Koltover, T.Salditt, and C.R.Safinya, *Biophys. J.*, **77**, 915 (1999).

Chapter 5

Structure of cationic-surfactant – polyelectrolyte complexes

5.1 Introduction

This chapter deals with the structures exhibited by surfactant-polyelectrolyte complexes in aqueous solutions. Earlier work on the structure and phase behaviour of similar complexes is described in section 5.2. Our experimental results from optical microscopy and x-ray diffraction studies on complexes of cetyltrimethylammonium bromide (CTAB) with a variety of polyelectrolytes listed in table 5.1 are discussed in section 5.3. All complexes form a hexagonal phase, though with different lattice parameters depending on the polyelectrolyte used. There has not been any systematic study of the influence of the micellar shape on the structure of these complexes. Hence as in the case of CTAB-DNA complexes, discussed in chapter 3, we have tuned the micellar shape using sodium-3-hydroxy-2-naphthoate (SHN). Section 5.4 deals with the structural changes of complexes of CTAB-SHN with different polyelectrolytes on varying the SHN concentration. A transition from a hexagonal to a centered rectangular structure is observed in CTAB-SHN-PAA and CTAB-SHN-PGA complexes on increasing α ($= [\text{SHN}]/[\text{CTAB}]$). CTAB-SHN-PSS complexes show a transition from a hexagonal to a primitive rectangular structure as α is increased. They also show yet another structure at higher α , which has not yet been identified. Complexes of PVS with CTAB-SHN exhibit a hexagonal \rightarrow centered rectangular \rightarrow lamellar transformation on increasing α . We have also examined complexes of these polyelectrolytes with the

double-tailed cationic surfactant didodecyldimethylammonium bromide (DDAB). The phase behaviour of the DDAB-water system and earlier work on complexes formed by DDAB with PGA are dealt with in section 5.5 . Our experimental results on DDAB-polyelectrolyte complexes are also discussed here. As discussed in section 5.6.1, our results on CTAB-SHN-polyelectrolyte complexes suggest the importance of poly-ion specificity in determining their structures. All DDAB-polyelectrolyte complexes exhibit a lamellar phase but the lattice parameter varies depending on the polyelectrolyte used. We also find that the weight fraction of the surfactant is the highest in PSS complexes and the least in DNA complexes. A similar trend is also seen in complexes of polyelectrolytes with CTAB as well as CTAB-SHN. This helps us to establish a correlation between the structure of the complexes and that of the surfactant-water system at similar surfactant content as discussed in section 5.6.2. Finally in section 5.7, we state the conclusions that can be drawn from the experiments discussed in this chapter.

5.2 Earlier studies

The complex formation between proteins and cationic detergents was first reported by Kuhn in 1940 [1, 2]. Later it was found to be a general phenomenon for anionic polyelectrolytes [3]. These complexes dissolve in the presence of salt [4]. These observations were made use of in the purification of anionic polysachcharides from biological tissues. Some of the earlier studies involved monitoring the binding of surfactants to polyelectrolytes using surfactant-selective electrodes [5]. Later NMR spectroscopy [6], small angle neutron scattering (SANS) and fluorescence techniques [7] were used to probe the structures in polyelectrolyte-surfactant systems.

One of the detailed studies on the phase behaviour of surfactant-polyelectrolyte systems has been by Thalberg et al [8] on didodecyltrimethyl ammonium bromide (DTAB)-poly (acrylic acid) (NaPA)-water and DTAB-sodium hyaluronate (NaHy)-water systems. The

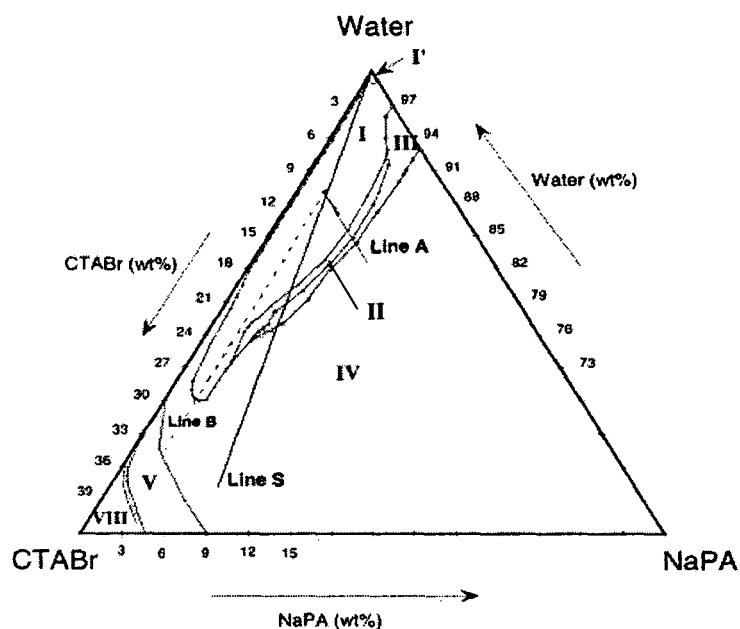


Figure 5.1: Phase diagram of CTAB-NaPA-water system [11].

complex formation occurs over a larger range of surfactant and polyelectrolyte concentration for complexes of DTAB with NaPA as compared to NaHy. Hence stronger interactions are indicated in NaPA complexes as compared to NaHy complexes, possibly due to the higher bare charge density of NaPA. The interactions in complexes of the anionic surfactant sodium dodecylsulphate (SDS) with cationic polyelectrolyte, poly(diallyldimethylammonium chloride) (PDADMAC) were found to be stronger than in the DTAB-NaPA system. This has been attributed to the smaller size of the surfactant head group of the anionic as compared to cationic surfactants [9, 10].

More detailed study of the phase behaviour of the CTAB-NaPA system has been carried out by Ilekci et al. [11, 12]. The phase diagram of NaPA-CTAB-water is given in fig 5.1. Dilute micellar solutions of CTAB with NaPA separate into a dilute aqueous phase and a concentrated mesophase containing the complex (cream phase) at the top (region I). Small angle diffraction studies indicate that these complexes have a hexagonal structure. The lattice parameter is in the range 5-6 nm, and is comparable to that of the hexagonal phase of CTAB-water system. At high dilutions (at surfactant concentrations close to CMC), a com-

plex with a cubic structure is obtained (region I'). A third phase appears between the cream and the aqueous phase on increasing the surfactant as well as polyelectrolyte concentration (region II). This is found to be an isotropic concentrated micellar phase. On further addition of NaPA the mesophase vanishes (region III). Finally the dilute aqueous phase vanishes at higher NaPA concentrations (region IV). At a fixed NaPA concentration along line B, the two phase region disappears at a surfactant concentration of $\sim 27\%$. CTAB-water system forms a hexagonal phase above 30% surfactant concentration. Between 30-37% the addition of polyelectrolyte leads to a hexagonal \rightarrow nematic \rightarrow micellar transition on increasing the polyelectrolyte concentration. Thus two opposite trends are exhibited in the dilute and concentrated CTAB solutions. The addition of NaPA to a dilute micellar solution leads to the phase separation of a concentrated mesophase, whereas the addition of the polyelectrolyte to a concentrated solution leads to the formation of an isotropic phase.

Thus on addition of NaPA to CTAB-water, three types of effects have been observed.

- i) The CTA^+ micelles retain their rod-like shape but the distances are collapsed (region I).
- ii) The distances remain the same but the shapes change.
- iii) Both the distances and the shapes change as seen in the cubic phase.

The formation of a CTAB-NaPA complex involves the exchange of Br^- counter ion of CTAB with acetate (Ac^-) ion. Cetyltrimethylammonium acetate (CTAAc)-water system is known to form a cubic phase over a large range of surfactant concentration. It has a body-centered cubic unit cell, with large micelles at the apexes and center of a cube and pairs of smaller anisotropic micelles at the centers of the faces [13]. The formation of the cubic phase in dilute CTAB-NaPA solution can, therefore, be attributed to the nearly complete exchange of the Br^- and Ac^- ions. At higher surfactant contents when the ion exchange is less, a hexagonal phase is observed. The decrease in the inter-micellar distance can be understood in terms of the formation of polyion bridges between the micelles. Thus these studies show that the sequence of phases in these ternary systems is determined by the extent of counter ion exchange and by the water content.

Some studies have also probed the structures of these complexes when dried. It is found that stable membranes can be made from these dry complexes. The chain melting transition of the bilayers in the complex was found to shift to higher temperatures on drying. The permeability of these membranes can be modulated by small electric fields [14]. They are found to dissolve in organic solvents where they exhibit polyelectrolyte behaviour. X-ray investigations on the alkyltrimethylammonium bromide-poly (styrene sulfonate) (PSS) dry complexes reveal a lamellar phase with a periodicity ranging from 2.9 nm to 4.1 nm depending on the alkyl chain length of the surfactant. The ability to form liquid crystalline phases and their high solubility in organic solvents make them suitable materials for optoelectronics, ion separation membranes and molecular composites. A lamellar phase has also been reported in dry complexes of CTAB and dodecyltrimethylammonium bromide (DTAB) with PGA [15]. On heating, the complexes are found to be stable up to 150°C.

There have also been a few investigations on the structures of complexes formed by cationic surfactants with polyelectrolyte gels [16]. The structures of DTAB with cross-linked NaPA gels have been probed using small angle x-ray scattering (SAXS). The surfactant aggregation number and the ordering of micelles were investigated using time resolved fluorescence quenching. The surfactant concentration was kept well below the critical micellar concentration (CMC). A collapse of the gel was observed on increasing the CTAB concentration. Above a critical concentration, a $Pm3n$ cubic phase was observed. On increasing the surfactant concentration above CMC, a hexagonal order was found in the 2D collapsed gel. The aggregation number was found to increase from 50 to 100 on increasing the surfactant concentration. This indicated that the aggregates that were initially globular formed short rods, at higher concentrations.

A more detailed study has been carried out on complexes of cationic surfactants with gels of anionic polyelectrolytes such as PSS and poly(sodium methacrylate) (PMAA) [17]. It was found that the alkyl chain length of the surfactant influences the formation of highly ordered

It was found that the liquid crystalline phases are formed in the same sequence and with similar structures in the polyelectrolyte-surfactant-water system as in the surfactant-water system. Increase in the alkyl chain length leads to a sequence of structures ranging from a disordered micellar $\rightarrow hcp \rightarrow bcc \rightarrow$ hexagonal \rightarrow lamellar phase. A similar sequence of transitions are obtained in the surfactant-water system by increasing the concentration of the surfactant. Increasing the temperature and decreasing the charge density of the polyelectrolytes in the complex were found to have similar effects on the structure of the complex. SANS studies indicate that the cationic starch has a helical conformation. When they associate with surfactants, more compact cylindrical aggregates are formed in which a core of surfactant is surrounded by the helical chains of cationic starch [20].

As discussed above, there have been several studies on the structures of polyelectrolyte-surfactant systems. However, the influence of the shape of the aggregates on the structure of the complex has not been probed systematically in any of these systems. Hence we have tuned the spontaneous curvature of the micelles in the dilute surfactant solution and examined the role of the aggregate morphology on the structure of the complex. This has been achieved using SHN which transforms CTAB aggregates from cylinders to bilayers, as described in chapter 2. The structure of the complex could also be specific to the chemical nature of the polyion. Not many of the earlier studies examined these systems from this perspective. Hence using four polyelectrolytes, which differ widely in the chemical nature of their charge moieties, bare charge density and persistence length, in addition to the single and double stranded DNA (discussed in chapter 3), we have made a comparative study of the structures of the complexes obtained in dilute solution of CTAB-SHN.

5.3 CTAB-polyelectrolyte complexes

A 10 mM CTAB solution was prepared and the polyelectrolyte was then added to it (table 5.1). Complexes, which precipitate out, were left in the solution for two days. The

Table 5.1: The bare charge densities and persistence lengths of the polyelectrolytes used, namely, double stranded (ds) DNA, single stranded (ss) DNA, poly (glutamic acid) (PGA), poly (acrylic acid) (PAA), poly (vinyl sulfonate) (PVS), poly (styrene sulfonate) (PSS).

Polyelectrolyte	bare charge density	l_p (nm)
ds DNA	$1 \bar{e}/0.17 \text{ nm}$	50
ss DNA	$1 \bar{e}/0.59 \text{ nm}$	1.5
PGA	$1 \bar{e}/0.154 \text{ nm}$	2
PAA	$1 \bar{e}/0.32 \text{ nm}$	1
PVS	$1 \bar{e}/0.32 \text{ nm}$	1
PSS	$1 \bar{e}/0.25 \text{ nm}$	10

precipitates were then transferred to a 1 mm glass capillary for x-ray diffraction studies. CTAB-polyelectrolyte complexes were found to be birefringent under a polarizing microscope. The complexes were prepared by varying the polyelectrolyte concentration ρ (= weight of CTAB/ weight of polyelectrolyte), above and below the isoelectric point ρ_{iso} , where the positive charges of the CTA^+ ions are balanced by the negative charges on the polyelectrolyte. The experimental observations were made at a temperature of 30°C.

X-ray diffraction studies on all four CTAB-polyelectrolyte complexes reveal three peaks in the small angle region (fig. 5.2). The scattering vectors are in the ratio $1:\sqrt{3}:2$, which correspond to the (1 0), (1 1) and (2 0) peaks of a 2D hexagonal lattice. The lattice parameters are in general found to vary depending on the polyelectrolyte used. Though PVS and PSS complexes have similar lattice parameters, in CTAB-PVS complexes we obtain peaks corresponding to the (1 0), (2 0) and (2 1) reflections of a 2D hexagonal lattice (fig 5.2c). The lattice parameters and the peak positions for the different complexes are given in table 5.2. The effect of the polyelectrolyte and surfactant concentration on the lattice parameter was studied for CTAB- poly (glutamic acid) (PGA) complexes. The peak positions were found to be independent of ρ , and of CTAB concentration up to 100 mM. These observations are in broad agreement with the earlier experiments on CTAB-polyelectrolyte complexes in aqueous solutions [11, 17].

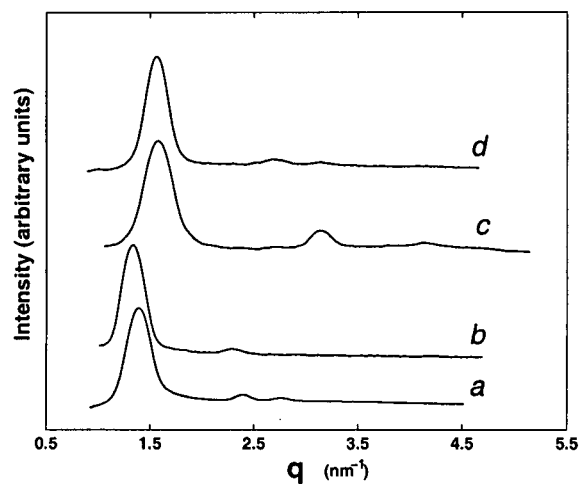


Figure 5.2: Diffraction patterns of the CTAB-polyelectrolyte complexes. ρ (= wt. of CTAB/wt of polyelectrolyte) and ρ_{iso} are 6.0, 3.88 for PAA (a); 1.8, 2.41 for PGA (b); 1.8, 1.78 for PSS (c); 1.15, 2.8 for PSS (d); CTAB concentration in the aqueous solution was 10 mM .

Table 5.2: The d-spacings, lattice parameters and structure of CTAB-polyelectrolyte complexes; a denotes the lattice parameter.

polyelectrolyte	$d_1(nm)$	$d_2(nm)$	$d_3(nm)$	$d_4(nm)$	$a(nm)$	structure
PAA	4.48	2.59	2.24		5.17	2-D hexagonal
PGA	4.61	2.67			5.33	2-D hexagonal
PSS	4.02	2.32	2.01		4.64	2-D hexagonal
PVS	4.0	2.31	2.0	1.52	4.64	2-D hexagonal

5.4 CTAB-SHN-polyelectrolyte complexes

Complexes were prepared using appropriate CTAB, SHN and polyelectrolyte concentrations. CTAB concentration was 10 mM. SHN concentration α ($=[\text{SHN}]/[\text{CTAB}]$), was varied from 0 to 0.7. The polyelectrolyte concentration ρ was varied over a wide range about the isoelectric point ρ_{iso} . The complexes were found to be birefringent under a polarizing microscope. X-ray diffraction studies of the complexes were carried out to probe their structure.

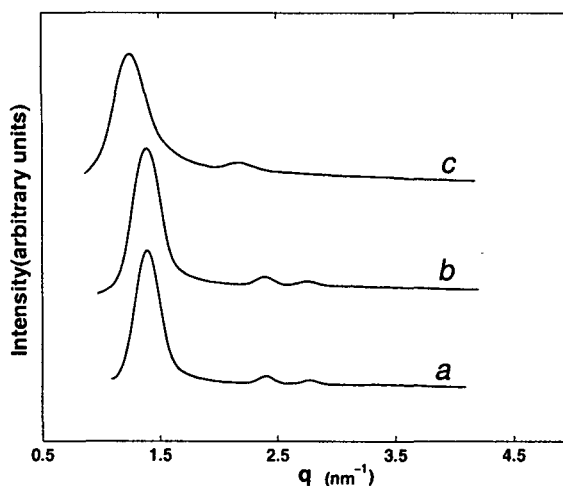


Figure 5.3: Diffraction patterns of the CTAB-SHN-PAA complexes in the hexagonal phase. α and ρ for the different curves are: 0.2, 6 (a); 0.2, 4 (b); 0.4, 0.6 (c), $\rho_{iso}=4.85$ at $\alpha=0.2$; $\rho_{iso}=6.47$ at $\alpha=0.4$; CTAB concentration in the aqueous solution was 10 mM .

In CTAB-SHN-PAA complexes, the diffraction patterns show three peaks in the small angle region, which can be indexed on a 2D hexagonal lattice (fig 5.3a). The hexagonal phase was found to occur up to $\alpha = 0.4$. The peak positions remained independent of polyelectrolyte concentration above and below ρ_{iso} (fig 5.3a, b). The lattice parameter of the hexagonal phase however increases with SHN concentration (fig 5.3c). At $\alpha = 0.5$, diffraction pattern shows additional peaks in the small angle region (fig. 5.4a) which could not be indexed on a hexagonal or a lamellar lattice. However, they could be indexed as the (2 0), (1 1) and (0 2) peaks of a centered rectangular lattice. Similarly, at $\alpha = 0.6$, the x-ray diffraction pattern has 5 peaks in the small angle region (fig 5.4c). They could also be indexed as

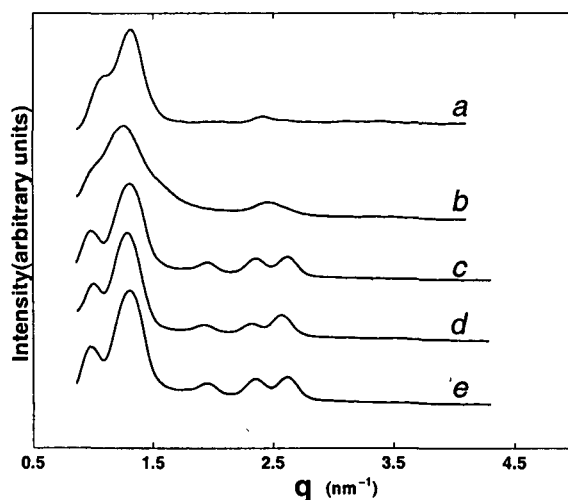


Figure 5.4: Diffraction patterns of the CTAB-SHN-PAA complexes. α and ρ for the different curves are: 0.5, 0.6 (a); 0.6, 0.6 (b); 0.6, 0.84 (c); 0.6, 12 (d); 0.7, 0.72 (e); $\rho_{iso}=7.76$ at $\alpha=0.5$; $\rho_{iso}=9.7$ at $\alpha=0.6$; $\rho_{iso}=12.93$ at $\alpha=0.7$.

Table 5.3: The d-spacings, structure and lattice parameters of CTAB-SHN-PAA complexes at different values of α and ρ . a and b denote the lattice parameters. R denotes a phase with a centred rectangular lattice. The concentration of CTAB in the solution was 10 mM.

α	ρ_{iso}	ρ	$d_1(nm)$	$d_2(nm)$	$d_3(nm)$	$d_4(nm)$	$d_5(nm)$	phase	$a(nm)$	$b(nm)$
0	3.88	6	4.48	2.59	2.24			hexagonal	5.17	
0.2	4.85	0.6	4.38							
0.2	4.85	6	4.51	2.63	2.25			hexagonal	5.21	
0.4	6.47	0.6	4.88	2.99	2.67			hexagonal	5.64	
0.5	7.76	0.6	6.13	4.75		2.64	2.6	R	12.26	5.28
0.6	9.7	0.6	6.25	5.03		2.57				
0.6	9.7	0.84	6.45	5.03	3.34	2.76	2.50	R	12.90	5.52
0.6	9.7	12	6.27	4.84	3.24	2.66	2.39	R	12.54	5.32
0.7	12.93	0.72	6.23	4.86	3.27	2.70	2.43	R	12.66	5.40

the (2 0), (1 1), (3 1), (0 2) and (2 2) reflections from a 2D centered rectangular lattice. This was also true at $\alpha = 0.7$ (fig 5.4e). The peak positions were found to be independent of the polyelectrolyte concentration and weakly dependent on SHN concentration (fig 5.4c, d). The peak positions and the lattice parameters for the various complexes are given in table 5.3.

For $\alpha < 0.5$, the CTAB-SHN-PGA complexes show three peaks in the small angle region with their q values in the ratio 1: $\sqrt{3}$:2 (fig 5.5a,b). These peaks could be indexed as the (1 0), (1 1) and (2 0) reflections of a 2D hexagonal lattice. The lattice parameter a , of the hexag-

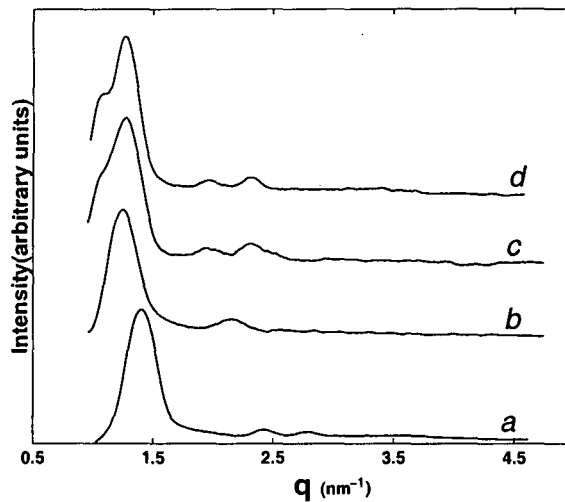


Figure 5.5: Diffraction patterns of the CTAB-SHN-PGA complexes. α and ρ for the different curves are: 0.2, 1.5 (a); 0.4, 1.93 (b); 0.5, 12 (c); 0.55, 0.72 (d); $\rho_{iso}=3.02$ at $\alpha=0.2$; $\rho_{iso}=4.02$ at $\alpha=0.4$; $\rho_{iso}=4.82$ at $\alpha=0.5$; $\rho_{iso}=5.36$ at $\alpha=0.55$;

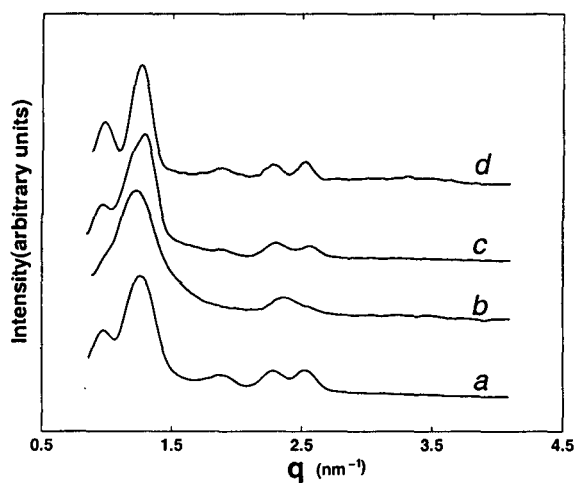


Figure 5.6: Diffraction patterns of the CTAB-SHN-PGA complexes. α and ρ for the different curves are: 0.6, 12 (a); 0.6, 1.8 (b); 0.6, 3.6 (c); 0.7, 6 (d); $\rho_{iso}=6.0$ at $\alpha=0.6$; $\rho_{iso}=8.0$ at $\alpha=0.7$;

Table 5.4: The d-spacings, structure and lattice parameters of CTAB-SHN-PGA complexes at different values of α and ρ . R denotes a phase with a centred rectangular lattice. a and b denote the lattice parameters.

α	ρ_{iso}	ρ	$d_1(nm)$	$d_2(nm)$	$d_3(nm)$	$d_4(nm)$	$d_5(nm)$	phase	$a(nm)$	$b(nm)$
0	2.41	1.8	4.61	2.66				hexagonal	5.33	
0.2	3.02	1.5	4.64	2.67	2.32			hexagonal	5.36	
0.4	4.02	1.93	5.06	2.92				hexagonal	5.84	
0.5	4.82	12.0	6.16	5.03	3.23	2.74		R	12.12	5.48
0.55	5.36	0.72	6.13	4.98	3.21	2.72		R	12.26	5.46
0.6	6.0	1.8	6.45	5.13		2.64				
0.6	6.0	3.6	6.43	4.96	3.32	2.75	2.48	R	12.86	5.48
0.6	6.0	12.0	6.45	4.90	3.32	2.75	2.48	R	12.9	5.48
0.7	8.0	6	6.33	4.98	3.30	2.75	2.49	R	12.46	5.5

onal structure gradually increases with α from 5.33 nm to 5.84 nm (table 5.4). Above $\alpha = 0.5$, the peaks could be indexed as the (2 0), (1 1), (3 1) (0 2) and (2 2) reflections of a 2D rectangular lattice (fig 5.5 c,d). The peak positions in this phase was found to be independent of polyelectrolyte concentration (fig 5.6a,b). Similarly, the lattice parameters of this phase was only weakly dependent on SHN concentration (fig 5.6c,d). Similar trends are found in both the PAA and PGA complexes with the lattice parameters remaining insensitive to ρ and being weakly dependent on SHN concentration (table 5.3, 5.4). Hence the structures of CTAB-SHN-PGA complexes are similar to those of the PAA complexes.

A hexagonal phase is also observed in CTAB-SHN-PVS complexes for $\alpha < 0.4$ (fig 5.7a). The lattice parameter of the hexagonal lattice increases from 4.67 nm at $\alpha=0$ to 5.16 nm for $\alpha = 0.2$. At $\alpha=0.4$, four peaks are observed in the small angle region which can be indexed as the (2 0),(1 1),(3 1) and (0 2) reflections of a 2D centered rectangular lattice (R) (fig 5.7b). The peak positions remain the same for α in the range 0.4 to 0.7 (fig 5.7b,c). At $\alpha = 0.7$ and above, two peaks appear with the scattering vector q in the ratio 1:2 (fig 5.8a,b), corresponding to a lamellar structure. The position of the first order peak here remains the same as that of the (1 1) reflection seen at $\alpha = 0.6$ (fig 5.7c). The lattice parameters of the different structures seen in this system are given in table 5.5.

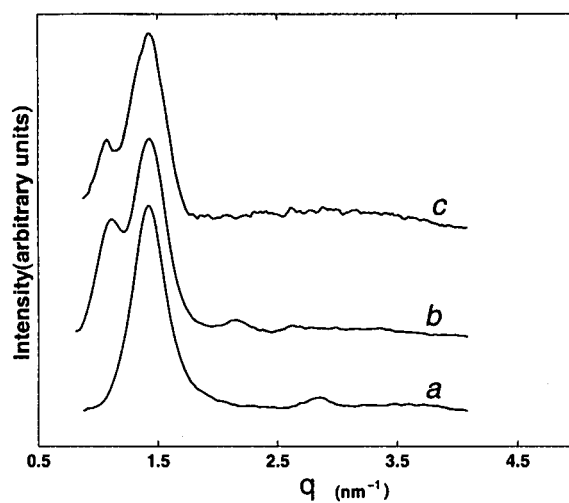


Figure 5.7: Diffraction patterns of the CTAB-SHN-PVS complexes. α and ρ for the different curves are: 0.2, 1.15 (a); 0.4, 1.15 (b); 0.6, 1.92 (c); $\rho_{iso}=3.5$ at $\alpha=0.2$; $\rho_{iso}=4.67$ at $\alpha=0.4$; $\rho_{iso}=7.0$ at $\alpha=0.6$;

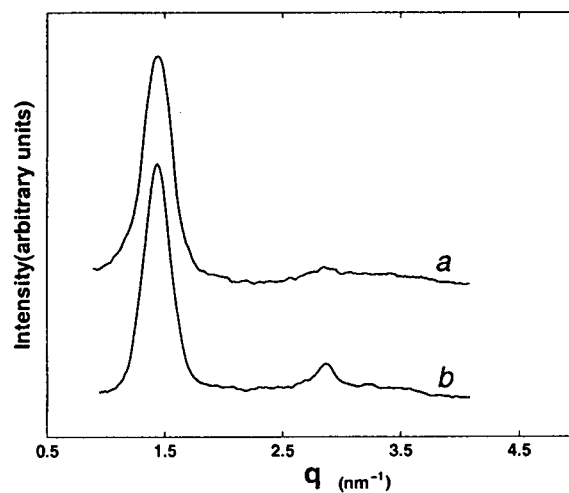


Figure 5.8: Diffraction patterns of the CTAB-SHN-PVS complexes. α and ρ for the different curves are: 0.7, 1.15 (a); 0.75, 1.15 (b); $\rho_{iso}=9.33$ at $\alpha=0.7$; $\rho_{iso}=9.99$ at $\alpha=0.75$;

Table 5.5: The d-spacings, structure and lattice parameters of CTAB-SHN-PVS complexes at different values of α and ρ . R denotes a phase with a centred rectangular lattice. a and b denote the lattice parameters.

α	ρ_{iso}	ρ	$d_1(nm)$	$d_2(nm)$	$d_3(nm)$	$d_4(nm)$	phase	$a(nm)$	$b(nm)$
0	2.8	1.15	4.00	2.31	2.00	1.52	hexagonal	4.6	
0.2	3.5	1.15	4.47		2.23				
0.4	4.67	1.15	5.67	4.37	2.93	2.37	R	11.34	4.74
0.5	5.6	1.15	5.67	4.47					
0.55	6.2	1.15		4.47					
0.6	7.0	1.92	5.85	4.34	2.17				
0.7	9.33	1.15	4.34	2.17			lamellar	4.34	
0.75	9.99	1.15	4.34	2.17			lamellar	4.34	

In CTAB-PSS complexes the diffraction patterns indicate that the structure of the complex remains hexagonal at low SHN concentration (fig 5.9a). At $\alpha = 0.4$, four peaks are obtained in the small angle region that could not be indexed on a 2-D centered rectangular or a hexagonal lattice (fig 5.9b,c). The lamellar phase also had to be ruled out from the peak positions. Unlike in the centred rectangular phases of PAA , PGA or PVS complexes, the first peak was found to be more intense than the higher order peaks. The peaks could be indexed as the (2 0), (1 1), (2 1), (0 2), (3 1) and (4 1) reflections of a rectangular lattice corresponding to the plane group pgg (fig 5.9c). The peak positions of the pgg lattice, are sensitive to the SHN concentration. At a higher SHN concentration where $\alpha= 0.7$, x-ray diffraction gives three peaks in the small angle region with no specific relationship between the values of q (fig 5.10). Additional peaks could not be observed even after very long exposures, and hence we have not been able to determine the structure of this phase. The peak positions in all these complexes are found to be independent of ρ . At $\alpha=0.75$, we find that the complex dissolves for ρ above and below ρ_{iso} . The structures and the lattice parameters of CTAB-SHN-PSS complexes are given in table 5.6.

We have also studied the influence of these polyelectrolytes on dilute solutions of the

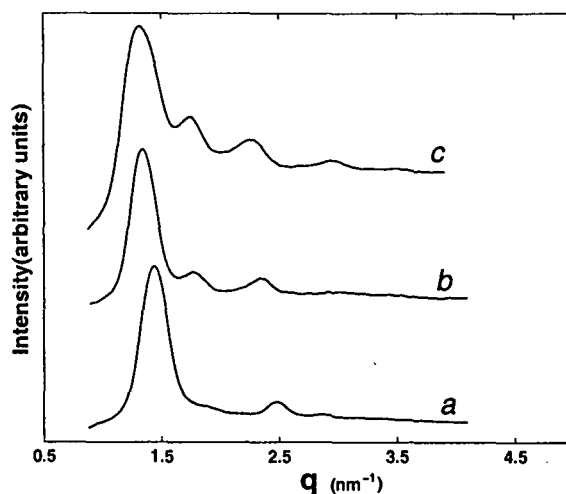


Figure 5.9: Diffraction patterns of the CTAB-SHN-PSS complexes. α and ρ for the different curves are: 0.2,2.25 (a); 0.5,3.6 (b); 0.6,4.5 (c); $\rho_{iso}=2.23$ at $\alpha=0.2$; $\rho_{iso}=3.56$ at $\alpha=0.5$; $\rho_{iso}=4.45$ at $\alpha=0.6$;

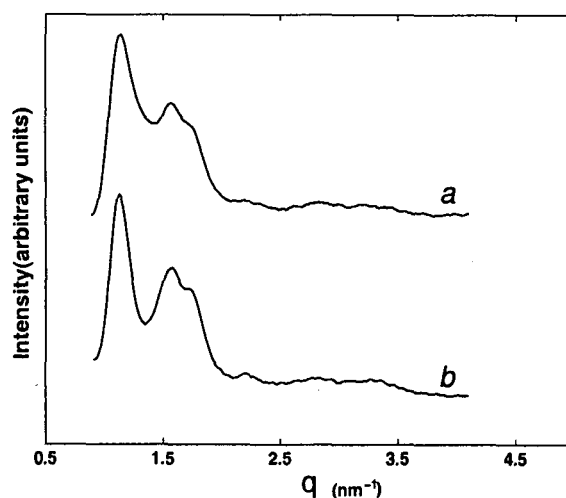


Figure 5.10: Diffraction patterns of the CTAB-SHN-PSS complexes. α and ρ for the different curves are: 0.7, 3.6 (a); 0.7, 12.0 (b); $\rho_{iso}=5.93$ at $\alpha=0.7$.

Table 5.6: The d-spacings, structure and lattice parameters of CTAB-SHN-PSS complexes at different values of α and ρ . a and b denote the lattice parameters.

α	ρ_{iso}	ρ	d_1 (nm)	d_2 (nm)	d_3 (nm)	d_4 (nm)	phase	a (nm)	b (nm)
0	1.78	1.8	4.02	2.32	2.01		hexagonal	4.6	
0.2	2.23	2.25	4.37	2.53	2.18		hexagonal	5.04	
0.4	2.97	3	5.15						
0.5	3.56	3.6	4.67	3.46	2.68		<i>pgg</i>	9.34	5.36
0.6	4.45	4.5	4.84	3.56	2.77	2.14	<i>pgg</i>	9.68	5.54
0.7	5.93	3.6	5.58	4.02	3.59				
0.7	5.93	12	5.58	4.02	3.59				

double-tailed cationic surfactant didodecyldimethylammonium bromide (DDAB), which forms bilayers at all concentrations. Their structures are discussed below.

5.5 DDAB-polyelectrolyte complexes

5.5.1 Phase diagram of DDAB-water

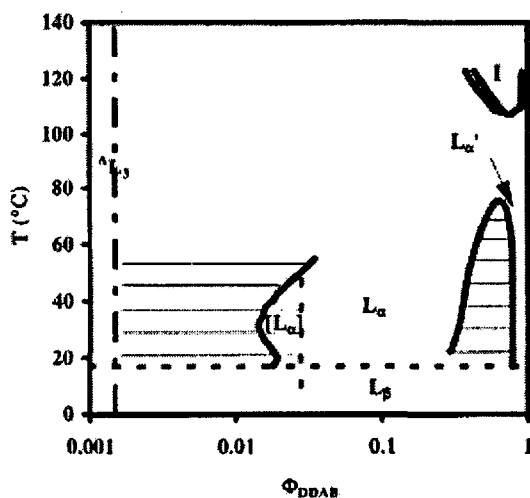


Figure 5.11: Phase diagram of DDAB-water system. L_α refers to the swollen lamellar phase. L'_α is the collapsed lamellar phase, L_β denotes the gel phase, and I the isotropic phase [21]

The phase diagram of the DDAB-water system has been studied extensively in the context of an anomalous attractive interaction between charged bilayers [21]. At low surfactant concentration the isotropic solution consists of unilamellar vesicles (L_3). The DDAB-water system is found to exhibit two coexisting lamellar phases at high surfactant concentration (fig 5.11). The lamellar phase (L_α) found at lower surfactant concentration shows the usual swelling behaviour given by

$$d = \delta_m / (1 - \phi_w) \quad (5.1)$$

Here d is the lamellar periodicity, δ_m the thickness of bilayer and ϕ_w the weight fraction of water.

On increasing the surfactant concentration, x-ray diffraction studies reveal in addition to the

lamellar peaks corresponding to L_α , peaks coming from a periodicity of 3.12 nm. The bilayer thickness of DDAB \sim 2.4 nm. Hence the second set of peaks correspond to a lamellar phase (L'_α) where the bilayers are collapsed with very little water between them. At 30°C, there is a large region of coexistence of L_α and L'_α . On increasing the temperature the coexistence range decreases, leading to a critical point at 73°C. In charged bilayer systems, the interactions between the bilayers is repulsive, owing to which the separation between the bilayers in the lamellar phase is determined by the water content. The appearance of a condensed phase (L'_α) at intermediate surfactant concentrations indicates that the interactions become attractive at these inter-bilayer separations. Such a behaviour has not been seen in other cationic surfactant systems like didodecyldimethylammonium chloride (DDACl)- water. Though the origin of the attractive interaction responsible for this behaviour is not known at present, they are suspected to arise from the condensation of Br^- counterions near the bilayer-water interface at these surfactant concentrations.

5.5.2 Earlier studies on DDAB-polyelectrolyte complexes

Mixtures of DDAB and the neutral lipid dilauroyl-sn-glycerophosphocholine (DLPC) form lamellar complexes with PGA [22]. By keeping ϕ_{PC} (= weight of neutral lipid/ total weight of the lipid) fixed and varying the PGA concentration, the lamellar periodicity remains constant at 5 nm. However at very low PGA concentrations ($\rho > \rho_{iso}$), faint additional peaks appear at small angles with $d \sim 7$ nm. On varying ϕ_{PC} from 0 to 0.9, keeping ρ fixed at ρ_{iso} , the d-spacing increases from 3.9 nm to 6 nm (fig 5.12). This behaviour was found to be independent of the molecular weight of the PGA used. Surprisingly no additional peaks corresponding to PGA-PGA correlation have been observed.

The thickness of DDAB-DLPC bilayers at $\phi_{PC} = 0.5$ is nearly 3.14 nm. PGA molecules form a α -helix when complexed with cationic surfactants [23] with a diameter of 1.3 nm. Hence the lamellar periodicity of 5 nm is consistent with a bilayer thickness of \sim 3.2 nm

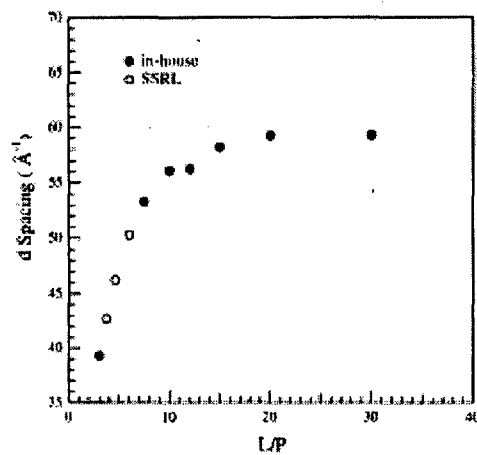


Figure 5.12: Plot of d spacing obtained as a function of L/P (= total weight of cationic and neutral lipid/ weight of PGA) [22].

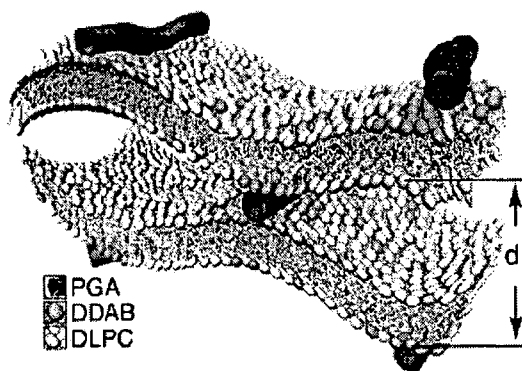


Figure 5.13: Schematic of the local lipid-PGA complex structure showing the 'pinching mechanism'. At larger length scales, the PGA macromolecules are positionally and orientationally disordered [22].

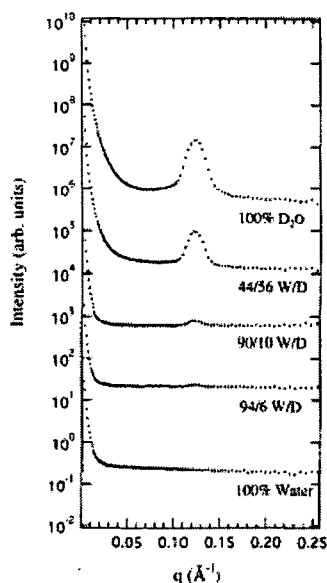


Figure 5.14: Small angle neutron scattering studies (SANS) data from DDAB-DLPC-PGA complexes at various solvent scattering densities [22].

and a PGA strand with two hydration shells ~ 1.8 nm. The swelling behaviour observed on increasing ϕ_{PC} at ρ_{iso} has been seen also in DDAB-DLPC-DNA system [24]. The increase in d-spacing on diluting the charge density of the bilayers, has led to the proposal of a pinched lamellar structure in these systems. This consists of locally pinched regions of DDAB and PGA with the d-spacing away from these regions determined by DLPC (fig 5.13). However the pinching mechanism proposed here has not been well established. PGA being flexible, with a persistence length $l_p \sim 2$ nm, a lamellar phase consisting of bilayers bridged by polyions cannot be ruled out.

Even if positional correlations exist between the PGA chains in the plane of the bilayer, the PGA-PGA peaks would be absent if there is no sufficient contrast between the PGA molecules and solvent. This can arise since the electron density of PGA molecules is nearly the same as that of water. However the contrast may be increased by using small angle neutron scattering techniques (SANS). Here the scattering length can be varied by changing the ratio of H_2O to D_2O . At high H_2O content, the scattering length of lipid and solvent are closely matched. Hence the scattering should be mainly from PGA molecules. However no

peaks are observed under these conditions (fig 5.14). On increasing the amount of D_2O , the contrast between the lipid and solvent increases, and a peak appears at 5 nm indicating the scattering from the lamellar complex.

Thus the structure in the lamellar phase of lipid-PGA systems are found to be different from those observed in lipid-DNA complexes. PGA strands, unlike the ds DNA, do not exhibit any order in the plane of the bilayer. Though PGA has a bare charge density comparable to that of ds DNA, its persistence length is an order of magnitude lower. Hence the absence of PGA-PGA correlations can be attributed to the low persistence length of PGA.

5.5.3 Structure of DDAB-polyelectrolyte complexes

All complexes appear as white precipitates phase separating out of the aqueous solution. They are found to be birefringent under a polarizing microscope. The complexes in general form a lamellar structure. In DDAB-ds DNA complexes the peak positions do not shift significantly on increasing the DNA concentration (fig 5.15b,c). Hence the lattice parameter of the DDAB-ds DNA complexes remain at 4.51 nm, nearly independent of DNA concentration on varying ρ across ρ_{iso} . However at high DNA concentration, a shoulder appears on the first order peak at 3.69 nm (fig 5.15c). A broad peak appears at 2.51 nm for ρ below ρ_{iso} (fig 5.15b). We have also studied the complexes formed by ss DNA with DTAB. The lamellar periodicity of these complexes is 4.15 nm (fig 5.15a).

The diffraction pattern of DDAB-PGA complexes give two peaks in the small angle region with their q values in the ratio 1:2, indicating a lamellar structure for the complex (fig 5.16a). These complexes have a periodicity of 3.82 nm for $\rho > \rho_{iso}$. On increasing the PGA concentration, the lattice parameter decreases to 3.43 nm for $\rho < \rho_{iso}$. The diffraction pattern of DDAB-PAA complexes also consists of two peaks (fig 5.16b) indicating a lamellar structure with a spacing of 3.46 nm for $\rho > \rho_{iso}$ and a spacing of 3.22 nm for $\rho < \rho_{iso}$. The x-ray

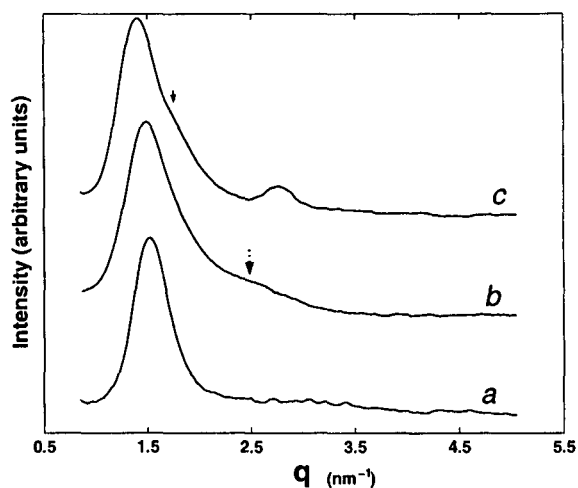


Figure 5.15: Diffraction patterns of the DDAB-DNA complexes. DDAB-ss DNA complex at $\rho = 9.2$ (a). DDAB-ds DNA complex with $\rho = 9.2$ (b); $\rho = 0.92$ (c); $\rho_{iso} = 0.71$; The arrow in curve (b) indicates the peak due to the scattering from the helical structure of the DNA strand; The arrow in curve (c) indicates the DNA-DNA peak; DDAB concentration in the aqueous solution is 10 mM .

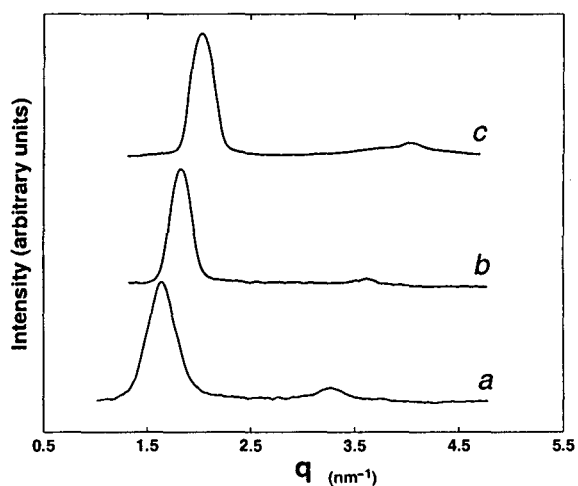


Figure 5.16: Diffraction patterns of : (a) DDAB-PGA complex at $\rho = 9.2$; $\rho_{iso} = 3.07$, (b) DDAB-PAA complex at $\rho = 0.92$; $\rho_{iso} = 4.59$, (c) DDAB-PVS complex at $\rho = 0.92$; $\rho_{iso} = 3.57$.

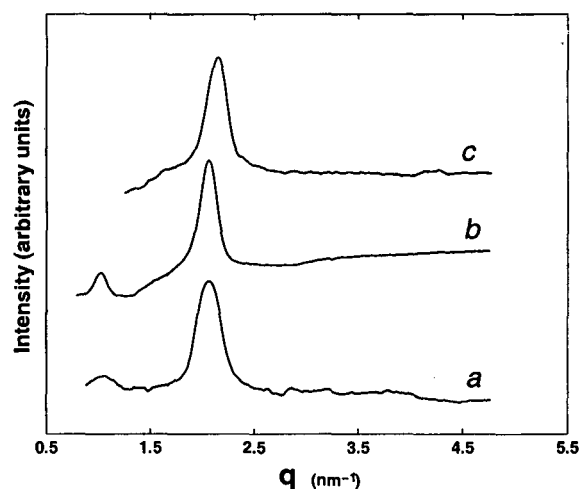


Figure 5.17: Diffraction patterns of DDAB-PSS complexes at different values of ρ . $\rho = 4.6$ (a); $\rho = 2.2$ (b); $\rho = 1.25$ (c). $\rho_{iso} = 2.25$. DDAB concentration in the aqueous solution is 10 mM.

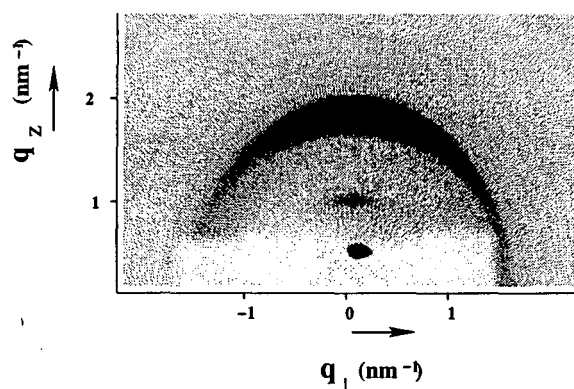


Figure 5.18: Diffraction pattern of a partially oriented DDAB-PSS complex; $\rho = 1.65$; $\rho_{iso} = 2.25$.

diffraction pattern of complexes of PVS with DDAB also give two peaks in the small angle region (fig 5.16c) showing a lamellar structure with the periodicity decreasing from 3.18 nm to 3.09 nm on increasing the PVS concentration.

The complexes of PSS with DDAB however show a very different behaviour. At $\rho > \rho_{iso}$, two peaks appear in the small angle region with no definite relationship between their q values (fig 5.17 a,b). The intensity of the peak at 5.95 nm is found to be lower than the peak at 3.03 nm. The peak at 5.95 nm remains nearly independent of the polyelectrolyte concentration. However at high PSS concentration, much below ρ_{iso} , the peak at 5.95 nm

Table 5.7: Relative intensities of the first peak (I_1) w.r.t the second peak (I_2) at different values of ρ in DDAB-PSS complexes. $\rho_{iso} = 2.25$.

ρ	I_1/I_2
9.01	0.01
4.6	0.048
3.1	0.027
2.2	0.063
1.65	0.029

Table 5.8: The d-spacings and lattice parameters of DDAB-polyelectrolyte complexes at various polyelectrolyte concentrations. d denotes the lattice parameter.

polyelectrolyte	ρ_{iso}	ρ	$d_1(nm)$	$d_2(nm)$	d (nm)
ds DNA	0.71	9.2	4.51	2.25	4.51
ds DNA	0.71	0.92	4.50	2.25	4.50
ss DNA	0.71	9.2	4.15		4.15
PGA	3.07	9.2	3.82	1.91	3.82
PGA	3.07	0.92	3.53	1.75	3.53
PAA	4.59	11.56	3.48		3.48
PAA	4.59	8.66	3.46	1.73	3.46
PAA	4.59	5.56	3.45	1.73	3.45
PAA	4.59	0.92	3.22		3.22
PVS	3.57	10.02	3.18		3.18
PVS	3.57	7.66	3.18		3.18
PVS	3.57	4.7	3.11		3.11
PVS	3.57	0.92	3.09		3.09
PSS	2.25	9.2	6.08	3.03	
PSS	2.25	4.6	5.96	3.03	
PSS	2.25	3.10	5.95	3.03	
PSS	2.25	2.20	6.22	3.04	
PSS	2.25	1.65	5.84	2.92	
PSS	2.25	1.25	2.99	1.50	2.99
PSS	2.25	0.9	2.96	1.48	2.96

disappears (fig 5.17c). In an oriented sample of DDAB-PSS complex (fig 5.18), the peaks occur at $q_z = 1.04 \text{ nm}^{-1}$ and at 2.12 nm^{-1} . No peaks appear along q_{\perp} direction. On increasing the temperature up to $70 \text{ }^{\circ}\text{C}$ the peak positions remain at around 6 nm and 3.03 nm respectively. But on increasing the temperature to $75 \text{ }^{\circ}\text{C}$, the peak at 6 nm disappears. Also no peaks could be observed due to the scattering from the supernatant, indicating that the peaks at $6.03 \pm 0.1 \text{ nm}$ and at 3.03 nm occur due to the scattering from the complex.

The relative intensities of the peaks were calculated after geometric corrections. The ratio of the intensity of the first peak with respect to the second, does not show any systematic variation with ρ (table 5.7). The inner peak seen in DDAB-PSS was not observed in any of the other DDAB-polyelectrolyte complexes studied, up to 8 nm which is the largest d-spacing that can be measured in our experimental set up. The d-spacings of the lamellar phase of all the DDAB- polyelectrolyte complexes are summarized in table 5.8.

5.6 Discussion

5.6.1 CTAB-SHN-polyelectrolyte complexes

All CTAB-polyelectrolyte complexes show a hexagonal phase. However the lattice parameters of the 2D hexagonal lattice vary, depending on the polyelectrolyte used. The diffraction pattern of CTAB-PVS and CTAB-PSS complexes indicate that though the lattice parameters remain almost the same for both the complexes, the electron density distribution is different.

Since PGA, PAA, PVS and PSS have very short persistence lengths (1-10 nm), the hexagonal phase of CTAB-SHN with the polyelectrolytes can be expected to consist of cylindrical micelles bridged by the polyelectrolyte chains (fig. 5.19). A similar structure has been proposed for the hexagonal phase of CTAB-PAA complexes earlier [11]. Since SHN is known to decrease the spontaneous curvature of cylindrical aggregates, the increase in the lattice

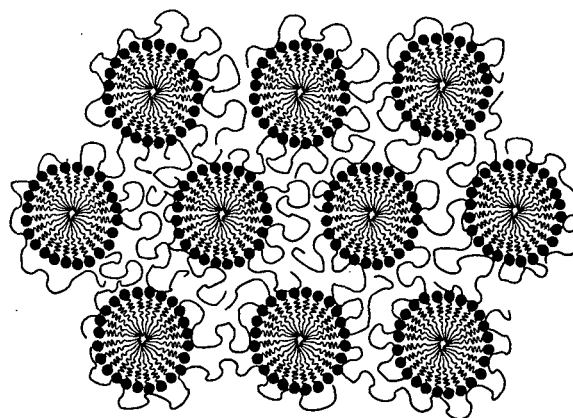


Figure 5.19: Schematic of the structure of the hexagonal phase of CTAB-polyelectrolyte complexes where the cylindrical micelles are bridged by the polymer chains.

parameters of hexagonal phase with SHN concentration can result from an increase in the size of the micellar cylinders. The lattice parameters of the hexagonal phase of the complex is similar to that observed in the hexagonal phase of CTAB-SHN with 50-60% water content (chapter 2, table 2.2).

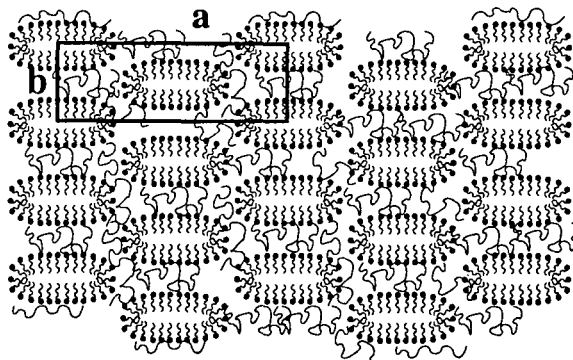


Figure 5.20: Schematic of the structure of the *cmm* phase of CTAB-SHN-PAA/PGA/PVS complexes where the ribbon-like surfactant aggregates are bridged by the polyelectrolyte chains.

The 2D centered rectangular lattice observed in CTAB-SHN-PGA complexes can arise if positional correlation develops between the PGA chains in the plane of the bilayers. However, as discussed in section 5.5.2, the neutron scattering experiments on DDAB-PGA complexes have shown that no positional correlations exist between the PGA strands in the plane of the bilayers [22]. The absence of such a correlation has been attributed to the low per-

sistence length of PGA. Hence positional correlation of the PGA strands can be ruled out in CTAB-SHN-PGA bilayers. Moreover, if such correlations exist, leading to the formation of a 2D lattice, the lattice parameters would depend on the PGA concentration. The lattice parameters in these complexes however remain independent of PGA concentration and are only weakly dependent on SHN concentration.

The structure of the centered rectangular phase observed at higher SHN concentrations in CTAB-SHN-PGA complexes is different from a similar phase observed in lipid-DNA complexes [25]. In cationic lipid-DNA complexes, a centered rectangular lattice arises from the transbilayer positional correlation of the DNA strands. Here, the lattice parameter corresponding to the separation between the DNA strands sandwiched between the bilayers, changes with the DNA concentration. Therefore, we propose a structure for the complexes of PGA with CTAB-SHN, consisting of ribbon-like aggregates arranged on a 2-D rectangular lattice (fig 5.20), corresponding to the plane group *cm*. Such a phase has been observed earlier in some surfactant systems in between the hexagonal and lamellar phases and also in the CTAB-SHN-water system as described in Chapter 2 [26]. However it has not been observed in any of the earlier studies on polyelectrolyte-surfactant systems.

The lattice parameters of CTAB-SHN-PAA complexes do not vary with PAA concentration, but depend weakly on SHN concentration. They are similar to those of CTAB-SHN-PGA complexes, indicating that PAA and PGA complexes form similar structures. Hence we propose that CTAB-SHN-PAA complexes also form a rectangular phase consisting of ribbon-like aggregates bridged by the polymer chains (fig 5.20). The lattice parameters of these complexes are comparable to those observed in the ribbon phases of CTAB-SHN-water system (Chapter 2).

The lattice parameters of CTAB-SHN-PVS complexes also do not vary with PVS concentration and depend weakly on SHN concentration. The lattice parameters are different

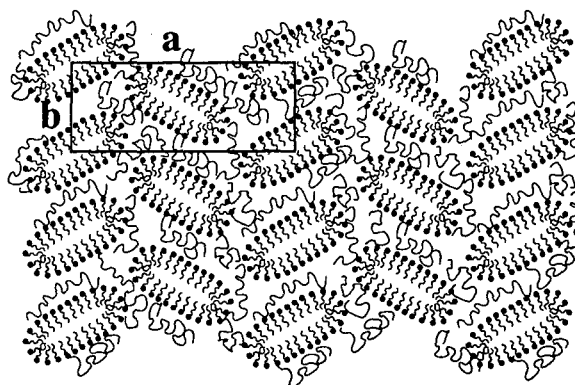


Figure 5.21: Schematic of the structure of the *pgg* phase of CTAB-SHN-PSS complexes where the ribbon-like surfactant aggregates are bridged by the polyelectrolyte chains.

from those observed in PAA and PGA complexes. The flexibility of PVS is however similar to that of PAA. Hence a PVS-PVS correlation cannot occur in the plane of the bilayers. Thus a ribbon phase similar to that seen in PAA and PGA complexes can be proposed for CTAB-SHN-PVS complexes characterized by a centred rectangular lattice.

The lattice parameters of CTAB-SHN-PSS complexes are weakly sensitive to SHN concentration and are independent of PSS concentration. This rules out a PSS-PSS correlation in the plane of CTAB-SHN bilayers. Hence the *pgg* structure of CTAB-SHN-PSS complexes at high SHN concentrations, most probably consists of ribbon-like aggregates bridged by polyelectrolyte chains (fig 5.21). Such structures have also been seen in some surfactant systems [27]. But we have not observed this in the CTAB-SHN-water system. Perhaps the complex is driven to form such structures because of their low water content. The phase observed in CTAB-SHN-PSS complexes at $\alpha = 0.7$, might also consist of ribbons arranged on an oblique lattice, a structure seen in sodium dodecylsulphate-water system [27].

The persistence length of a polyelectrolyte is very sensitive to counter-ion and salt concentrations [28]. Since most of the polyelectrolyte charges are neutralized in the complexes, the relevant quantity here is the intrinsic persistence length due to the stiffness of the polymer backbone. The persistence lengths of PGA, PAA, PSS and PVS are about 2, 1, 10 and 2 nm.

Table 5.9: Sequence of phase transitions in CTAB-SHN-Polyelectrolyte complexes on varying α .

polyelectrolyte	α	structure
PAA	0	2-D hexagonal
PAA	0.5	cmm
PAA	0.7	cmm
PGA	0	2-D hexagonal
PGA	0.5	cmm
PGA	0.7	cmm
PVS	0	2-D hexagonal
PVS	0.4	cmm
PVS	0.7	lamellar
PSS	0	2-D hexagonal
PSS	0.4	pgg
PSS	0.7	oblique?

They carry a bare charge of $1\bar{e}/0.154$ nm, $1\bar{e}/0.32$ nm, $1\bar{e}/0.25$ nm and $1\bar{e}/0.154$ nm respectively. In an earlier chapter of this thesis, we have seen that the complexes of CTAB-SHN with ds DNA and ss DNA, which have the same charge moiety but a persistence length that differ by almost to orders of magnitude, give similar structures at similar α . The complexes of CTAB-SHN with the polyelectrolytes, PAA and PVS which differ only by the chemical nature of the charge moiety exhibit a different sequence of transitions with α (table 5.9). However, PAA and PGA which have the same charge moiety but different bare charge densities and persistence lengths exhibit identical behaviour on varying α . Hence the structures seen in these complexes may not be primarily determined by the persistence length of the polyelectrolyte or its bare charge density. Similarly PSS and PVS exhibits different structures on varying α . Thus we find that the structures observed in these complexes are specific to each polyion. The theories of polyelectrolyte-surfactant complexation do not at present take into account the specificity of the polyion. Our results indicate that this needs to be incorporated to predict the variety of structures seen in these complexes.

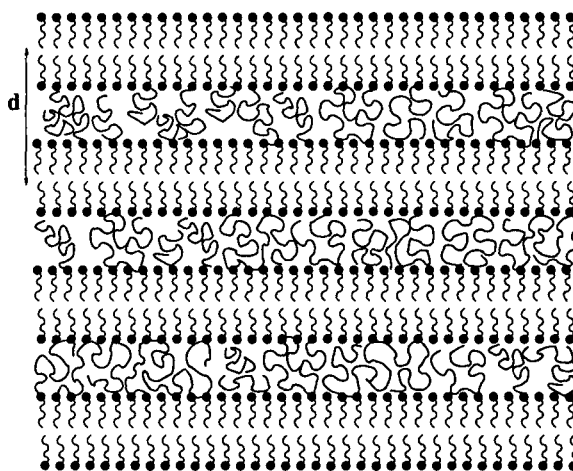


Figure 5.22: Lamellar phase of the complexes of flexible polyelectrolytes with DDAB. The bilayers are bridged by the flexible polymer chains

5.6.2 Structures in DDAB-polyelectrolyte complexes

Since DDAB always forms bilayers in aqueous solution [21], the lamellar phase of DDAB-DNA complexes is expected to consist of DNA sandwiched between bilayers; a structure similar to that seen in cationic lipid-DNA complexes (L_{α}^C). The lamellar periodicity of 4.51 nm for the DDAB-DNA complex is consistent with a DNA strand of diameter 2.5 nm, sandwiched between a bilayer of thickness 2 nm. The peak observed at 3.96 nm corresponds to the DNA-DNA peak (fig.5.15c). The hump at 2.51 nm appears due to scattering from the helical structure of the ds DNA strand (fig.5.15b).

The complexes of flexible polyelectrolytes with DDAB consists of bilayers bridged by the polyelectrolyte to form a lamellar structure (fig 5.22). The decrease in the lamellar periodicity when the polyelectrolyte concentration is below ρ_{iso} , could be the result of enhanced neutralization of the surfactant charges. The effective attraction between bilayers can also increase if more and more polyions bridge the bilayers when the polyelectrolyte concentration is increased. The bilayer periodicity of the various complexes (table 5.8) except for the single and double stranded DNA and PGA, is ~ 3.2 nm, the periodicity observed in the condensed lamellar phase (L_{α}') of the DDAB-water system. The absence of peaks corresponding to a correlation between the PAA, PGA or PVS strands is consistent with their persistence

length being ~ 1 nm; they remain disordered in the plane of the bilayers. Positional correlations between the polymer strands in the plane of the bilayers have been observed only for ds DNA strands whose persistence length is 50 nm [22].

The peak observed at 3.03 nm in DDAB-PSS complexes can arise due to scattering from the bilayers, if the complex forms a lamellar structure. This would lead us to surmise that the peak at smaller angles, corresponding to 6.03 ± 0.1 nm arises due to scattering from the PSS-PSS strands. We would then expect this peak position to shift with PSS concentration. However since the peak always appears at 6.03 nm, irrespective of the polyelectrolyte concentration, this possibility may be ruled out. In addition to this, we also find that when the sample is oriented, all the peaks appear along the q_z direction (fig 5.18). A PSS-PSS correlation peak, which arises from ordering in the plane of the bilayers would be oriented perpendicular to the lamellar peaks.

Due to the unique phase behaviour seen in DDAB-water system as discussed in section 5.5.1, it is possible that the complex forms two lamellar phases with distinct periodicities. But, to be consistent with the observations in the surfactant system, we would expect the peak position of the two coexisting lamellar phases in the complex, to shift with temperature (fig 5.11). However, the peak position is found to remain independent of temperature up to 73 °C, and then disappears. Moreover, if we assume that DDAB-PSS complex consists of two distinct lamellar phases, one would expect the scattering intensities corresponding to the two structures to vary with polyelectrolyte concentration. However the relative intensity of the inner peak with respect to the first order lamellar peak exhibits no particular dependence on ρ (table 5.7). The peak observed here at small angles has not been observed in any of the other polyelectrolyte complexes up to 8 nm.

The disappearance of the peak at high polyelectrolyte concentrations much below ρ_{iso} , is equally surprising. The dissolution of the complex at low salt concentrations (~ 50 mM

NaBr) indicates that the structure of the complex is highly sensitive to the presence of salt. Hence the structure of DDAB-PSS complex remains unexplained at present. More work is required to understand the structure exhibited by this complex.

5.6.3 Surfactant content of the various polyelectrolyte complexes

From the lattice parameters of the DDAB-polyelectrolyte complexes, we can estimate the surfactant content in the complexes. If δ_s is the bilayer thickness, d the lattice parameter, and if we assume that density of surfactant $\rho_s^{DDAB} \approx \rho_w$, the density of water, then the weight fraction of DDAB in the complex is $\phi_s^{DDAB} = \frac{\delta_s}{d}$. The bilayer thickness of DDAB in the complex, $\delta_s \sim 2$ nm. ϕ_s^{DDAB} calculated for the various complexes is given in table 5.10.

Similarly, we may also estimate the surfactant content of the hexagonal phase of CTAB-polyelectrolyte complexes. The radius of the CTAB cylinder, R_m is ~ 1.98 nm [11]. A unit cell of a hexagonal lattice consists of one cylindrical micelle of CTAB. The ratio of the area occupied by the cylinder to the area of a unit cell obtained from the lattice parameter of the hexagonal lattice, gives the surfactant weight fraction. We assume here that density of CTAB, $\rho_s^{CTAB} \approx \rho_w$ and that the radius of the micellar cylinders in the complex do not change with surfactant concentration. Hence the surfactant content of the CTAB-polyelectrolyte complexes are given by, $\phi_s^{CTAB} = (2 \pi R_m^2) / \sqrt{3}a^2$. These values are also given in table 5.10.

At similar SHN concentrations ($\alpha = 0.7$) the lattice parameters of CTAB-SHN-PAA/PGA complexes were nearly the same as the lattice parameters observed at $\phi_s = 0.6$ in the CTAB-SHN-water system. The lattice parameters of the centred rectangular phase at these SHN concentrations are $a = 13$ nm, $b = 5.4$ nm. Assuming that the size of the surfactant aggregates in the complex remain the same as those in the surfactant system at similar lattice parameters, we could estimate the surfactant content of CTAB-SHN-polyelectrolyte complex at $\alpha = 0.7$. Since PVS complexes form a lamellar phase at these SHN concentrations,

Table 5.10: Estimated surfactant content in complexes of polyelectrolytes with DDAB (ϕ_s^{DDAB}), CTAB (ϕ_s^{CTAB}) and CTAB-SHN (ϕ_s^{CS}). ϕ_s^{CS} corresponds to $\alpha = \sim 0.7$.

polyelectrolyte	ϕ_s^{DDAB}	ϕ_s^{CTAB}	ϕ_s^{CS}
ss DNA	0.48	0.48	0.58
PGA	0.52	0.5	0.6
PAA	0.58	0.53	0.61
PVS	0.63	0.66	0.69
PSS	0.66	0.66	

assuming a bilayer thickness of 3 nm for CTAB-SHN, we have estimated the surfactant content (see table 5.10).

Table 5.10 indicates that both CTAB and DDAB complexes exhibit similar behaviour. The surfactant content in the complex varies as ss DNA < PGA < PAA < PVS < PSS. Though the estimated surfactant content varies depending on the polyelectrolyte used, the structure remains the same for all the polyelectrolytes with the complex forming a hexagonal phase when the aggregates in the surfactant solution consists of cylinders (in the case of CTAB) and a lamellar phase when the surfactant solution consists of bilayers (in the case of DDAB). We need to note here that CTAB-water system consists of a hexagonal phase over a large range of surfactant concentration and DDAB forms only bilayers in aqueous solutions.

The behaviour observed above can be contrasted with the trends in CTAB-SHN-polyelectrolyte complexes. A variety of structures are observed in this system depending on the polyelectrolyte used. But if we estimate the water content in the CTAB-SHN-polyelectrolytes, for example at $\alpha (= [\text{SHN}]/[\text{CTAB}]) \sim 0.7$, they exhibit a trend (table 5.10) similar to the CTAB and DDAB complexes. The structures observed in the former vary depending on the polyelectrolytes used since the CTAB-SHN-water system at $\alpha \sim 0.7$, exhibits these structures at similar surfactant content (table 4, chapter 2). We have assumed here that for similar lattice parameters, the size of the surfactant aggregates remain the same in the complex as well as in the surfactant-water system.

Thus we find a correlation between the structure of the complex and the structure exhibited by the surfactant system at similar surfactant content. Such a correlation has not been suggested in any of the earlier studies; the use of a surfactant system with a very rich phase behaviour makes it possible in the present case.

5.7 Conclusions

We have studied in detail the influence of aggregate morphology on the structure of surfactant-polyelectrolyte complexes. This has been achieved by using SHN which tunes the spontaneous curvature of CTAB cylinders. For any given polyelectrolyte, the complex shows a variety of structures on varying α . We have obtained novel structures for the complexes, like *cm* and *pgg*, which have not been reported in earlier studies. These studies show that the chemical nature of the polyion plays an important role in determining the structure of the complexes, by determining the surfactant content of the complex. We also found that the structure exhibited by the complex is almost identical to that seen in the corresponding surfactant system at similar surfactant concentration.

Bibliography

- [1] E. D. Goddard and K. P. Ananthapadmanabhan (Editors), *Interactions of Surfactants with Polymers and Proteins* (CRC Press, Boca Raton) 1993.
- [2] R. Kuhn, Ber. Dtsch. Chem. Ges. **73**, 1080 (1940)
- [3] J. E. Scott, Chem. Ind. (London), 168 (1955).
- [4] T. C. Laurent, and J. E. Scott, Nature **202**, 661 (1964)
- [5] T. Gilanyi, and G. Wolfram, Colloids Surf. **3**, 181 (1981)
- [6] B. Cabane, J. Phys. Chem. **81**, 1639 (1977)
- [7] J. N. Turro, B. H. Barretz, and P. L. Kuo, Macromolecules **17**, 1321 (1984).
- [8] K. Thalberg, B. Lindman, and K. Bergfeldt, Langmuir **7**, 2893 (1991).
- [9] R. Nagarajan, Colloids Surf. **13**, 1 (1985).
- [10] F. M. Witte and B. F. Engberts, Colloids Surf **36**, 417 (1989).
- [11] P. Ilekli, T. Martin, B. Cabane, and L. Piculell, J. Phys. Chem. B **103**, 9831 (1999).
- [12] P. Ilekli, L. Piculell, F. Tournilhac, and B. Cabane, J. Phys. Chem. B **102**, 344 (1998).
- [13] M. Clerc, J. Phys. II (France) **6**, 961 (1996).
- [14] M. Antonietti, J. Conrad, and A. Thunemann, Macromolecules **27**, 6007 (1994).
- [15] E. A. Ponomarenko, A. J. Waddon, K. N. Bakeev, D. A. Tirrell, and W. J. MacKnight, Macromolecules **29**, 4340 (1996).

- [16] P. Hansson, *Langmuir* **14**, 4059 (1998).
- [17] S. Zhou, F. Yeh, C. Burger, and B. Chu, *J. Phys. Chem. B* **103**, 2107 (1999)
- [18] D. Ruppelt, J. Kotz, W. Jaeger, S. E. Friberg, R. A. Mackay, *Langmuir* **13**, 3316 (1997).
- [19] J. Merta, M. Torkkeli, T. Ikonen, R. Serimeaa, and P. Stenius, *Macromolecules* **34**, 2937 (2001).
- [20] J. Merta, V. M. Garamus, A. I. Kuklin, R. Willumeit, and P. Stenius, *Langmuir* **16**, 10061 (2000).
- [21] M. Dubois and Th. Zemb, *J. Chem. Phys.* **108**, 7855 (1998).
- [22] G. Subramanian, R. P. Hjelm, T. J. Deming, G. S. Smith, Y. Li, and C. R. Safinya, *J. Am. Chem. Soc.* **122**, 26 (2000).
- [23] E. A. Ponomarenko, A. J. Waddon, K. N. Bakeev, D. A. Tirrell, and W. J. Macknight, *Macromolecules* **29**, 4340 (1996).
- [24] T. Salditt, I. Koltover, J. O. Raedler, and C. R. Safinya, *Phys. Rev. E* **58**, 889 (1998).
- [25] F. Artzner, R. Zantl, G. Rapp, and J. O. Raedler, *Phys. Rev. Lett.* **81**, 5015 (1998).
- [26] Y. Hendriks and J. Charvolin, *J. Physique* **42**, 1427 (1981).
- [27] P. Kekicheff and B. Cabane, *J. Physique* **42**, 1427 (1981).
- [28] K. Ghosh, G. A. Carri, M. Muthukumar, *J. Chem. Phys.* **115**, 4367 (2001).

